Search for Standard Model Higgs Bosons Decaying to W-Boson Pairs in $p\bar{p}$ Collisions at $\sqrt{s} = 1.96$ TeV

by

Dean Andrew Hidas

Department of Physics
Duke University

Date:_____
Approved:

_____
Dr. Mark C. Kruse, Supervisor

_____
Dr. Steffen A. Bass

_____
Dr. Richard G. Palmer

_____
Dr. Christopher W. Walter

_____
Dr. Ying K. Wu

Dissertation submitted in partial fulfillment of the
requirements for the degree of Doctor of Philosophy
in the Department of Physics
in the Graduate School of
Duke University

2008

ABSTRACT

(Physics)

Search for Standard Model Higgs Bosons Decaying to W-Boson Pairs in $p\bar{p}$ Collisions at $\sqrt{s} = 1.96$ TeV

by

Dean Andrew Hidas

Department of Physics
Duke University

Date:_____
Approved:

_____
Dr. Mark C. Kruse, Supervisor

_____
Dr. Steffen A. Bass

_____
Dr. Richard G. Palmer

_____
Dr. Christopher W. Walter

_____
Dr. Ying K. Wu

An abstract of a dissertation submitted in partial fulfillment of
the requirements for the degree of Doctor of Philosophy
in the Department of Physics
in the Graduate School of
Duke University

2008

Abstract

This thesis describes a search for standard model Higgs bosons decaying to W boson pairs in proton-anti-proton collisions at a center of mass energy of 1.96 TeV using the CDF II detector. The decay to W bosons is dominant for Higgs masses greater than about 135 GeV. The final state examined consists of two leptons and missing transverse energy from the leptonic decay of one or more W bosons. The signal production mechanisms included are gluon fusion, associated production with a W or Z boson, and vector boson fusion. Matrix element calculations and artificial neural networks are used to discriminate signal from background for Higgs masses in the range $110 \leq M_H \leq 200$ GeV. No significant excess of events is observed at any of the Higgs masses investigated. Upper limits on the standard model Higgs cross section are set at 95% confidence for each Higgs mass investigated, the most stringent limit being 1.63 times the predicted standard model cross section for a Higgs mass of 160 GeV.

Contents

List of Tables

List of Figures

List of Abbreviations

BR Branching ratio.

CDF Refers to the Collaboration named Collider Detector at Fermilab.

CDF II Refers to the physical detector used in this analysis.

CES The shower-maximum detector located in the EM calorimeter in the central calorimeter wedges.

CKM Cabibbo-Kobayashi-Maskawa usually in reference to the CKM matrix.

CLC Cherenkov luminosity counter which is used to measure the luminosity.

CMP Muon detector in the central region ($|\eta_{det}| < 0.6$) which sits beyond the calorimeters and additional 60 cm of steel shielding. This detector is used to confirm muon hits in the CMU detector.

CMU Muon detector embedded in the outer region of the central calorimeters covering a pseudo-rapidity range of $|\eta_{det}| < 0.6$

CMUP This is a muon category referring to muons which have a stub in both the CMU and CMP detectors

CMX This refers to both a muon detector and a muon category. This muon category requires a stub in the CMX detector.

COT The central outer tracker which is a wire drift chamber used for charged particle tracking.

CrkTrk A high P_T track which points to a crack in the calorimeter and is of unknown type. These objects are assumed to be electron or muons in this analysis.

DY Drell-Yan production.

EM Generally refers to "electromagnetic" and often to the electromagnetic calorimeter.

HAD The hadronic calorimeter.

ISL The intermediate silicon layers which are radially between the SVX and the COT.

LR Likelihood ratio of matrix element based probabilities.

L00 The innermost silicon tracking layer which is attached to the beampipe itself.

MC Monte Carlo.

PES The shower-maximum detector located in the EM calorimeter in the forward calorimeters.

PHX A forward electron category which relies on silicon tracking.

QCD Quantum chromodynamics.

SL Sulerlayers of the central outer tracker (COT).

SM The standard model of particle physics

SVXII The 5-layer silicon tracking detector which lies just outside of the L00.

TCE Tight central electron.

VBF Vector boson fusion. This is in reference to the Higgs production mechanism.

VH Higgs boson produced in association with a W or Z boson.

XFT The eXtremely Fast Tracker uses COT information to reconstruct tracks for level 1 trigger decisions.

α_s The strong coupling constant.

$\not\!\!E_T$ The fully corrected missing transverse energy.

$\not{E}_T^{spec}$	"Met special" is the quantity used to select signal region events. This is defined in section 5.5.1.
$\not{E}_T^{sig}$	"Met significance" is defined in equation 5.5.
η	The pseudo-rapidity.
η_{det}	The pseudo-rapidity as defined from $z = 0$.

Acknowledgments

First I would like to thank my advisor Mark Kruse for his guidance and support throughout my graduate years. Thank you for sticking with me, sticking up for me, for the many opportunities you gave me, and for the knowledge and time you have shared.

I owe many thanks to the members of our analysis group, Susan Burke, Sergo Jindariani, Jennifer Pursley, and Simone Pagan Griso without whose efforts this analysis would have not been possible. I thank you for all of your hard work, support, and especially for you kindness and willingness to help throughout. It was really a pleasure to get to work with such a fantastic group of people, who couldn't have come into my life at a better time. I owe special thanks to Eric James who brought us all together and gave us momentum.

jenraaf (PhD!!), whose name I am no longer allowed to capitalize, the only other person who truly understands The Roma D's, thank you. A slice **is** more than just nice. It is, in fact, *delicious*. Thanks to Kirby and Copic for dragging me out when "my advisor would want me to go". I still think you should have 6th gear checked. It makes an awful grinding noise, even worse then the sound of me dying trying to keep up on one of Kirby's "easy recovery rides", I swear. Dr. G for many of the best dinners out west which kept me laughing. It was always a pleasure. Many thanks to Toby Davies, with whom I shared many many commiserating Monday

lunches with. My office mate of 5 years and good friend Jianrong Deng with whom I shard the majority of my waking hours, thank you for putting up with my mess for so long, and more so your friendship and all of the wonderful times together. Bodhitha Jayatilaka, for our hourly espresso breaks. And on that note, thanks to Doug Benjamin for keeping me supplied. I would also like to thank, in general, coffee for getting me through, even if you are addictive.

To my classmates from the beginning, many thanks. Bason Clancy, remember, I was grad school WM 1! To Carolyn Berger, for being a friend from the beginning even while far apart and to Andy and Leslie for the first couple of years and always giving me a place to crash. To M. Stephen M. Smith for getting me out of the office.

To my "aunt" Joan and "uncle" John Ward who are nothing short of family to me, I thank you for your never-ending generosity and for always giving me a warm place when I was so far from home.

Last, and most of all, I would like to thank my parents, Bonny and Peter Hidas, and my sister Laura Hidas for their support, patience, and understanding over the years. While so far away you were always close, encouraging, and forgiving. Thank you for all that you have given me.

Chapter 1

Introduction

The standard model of particle physics is a description of the fundamental particles, quarks and leptons, and the forces between them, mediated by the vector gauge bosons g, $W^{\pm}$, Z, and γ. To date, it has been enormously successful in describing these particles and the interactions between them. Despite its many successes, direct experimental verification of one of its most striking properties is still lacking.

In 1964 Peter Higgs proposed a mechanism by which the fundamental particles acquire mass in a theory that was until then, a theory of massless particles. This simple addition explains the masses of the $W^{\pm}$ and Z gauge bosons and is extended to explain the masses of the quarks and leptons. A consequence of this addition is the unavoidable prediction of a new particle, called the Higgs boson. The Higgs boson is the only fundamental particle in the standard model of particle physics which has yet to be experimentally verified and it is this striking and unobserved feature which is the topic of this thesis. It has been the topic of theses past and will certainly be the topic of many theses to come. Perhaps one of them will contain the word "Discovery" in the title, or, perhaps not. Either of these conclusions will be interesting in its own right. Either there is some truth in the Higgs, or the truth is still out there.

The Higgs boson can be produced in many ways and can decay to many different particles. How a Higgs is produced and decays is well known and depends on its mass. However, the mass of the Higgs is itself an unknown. Although the mass of the Higgs is not predicted by the standard model, previous experimental results (discussed in chapter 2) indicate that its mass is most likely in the range $114 \leq M_H \leq 154$ GeV with a theoretical upper limit of about 1 TeV.

This thesis presents a search for a high mass (generally this refers to $M_H > 135$ GeV) Higgs in the range of $110 \leq M_H \leq 200$ GeV where its decay to W boson pairs is the decay of interest. Specifically, this thesis describes a search for Higgs bosons in a final state consisting of two leptons, which may be any combination of electrons and muons, and a net energy imbalance in the detector arising from neutrinos which escape undetected.

The experiment is carried out at Fermi National Accelerator Laboratory (Fermilab) where protons and anti-protons are made to collide at a center of mass energy of 1.96 TeV. The products of these collisions are investigated using the CDF II detector. This is the topic of chapter 3.

This analysis begins with the careful definition of lepton (electron and muon) identification and the kinematic selection of events as discussed in chapters 4 and 5 respectively. Several event selection criteria different from the signal selection criterion are investigated to ensure that the data is being properly modeled by simulation and that different backgrounds are correctly estimated. These "control regions" are discussed in section 5.6. Two other important measurements that are made to verify the analysis as a whole are the measurement of the top quark pair production cross section and the WW production cross section. These cross section measurements

are discussed in section 5.6.5 and chapter 7 respectively.

This analysis uses 3 fb^{-1} of data from which 918 events are selected in the signal region. Matrix element probability calculations (chapter 6) and artificial neural networks (chapter 8) are used to discriminate signal from background in a total of 5 channels. When no appreciable excess of events is observed, these channels are combined in a Bayesian calculation of an upper limit (described in chapter 11) on standard model Higgs production. The results of these calculations are given in section 11.4

Unit Convention

In this thesis the convention $\hbar = c = 1$ is used so that mass, energy, and momentum will all be expressed in units of GeV.

Chapter 2

The Standard Model and the Higgs Mechanism

The standard model (SM) of particles physics is a gauge field theory which incorporates both quantum mechanics and Einstein's theory of special relativity in an attempt to describe the fundamental particles and their interactions. The standard model describes three of the four known fundamental forces of nature: strong interactions, electromagnetic interactions, and weak interactions. The fourth known force, being gravity, is far weaker (roughly 40 orders of magnitude smaller than the strong nuclear force) and is not expected to contribute significantly to the physical processes which are of current interest in high energy particle physics.

The standard model is described by the gauge group

$$SU(3)_C \times SU(2)_L \times U(1)_Y \tag{2.1}$$

which is invariant under local gauge transformations. The C is a reminder that $SU(3)$ represents the symmetry group of the *colored* strong interactions of quantum chromodynamics (QCD). The L indicates that the $SU(2)$ group contains left-handed weak isospin doublets and the Y is a reminder that the $U(1)$ group contains the

right-handed weak hypercharge singlets. Together, the $SU(2)_L \times U(1)_Y$ groups govern the now unified electroweak force.

There are two main classifications of particles which the SM describes. These are the spin-$\frac{1}{2}$ *fermions* that are the constituents of normal matter and the integer spin *bosons* which are the mediators of the strong and electroweak forces. Particles in the SM acquire mass via interactions with a so-called Higgs field which is a result of a spontaneously broken symmetry arising in the $SU(2)_L \times U(1)_Y$ electroweak sector. The predicted Higgs boson resulting from this broken symmetry is the only particle in the SM which has yet to be experimentally verified and is the topic of this thesis. The remainder of this chapter describes the fundamental particles and their interactions, the Higgs mechanism, and the phenomenology related to the experimental aspects of this thesis.

2.1 Fundamental Particles

2.1.1 Fermions

Fermions are spin-$\frac{1}{2}$ fundamental particles that appear as two different types: quarks and leptons. Quarks are the constituents of familiar composite particles such as the proton and neutron, but can combine to form other hadrons which are a bound state of 2 or 3 quarks called mesons and baryons respectively. Quarks interact via both the strong and electroweak forces. Leptons, such as the electron, on the other hand only interact via the electroweak force.

	Flavor	Charge (Q)	Quantum Numbers	Mass (GeV)
1st Generation	u	$+2/3$	$U = +1$	$(1.5 - 3.3) \times 10^{-3}$
	d	$-1/3$	$D = -1$	$(3.5 - 6.0) \times 10^{-3}$
2nd Generation	c	$+2/3$	$C = +1$	$1.27^{+0.07}_{-0.11}$
	s	$-1/3$	$S = -1$	$104^{+26}_{-34} \times 10^{-3}$
3rd Generation	t	$+2/3$	$T = +1$	171.2 ± 2.1
	b	$-1/3$	$B = -1$	$4.2^{+0.17}_{-0.07}$

Table 2.1: Charge, *quark*-ness, and mass [27] for the quarks.

Quarks

There are six types of quarks (plus their anti-quarks and color partners): up, down, charm, strange, top, and bottom. Quarks have non-integer electric charge (Q) and a quantum property called *color charge* similar to the electric charge of electromagnetism, however it comes in three flavors being r, g, and b. There is also a quantum number associated with each quark *charmness* (C), *strangeness* (S), and so on. The charges (Q) and masses of the different quarks are listed in table 2.1 along with their *quark*-ness quantum number.

The up and down quarks are the constituents of everyday matter such as protons and neutrons and together with the electron and electron neutrino constitute the "first generation" of fundamental fermions. The heavier and more exotic quarks are typically only created in high energy collisions and are constituents of the second and third generations. Quarks are subject to both strong interactions as well as electroweak interactions which are discussed in sections 2.2 and 2.3 respectively.

Flavor	Charge (Q)	Lepton Numbers	Mass (GeV)
e	-1	$L_e = 1$	0.511×10^{-3}
ν_e	0	$L_e = 1$	$< 225 \times 10^{-9}$
μ	-1	$L_\mu = 1$	105.7×10^{-3}
ν_μ	0	$L_\mu = 1$	$< 0.19 \times 10^{-3}$
τ	-1	$L_\tau = 1$	1.777
ν_τ	0	$L_\tau = 1$	$< 18.2 \times 10^{-3}$

Table 2.2: Charge, lepton number, and mass [27] for the quarks.

Leptons

There are six types leptons (plus their anti-particles) in the SM. These are the electron, muon, tau (e, μ, τ), and their respective neutrinos (ν_e, ν_μ, ν_τ). They are classified by their charge and lepton quantum numbers (L_e, L_μ, and L_τ) as given in table 2.2. Leptons are subject to the electroweak force. They are colorless and thus do not participate in strong interactions.

Although the neutrino masses are listed as having an upper limit as indicated in table 2.2, there is now strong evidence from measurements of neutrino mixing that they are in fact nonzero [36]. Also, it is worth noting that the τ lepton is the only lepton with enough mass to decay hadronically, and it will do so with a branching fraction of 65% [27].

2.1.2 Bosons - Force Mediators

All interactions in the SM are mediated by spin-1 bosons. The gluon (g) is the mass-less bi-colored mediator of the strong force. The photon (γ), $W^\pm$, and Z are the force carriers of the electroweak interactions. The photon is mass-less while the $W^\pm$ and Z are massive particles. In the SM the $W^\pm$ and Z acquire mass as a

	Interactions	Charge	Mass (GeV)
g	strong	0	0
γ	electromagnetic	0	0
Z	weak	0	91.1876 ± 0.0021
$W^{\pm}$	weak	± 1	80.398 ± 0.025

Table 2.3: A summary of the force carriers of the standard model and their masses [27].

consequence of electroweak symmetry breaking through the Higgs mechanism which is discussed in section 2.4. The gauge bosons and their properties are summarized in table 2.3. The role of these force carriers in particle interactions is described in sections 2.2 and 2.3.

2.2 Quantum Chromodynamics

Quantum chromodynamics (QCD) is the study of the strong force between quarks and gluons. Quarks carry a single color charge while a gluon is bicolored and is the mediator of color flow. In $SU(3)$ the three colors give nine total color states for the gluon: a color octet and a color singlet. However, the singlet is colorless and so in nature there are only 8 possible colored gluons.

Quarks only exist in colorless bound states with integer charge. For instance the proton is the combination of three quarks uud perhaps having the colors rgb (among other possibilities) respectively, which sum to give a colorless bound state with a net charge of +1. Quark-anti-quark combinations are also possible, for example, the pion π^+ which is a $u\bar{d}$ bound state whose quarks have the color combination possibilities $r\bar{r}$ or $b\bar{b}$.

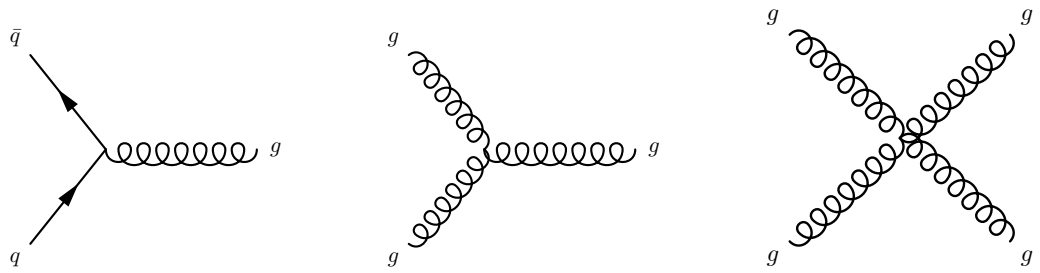

Figure 2.1: The primary vertices of QCD.

A striking feature of the strong force is that the coupling becomes increasingly large with separation distance. This indicates that colored partons will be confined in objects which are as a whole color neutral. The coupling constant of QCD (α_s) is a running constant which is given by

$$\alpha_s(q^2) = \frac{12\pi}{(33 - 2n_f)\log(q^2/\Lambda^2)} \tag{2.2}$$

where Λ is of the order 0.1 GeV and n_f is the number of quark flavors whose mass is greater than the q^2 of interest [7]. At very large q^2 or very short distances α_s becomes increasingly small. This phenomena is known as asymptotic freedom. Also, this property allows for high-q^2 perturbative expansion of QCD processes which remain finite.

Gluons couple only to quarks and other gluons via the qqg, ggg, and $gggg$ vertices shown in figure 2.1. Color, charge, and quark-ness are always conserved in strong interactions.

The QCD Lagrangian is given by

$$\mathcal{L}_{QCD} = -\frac{1}{4}F_a^{\mu\nu}F_{a\mu\nu} + \bar{\psi}_j(i\gamma_\mu D^\mu_{jk} - M_j\delta_{jk})\psi_k \tag{2.3}$$

where D^{μ}_{jk} is the covariant derivative

$$D^{\mu}_{jk} = \delta_{jk}\partial^{\mu} + ig(T_a)_{jk}G^{\mu}_{a} \tag{2.4}$$

and M the quark mass matrices discussed further in section 2.4. g is the strong coupling constant and G^{μ}_{a} the gluon fields. $F^{\mu\nu}_{a}$ is the gluon field tensor and ψ_k the quark fields. Quark-gluon interactions can be seen in the covariant derivative acting on the quark fields in equation 2.3. T are the $SU(3)$ generators and have the commutation relation

$$[T_i, T_j] = if_{ijk}T_k \tag{2.5}$$

which defines the structure constants f of QCD. γ are the "gamma matrices" which in the Dirac representation are give by

$$\gamma^0 = \begin{pmatrix} I & 0 \\ 0 & -I \end{pmatrix},\ \gamma^i = \begin{pmatrix} 0 & \sigma_i \\ -\sigma_i & 0 \end{pmatrix},\ \gamma^i = \begin{pmatrix} 0 & I \\ I & 0 \end{pmatrix} \tag{2.6}$$

where σ_i are the pauli matrices given by

$$\sigma^x = \begin{pmatrix} 0 & 1 \\ 1 & 0 \end{pmatrix},\ \sigma^y = \begin{pmatrix} 0 & -i \\ i & 0 \end{pmatrix},\ \sigma^z = \begin{pmatrix} 1 & 0 \\ 0 & -1 \end{pmatrix} \tag{2.7}$$

and I is the 2×2 identity matrix.

2.3 Electroweak Interactions

The electroweak interaction of quarks and leptons is described by the $SU(2)_L \times U(1)_Y$ gauge group. Weak isospin (T_L) and hpercharge (Y) are the respective generators of symmetry transformations. They satisfy the equation

$$Q = T_3 + \frac{1}{2}Y \tag{2.8}$$

where T_3 is the projection of the third component of the weak isospin vector.

The electroweak Lagrangian is given by

$$\mathcal{L} = -\frac{1}{4}W^{\mu\nu}W_{\mu\nu} - B^{\mu\nu}B_{\mu\nu} + \bar{\psi}i\gamma^{\mu}D_{\mu}\psi \tag{2.9}$$

where the covariant derivative is

$$D_{\mu} = \partial_{\mu} + igW_{\mu}T + \frac{1}{2}ig'B_{\mu}Y. \tag{2.10}$$

T is the weak isospin operator and $B_{\mu\nu}$, similar to the electromagnetic field tensor, is given by

$$B_{\mu\nu} = \partial_{\mu}B_{\nu} - \partial_{\nu}B_{\mu} \tag{2.11}$$

where B_{ν} is the massless gauge field representing the singlet of $U(1)_Y$. W_{μ} are the gauge fields of $SU(2)$ and $W_{\mu\nu}$ the field tensor which is defined as

$$W_{\mu\nu} = \partial_{\mu}W_{\nu} - \partial_{\nu}W_{\mu} - gW_{\mu} \times W_{\nu}. \tag{2.12}$$

By requiring the electromagnetic and weak forces to be unified and to describe the bosons observed experimentally it is required that there be two neutral and two charged bosons. Thus the electromagnetic field A and neutral current Z must be some linear combination of the unified electroweak fields. This can be written in terms of the electroweak mixing angle θ_w as

$$\begin{pmatrix} Z \\ A \end{pmatrix} = \begin{pmatrix} \cos\theta_w & -\sin\theta_w \\ \sin\theta_w & \cos\theta_w \end{pmatrix} \begin{pmatrix} W^3 \\ B \end{pmatrix} \tag{2.13}$$

from which can be shown that the parameters g and g' have the relation $g' = g\tan\theta_w$ and are also related to the charge of the electron e by the relation $e = g\sin\theta_w$. The remaining two components of W_μ are then related to the observables W^+ and W^-. The real fields are then given by

$$\begin{aligned} W_\mu^\pm &= \frac{1}{\sqrt{2}}(W_\mu^1 \mp iW_\mu^2) \\ Z_\mu &= \frac{-g'B_\mu + gW_\mu^3}{\sqrt{g^2+g'^2}} \\ A_\mu &= \frac{gB_\mu + g'W_\mu^3}{\sqrt{g^2+g'^2}}. \end{aligned}$$

The term in the electroweak Lagrangian given in equation 2.9 responsible for the interaction of quarks and leptons with the gauge bosons is $\bar{\psi}i\gamma^\mu D_\mu\psi$ which can be rewritten in a form which allows easier identification of the specific gauge boson interactions as

$$eJ_{EM}^\mu A_\mu + \frac{g}{\sqrt{2}}(J_L^{+\mu}W_\mu^+ + J_L^{-\mu}W_\mu^-) + \frac{gg'}{e}J_Z^\mu Z_\mu \tag{2.14}$$

where

$$\begin{aligned} J_L^{\pm\mu} &= \sqrt{2}\bar{\psi}\gamma^\mu T_L^\pm \psi \\ J_Z^\mu &= \bar{\psi}\gamma^\mu (T_{3L} - \sin^2\theta_w Q)\psi \\ J_{EM}^\mu &= \bar{\psi}\gamma^\mu Q\psi \end{aligned}$$

which are the charged and neutral current interaction terms describing the interaction of the gauge bosons with the fermion ψ fields.

Singlet states ψ_R do not survive operations by T and T_{3L}. Since neutrinos do not carry charge it can be seen that there are no right-handed neutrino states ν_R. The relevant quantum numbers for the allowed fermion states are shown in table 2.4.

In electroweak interactions the leptons numbers L_e, L_μ, and L_τ are always conserved. Electroweak interactions among the leptons only occur within a single family and there is no inter-generational mixing. This is not the case for quarks in charged current interactions. Apparently the quark mass eigenstates are not exactly the same as the electroweak eigenstates. The quark eigenstates of electroweak charged current interactions are given by

$$\begin{pmatrix} u \\ d' \end{pmatrix}, \quad \begin{pmatrix} c \\ s' \end{pmatrix}, \quad \begin{pmatrix} t \\ b' \end{pmatrix}$$

where the mixing is described by the Cabibbo-Kobayashi-Maskawa (CKM) matrix

$$\begin{pmatrix} d' \\ s' \\ b' \end{pmatrix} = \begin{pmatrix} V_{ud} & V_{us} & V_{ub} \\ V_{cd} & V_{cs} & V_{cb} \\ V_{td} & V_{ts} & V_{tb} \end{pmatrix} \begin{pmatrix} d \\ s \\ b \end{pmatrix}. \tag{2.15}$$

Although there are 9 elements in the CKM matrix, there are only 4 free parameters which can be expressed as 3 angles and one CP (charge-parity) violating phase, for instance the Kobayashi-Maskawa form

$$V = \begin{pmatrix} c_1 & -s_1c_3 & -s_1s_3 \\ s_1c_2 & c_1c_2c_3 - s_2s_3e^{i\delta} & c_1c_2s_3 + s_2c_3e^{i\delta} \\ s_1s_2 & c_1s_2c_3 + c_2s_3e^{i\delta} & c_1s_2s_3 - c_2c_3e^{i\delta} \end{pmatrix} \tag{2.16}$$

where s and c refer to sin and cos and their subscript the angle θ_i. δ is then the CP violating phase. Thus there are four parameters which are θ_1, θ_2, θ_3, and δ. CP violation, though very small, is now well established with CPT (charge, parity, and time operations) believed to be the preserved underlying symmetry.

This unified theory of the electromagnetic and weak interactions describes physical reality rather well at high energies where Q^2 is much greater than the mass of the partons involved. However, it has one major shortcoming in that it describes only mass-less particles. The Higgs mechanism, described in section 2.4, is the mechanism by which particles in the SM acquire mass.

Family			T	T_3	Y	Q
$\begin{pmatrix} \nu_e \\ e \end{pmatrix}_L$	$\begin{pmatrix} \nu_\mu \\ \mu \end{pmatrix}_L$	$\begin{pmatrix} \nu_\tau \\ \tau \end{pmatrix}_L$	$1/2$ $1/2$	$+1/2$ $-1/2$	-1 -1	0 -1
e_R	μ_R	τ_R	0	0	-2	-1
$\begin{pmatrix} u \\ d \end{pmatrix}_L$	$\begin{pmatrix} c \\ s \end{pmatrix}_L$	$\begin{pmatrix} t \\ b \end{pmatrix}_L$	$1/2$ $1/2$	$+1/2$ $-1/2$	$+1/3$ $+1/3$	$+2/3$ $-1/3$
u_R	c_R	t_R	0	0	$+4/3$	$+2/3$
d_R	s_R	b_R	0	0	$-2/3$	$-1/3$

Table 2.4: Weak isospin, hypercharge, and electric charge for the quarks and leptons.

2.4 Electroweak Symmetry Breaking and the Higgs Mechanism

In 1964 Peter W. Higgs published a very short paper on "Broken Symmetries and the Masses of Gauge Bosons" [47] in which he describes a mechanism by which gauge bosons can acquire mass. The Higgs mechanism has since been fully incorporated into the standard model and is responsible for the gauge boson and fermion masses. This mechanism not only gives rise to particle masses, but also predicts a new spin-0 scalar, now called the Higgs boson. It is through interactions with this Higgs field that particles acquire mass.

In order to give the gauge bosons mass, a scalar field Φ and potential term $V(\Phi) = \mu^2|\Phi|^2 + \lambda|\Phi|^4$ is introduced to the electroweak Lagrangian given in equation 2.9 as

$$\mathcal{L}_\Phi = |D_\mu \Phi|^2 - \mu^2|\Phi|^2 - \lambda|\Phi|^4.$$

If μ^2 is positive then the potential $V(\Phi)$ is symmetric about its minimum which

is 0. However, in the case where $\mu^2 < 0$ the potential has a minimum at

$$|\Phi| = \sqrt{\frac{-\mu^2}{2\lambda}}$$

as can be seen in figure 2.2. The ground state is said to have spontaneously picked a direction, which has given rise to a non-zero vacuum expectation value and a broken symmetry. The complex doublet Φ can be written in terms of the vacuum expectation value and two real fields with zero vacuum expectation value ξ and H as

$$\Phi(x) = \exp\left(\frac{i\xi(x)\cdot\tau}{2v}\right)\begin{pmatrix} 0 \\ (v+H(x))/\sqrt{2} \end{pmatrix} \tag{2.17}$$

where $v = \sqrt{-\mu^2/\lambda}$. Here, H will be the Higgs field and $\xi(x)$ are non-physical fields known as Goldstone bosons. With an appropriate gauge transformation the ξ fields will vanish. The gauge of choice is called the unitary gauge where

$$\Phi(x) = \frac{1}{\sqrt{2}}\begin{pmatrix} 0 \\ v+H(x) \end{pmatrix}$$

and the Lagrangian $\mathcal{L}_\Phi$ becomes

$$\mathcal{L}_\Phi = \frac{1}{2}(\partial H)^2 + \frac{1}{4}g^2W^+W^-(v+H)^2 + \frac{1}{8}\left(\frac{gg'}{e}\right)^2 ZZ(v+H)^2 - V\left(\frac{1}{2}(v+H)^2\right).$$

What has happened here is that the goldstone bosons ξ have vanished and as a result, the gauge bosons have acquired terms which can be identified as mass terms. For the W and Z bosons they can essentially be read off the equation above and

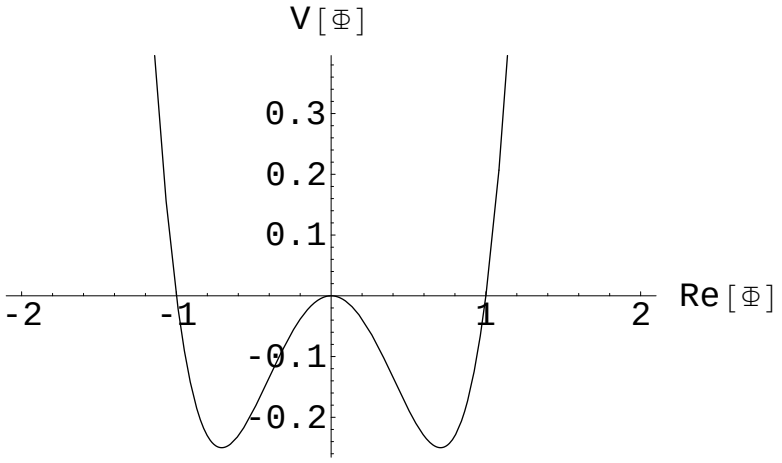

Figure 2.2: Higgs potential $V(\Phi)$ for $\mu < 0$.

are given by

$$M_W = \frac{1}{2}gv, \qquad M_Z = \frac{1}{2}\frac{gg'}{e}v.$$

The Higgs itself has an associated mass term coming from the potential term V

$$M_H = \sqrt{-2\mu^2}.$$

Recall that g and g' are related by the electroweak mixing angle θ_w. It follows that M_W and M_Z are related by

$$M_W = M_Z \cos\theta_w.$$

Experimentally one can measure both M_W and M_Z and given the relationship between g and g' show that $v = 246$ GeV [58]. Then the only undetermined parameter is μ which implies that the mass of the Higgs is undetermined, however there are

some theoretical limitations on the values that it can take on which is discussed further in section 2.7.

Electroweak symmetry breaking and the Higgs mechanism have thus far provided a mechanism for gauge boson masses. It is still lacking a mechanism by which quarks and leptons acquire mass. Fermion masses are generated in the Higgs mechanism by what is called the Yukawa coupling. The Yukawa interaction term in the Lagrangian for a lepton is given by

$$\mathcal{L}_\ell = -G_l \left[\overline{\ell_R}(\Phi^\dagger \ell_L) + (\overline{\ell_L}\Phi)\ell_R\right]$$

for the singlet ℓ_R and doublet ℓ_L where G_ℓ is a coupling constant. In the unitary gauge this becomes

$$\mathcal{L}_\ell = -\frac{1}{\sqrt{2}} G_\ell v \bar{\ell}\ell - \frac{1}{\sqrt{2}} G_\ell H \bar{\ell}\ell \tag{2.18}$$

from which the lepton mass can be read off as

$$M_\ell = \frac{1}{\sqrt{2}} G_\ell v.$$

The direct coupling of the leptons to the Higgs is evident in the $H\bar{\ell}\ell$ term in equation 2.18. Note that although the Higgs mass is not known, its couplings to all particles are well defined and depend on the particle masses.

Similarly for the quarks, a Yukawa coupling can be added of the form

$$\mathcal{L}_q = -\sum_{i=1}^{3}\sum_{j=1}^{3}\left[\tilde{G}_{ij}\overline{u_{iR}}(\tilde{\Phi}^\dagger D_{jL}) + G_{ij}\overline{d_{iR}}(\Phi^\dagger D_{jL})\right] + \text{h.c.}$$

where u_i and d_i refer to the up and down-*type* quarks. Here G is related to the quark mass matrices by

$$M^u_{ij} = \frac{v}{2}\tilde{G}_{ij}, \qquad M^d_{ij} = \frac{v}{2}G_{ij}$$

The quark, lepton, and gauge boson masses are both well motivated and experimentally well measured. The focus of this thesis is standard model Higgs production and decay, specifically the WWH coupling. These topics are discussed in the following section. Although this thesis presents a search for standard model Higgs it should be noted that other theories exist which attempt to explain spontaneous symmetry breaking and particle mass. Some of these ideas are briefly mentioned in section 2.8 but are not otherwise considered in the analysis presented here.

2.5 Standard Model Higgs Phenomenology

2.5.1 Higgs Production

Four Higgs production mechanisms are investigated in this analysis. The cross sections for these processes at the Tevatron are shown as a function of the Higgs mass in figure 2.3. The largest contribution to the total cross section is from the gluon fusion channel ($gg \rightarrow H$) where two gluons interact via a quark loop (dominated by the top quark in this case because of its large mass) to produce a single Higgs as shown in figure 2.4 along with the Feynman diagrams of the other three production processes. This production channel is particularly useful for high mass (> 135 GeV) Higgs searches where the WW^* decay products can have a fairly

clean signature (when both Ws decay leptonically) but is essentially inaccessible at lower mass where the dominant $b\bar{b}$ decay of the Higgs is overwhelmed by huge QCD backgrounds.

This gluon fusion process is known at next-to-next-to-leading order (NNLO) in QCD in the limit of large top mass [45]. Contributions from multiple soft-gluon emission have also been included at next-to-next-to-leading logarithmic level ($\sigma^{NNLL}_{gg\to H}$) [15]. Independent two-loop electroweak corrections (δ_{EW}) [5] are applied on top of the best available calculations in QCD which gives the best estimates of the cross section ($\sigma^{NNLL}_{gg\to H} \times \delta_{EW}$) which are listed in table 2.7. The electroweak corrections δ_{EW} range from $+8\%$ to -2% [4]. The uncertainty on this cross section is estimated to be about 8% [15] by varying the factorization and renormalization scales (μ_F and μ_R) about M_H.

It is interesting to note that the higher-order corrections to the cross section in the case of $gg \to H$ are indeed quite large. The "K" factor for the ratio of $NNLL\times\ \delta_{EW}$ to the LO $gg \to H$ cross section is shown in table 2.5. The LO cross sections were obtained using the HNNLO program [38] which includes calculations at LO, NLO, and NNLO.

There are three other production mechanisms considered in this analysis each of which is roughly an order of magnitude smaller than the gluon fusion process, but contribute significantly to the analysis. A Higgs can be produced in association with a W or Z boson (often denoted as VH) as well as resulting from initial state quarks which radiate vector bosons that then combine to produce a Higgs (called vector boson fusion, or VBF) as shown in figure 2.4. The latter has a unique signature in that there are two quarks in the final state which tend to have a small transverse

M_H (GeV)	$\sigma^{LO}_{gg\to H}$ (fb)	$\sigma^{NNLL}_{gg\to H} \times \delta_{EW}$ (fb)	$K^{LO\to NNLL\times\delta_{EW}}$
110	458	1132	2.5
120	359	1058	2.9
130	284	848	3.0
140	227	687	3.0
145	209	622	3.0
150	184	563	3.1
155	162	511	3.2
160	143	461	3.2
165	123	410	3.3
170	114	368	3.2
175	107	334	3.1
180	97	303	3.1
190	81	248	3.1
200	68	207	3.0

Table 2.5: Cross sections for various Higgs masses calculated at LO compared to the best available ($NNLL \times \delta_{EW}$) and the "K" factor associated with them ($K^{LO\to NNLL\times\delta_{EW}}$).

momentum component and are very boosted in the direction of the initially colliding quarks, meaning that they tend to be very "forward", or have large rapidity.

Associated production of a Higgs (VH) is known at NNLO in QCD and higher order electroweak corrections are calculated at NLO [12, 17]. Vector boson fusion is known at NLO in QCD. The cross sections σ_{WH}, σ_{ZH}, and σ_{VBF} are shown for various Higgs masses in table 2.7. The theoretical uncertainty associated with these values for σ_{WH}, σ_{ZH}, and σ_{VBF} are estimated to be 5% [17], 5% [12], and 10% [9], respectively.

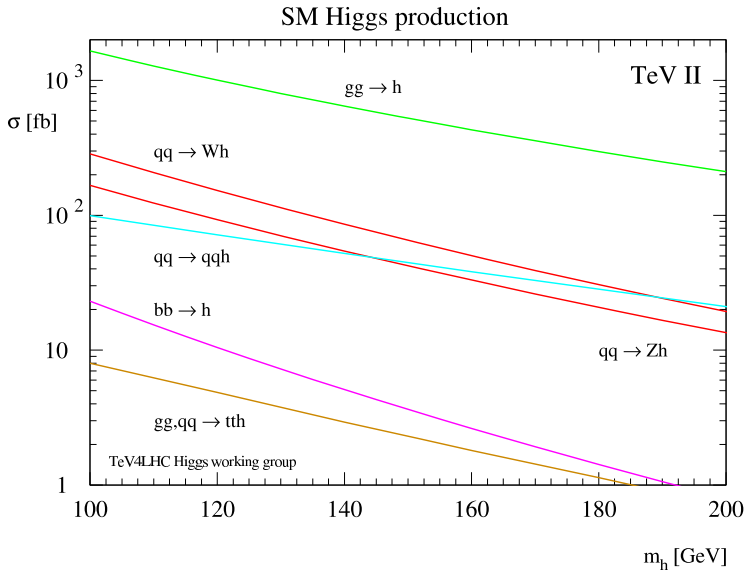

Figure 2.3: Higgs production cross sections for the various production mechanisms in $p\bar{p}$ collisions at $\sqrt{s} = 1.96$ TeV as a function of the Higgs mass [1].

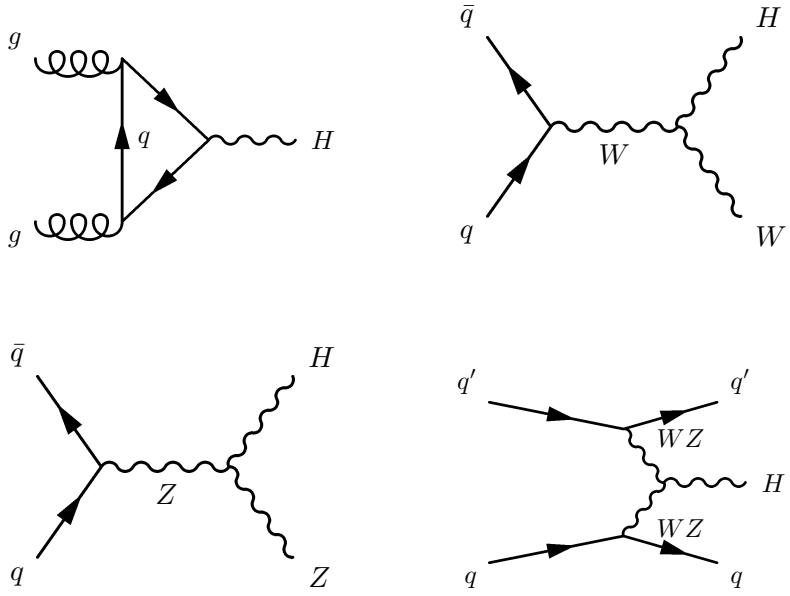

Figure 2.4: Leading order Feynman diagrams for the four main Higgs production mechanisms in $p\bar{p}$ collisions at $\sqrt{s} = 1.96$ TeV.

2.5.2 Higgs Decay

Once produced, a Higgs boson can decay in many ways. The probabilities for the different possible decay channels, or relative widths $\Gamma_i/\Gamma_{\text{Total}}$, are a strong function of the Higgs mass. The branching fraction (or branching ratio, BR) for various decay modes can be seen in figure 2.5. The two largest decay channels in the mass range which experiments at the Tevatron are currently probing are $H \to b\bar{b}$ which is the dominant mode for $M_H < 135$ GeV and $H \to WW^*$ for $M_H > 135$ GeV. The branching fraction to W boson pairs peaks around 160 GeV where the Higgs can decay to two on-shell Ws. Currently CDF exploits these two main channels as well as the $H \to \tau\bar{\tau}$ channel in combination with the production mechanisms discussed in section 2.5.1. The low mass (< 135 GeV) searches must rely on the associated production modes (VH) with subsequent leptonic decay of the vector boson, in order to have any reasonable sensitivity, otherwise the $H \to b\bar{b}$ signal is completely overwhelmed by QCD production of jets. This analysis focuses exclusively on the $H \to WW^*$ decay in the dilepton channel which will be the topic of the remainder of this thesis. W^* indicates that one of the W bosons must be off-shell if $M_H < 2M_W$.

There are several ways in which a Higgs can be produced and decay into a dilepton final state. The simplest way is to produce a single Higgs via gluon fusion giving

$$gg \to H \to WW^* \to \ell\nu\bar{\ell}\bar{\nu} \tag{2.19}$$

where one can identify the two leptons and significant missing transverse energy ($\not\!\!E_T$) from the neutrinos. Recall that this production mechanism has the largest cross section, but can only be used for the high mass searches. One interesting

property to note about this decay arises from the spin correlations among the decay products of the Higgs in the dilepton final state. The Higgs is a spin-0 scalar particle which in this case decays into two spin-1 vector particles whose spins must then be anti-aligned in the Higgs rest frame. The couplings of the leptons to Ws allows for only left-handed neutrinos and right-handed anti-neutrinos. As a result of these couplings one can deduce that the neutrinos (ν) are preferentially emitted in the same direction as is the case with the other leptons (e, μ, or τ) and hence the separation angle of the charged leptons will tend to be small.

In the case of associated production there are a number of ways in which one can end up with a similar final state. For WH there will essentially be 3 Ws which can give, among others

$$WH \rightarrow WWW \rightarrow \begin{cases} \ell\nu\ell\nu qq \\ \ell\nu\ell\nu\ell\nu \end{cases} . \tag{2.20}$$

Here note that in practice one might get a dilepton signature from a truly trilepton event where one lepton may not be reconstructed in the detector.

The case is similar for ZH which can give

$$ZH \rightarrow ZWW \rightarrow \begin{cases} \nu\nu\ell\nu\ell\nu \\ qq\ell\nu\ell\nu \\ \ell\ell\ell\nu qq \end{cases} . \tag{2.21}$$

These signatures are not the only decay modes, but are the most likely candidate modes to contribute a significant signal acceptance in real experiments as they have

M_H (GeV)	$gg \to H$	WH	ZH	VBF	Total
110	3996	623	371	252	5242
120	3173	459	278	215	4124
130	2543	342	212	183	3280
140	2062	258	163	156	2639
145	1865	225	143	144	2377
150	1690	196	126	134	2146
155	1534	172	112	124	1941
160	1382	153	99	115	1749
165	1229	132	88	106	1556
170	1103	117	78	99	1397
175	1001	103	70	92	1265
180	909	92	62	85	1149
190	743	73	50	73	939
200	622	58	41	63	783

Table 2.6: Number of Higgs bosons produced in 3 fb^{-1} for each process and Higgs mass considered.

≥ 2 leptons and real missing energy from the neutrinos in the final state.

Vector boson fusion is somewhat more straightforward since in requiring the decay $H \to WW$ there is really only one final state involving dileptons given by

$$qq \to qqH \to qqWW \to qq\ell\nu\ell\nu. \tag{2.22}$$

In particular VBF has the distinctive signature of the two outgoing quarks having very large rapidity as mentioned in section 2.5.1. The number of Higgs bosons produced in 3 fb^{-1} for each process considered are given in table 2.6 for the different masses investigated in this analysis.

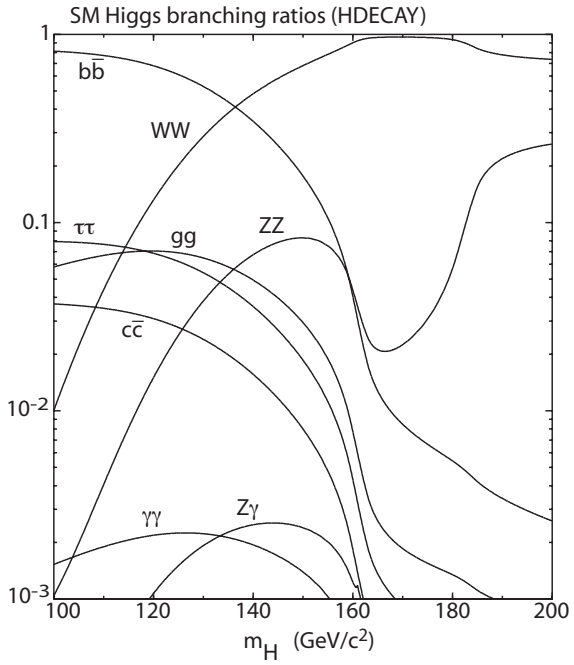

Figure 2.5: Higgs branching ratios as a function of the Higgs mass from HDECAY [25].

M_H (GeV)	$\sigma^{NNLL}_{gg\to H} \times \delta_{EW}$	σ_{WH}	σ_{ZH}	σ_{VBF}	$\mathrm{Br}_{\mathrm{H}\to\mathrm{WW}}$
110	1.2808 × 1.0400	0.2075	0.1236	0.0841	0.0441
120	1.0062 × 1.0510	0.1529	0.0927	0.0717	0.1320
130	0.8013 × 1.0580	0.1141	0.0705	0.0611	0.2869
140	0.6455 × 1.0650	0.0860	0.0542	0.0521	0.4833
145	0.5818 × 1.0685	0.0749	0.0477	0.0481	0.5731
150	0.5251 × 1.0730	0.0654	0.0421	0.0445	0.6817
155	0.4750 × 1.0765	0.0572	0.0373	0.0412	0.8007
160	0.4310 × 1.0690	0.0510	0.0331	0.0382	0.9011
165	0.3920 × 1.0450	0.0441	0.0294	0.0354	0.9566
170	0.3566 × 1.0310	0.0389	0.0261	0.0329	0.9653
175	0.3254 × 1.0250	0.0344	0.0233	0.0305	0.9505
180	0.2972 × 1.0200	0.0306	0.0208	0.0283	0.9345
190	0.2493 × 0.9940	0.0243	0.0166	0.0244	0.7761
200	0.2105 × 0.9850	0.0193	0.0135	0.0210	0.7347

Table 2.7: Higgs production cross sections for various production mechanisms in $p\bar{p}$ collisions at $\sqrt{s} = 1.96$ TeV and branching ratios to W boson pairs for the Higgs masses specifically used in this analysis. Cross sections (σ) are all given in pb. δ_{EW} refers to the additional 2-loop electroweak corrections.

2.6 Standard Model Backgrounds

There are several SM processes which can result in a final state with 2 leptons. By far the largest of these processes is Drell-Yan ($q\bar{q} \rightarrow Z/\gamma^* \rightarrow \ell^+\ell^-$). However, the most difficult background experimentally is WW production, which can look very similar to the $H \rightarrow WW$ signature. The major SM backgrounds are briefly described below.

2.6.1 Drell-Yan : Z/γ^*

Of the SM backgrounds which have 2 leptons in the final state, the Drell-Yan process is by far the largest. The cross section for $p\bar{p} \rightarrow Z/\gamma^*$ production is 355×1.4 for $M_{\ell\ell} > 20$ GeV. The leading order Feynman diagram is shown in figure 2.6. In this process a quark and an anti-quark annihilate to produce Z/γ^* which can decay into a lepton pair. The Z contribution is strongly peaked at around 90 GeV while the γ^* contribution dominates the lower mass region. This process does not contain any neutrinos in the final state and thus does not have any inherent, or *real* missing energy since there are no neutrinos in the final state. The shear number of dilepton events produced along with imperfect energy resolution in a detector means that it is likely that a large number of events will pass a selection criterion designed to select Higgs events (discussed in section 5.5).

2.6.2 WW Production

While not the largest cross section among the backgrounds, the WW signal is the most *Higgs-like* and hence requires a good deal of attention. The s and t channel

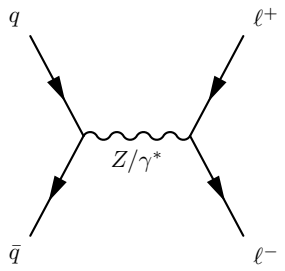

Figure 2.6: Leading order Feynman diagram for Drell-Yan production and decay to leptons.

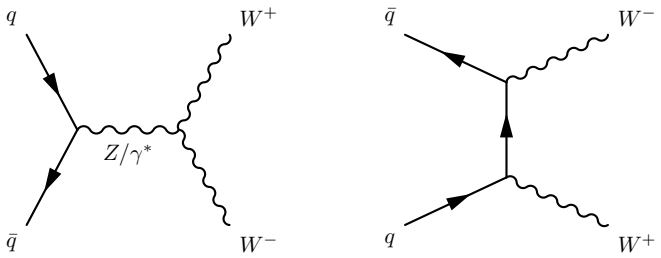

Figure 2.7: Tree level diagrams for WW production in the s-channel (*left*) and t-channel (*right*).

diagrams are shown in figure 2.7. The total cross section calculated at NLO is 12.4 ± 0.8 pb [13]. A W boson will decay to a lepton and a neutrino ($e\nu$, $\mu\nu$, or $\tau\nu$) one third of the time and hence WW will yield a dilepton one ninth of the time. Considering only electrons or muons in the final state this drops to 4.9%, but if one considers the leptonic decay of the tau this number increases to 5.8% (before considering any E_T or P_T requirements). The WW decay will have two high energy leptons and significant missing energy from neutrinos in the final state considered here.

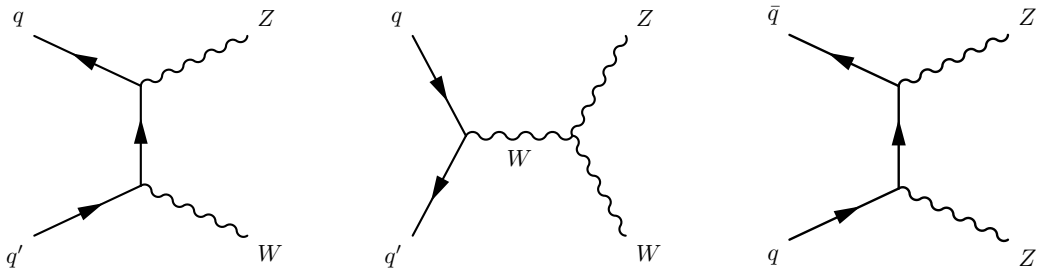

Figure 2.8: Tree level diagrams for WZ t-channel (*left*), s-channel (*middle*), and ZZ (*right*) production.

2.6.3 Other Dibosons : WZ and ZZ

The WZ and ZZ cross sections are relatively small at the Tevatron. These cross sections are predicted at NLO to be 3.7 ± 0.3 pb and 1.4 ± 0.1 pb [13] respectively. The ZZ cross section in particular was only recently measured at CDF and D0 with good statistical significance (4.4σ [32] and 5.7σ [29] respectively). Tree level diagrams for WZ and ZZ production are shown in figure 2.8.

There are several ways in which WZ might end up in a dilepton sample. The Z must decay leptonically and the W can decay to two quarks ($WZ \to qq'\ell^+\ell^-$) or a lepton-neutrino pair ($WZ \to \ell\nu\ell^+\ell^-$). Also, it should be noted that the leptons ℓ can be tau leptons which decay hadronically with a branching fraction of 65% [27]. In the former case one lepton must be missed and in the latter there is no neutrino present as a source for missing energy. Nevertheless, this process will show up in both forms in real data. Contributions to a dilepton sample from ZZ will mainly come from the case where one Z decays to a lepton pair and the other decays into neutrinos ($ZZ \to \ell^+\ell^-\nu\bar{\nu}$) or jets ($ZZ \to \ell^+\ell^- jj$). A much smaller contribution will come from the leptonic decay of both Z bosons with two leptons missed.

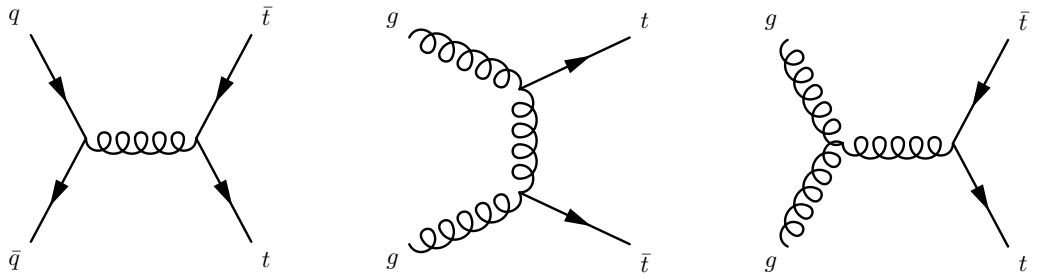

Figure 2.9: Leading order diagrams for top pair production at the Tevatron.

2.6.4 Top Pair Production : $t\bar{t}$

Top pair production can result from quark-antiquark annihilation or through gluon-gluon fusion. Leading order diagrams for top pair production are shown in figure 2.9. At the Tevatron the dominant production process is expected to be quark-antiquark annihilation. For a top mass of 175 GeV the Standard Model cross section at $\sqrt{s} = 1.96$ TeV is calculated to be $6.7^{+0.7}_{-0.9}$ pb and in the interval $170 < m_t < 190$ GeV this number varies by about 0.2 pb [30].

Due to the large CKM mixing parameter $V_{tb} = 0.999133^{+0.000044}_{-0.000043}$ [27], the top quark will decay to Wb essentially all of the time. Top decay followed by a leptonic decay of the W is shown in figure 2.10. Both Ws can decay leptonically and do so with a total branching fraction of 5.8% including the branching fractions of τ leptons to electrons and muons. There is significant missing energy in these events arising from the leptonic decay of the Ws, and also jets from the b-quarks in the final state.

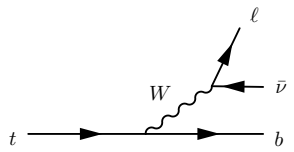

Figure 2.10: Feynman diagram for top decaying to Wb where the W decays leptonically.

2.6.5 Sources of Fake Backgrounds : $W\gamma$ and W+Jets

There are two sources of background which do not inherently contain two leptons in the final state, but which will appear in the dilepton sample as a result of misclassification of either the photon (γ) or a jet (originating from a quark or gluon). The two contributions to this are $W\gamma$ and W+jets production. These *fake* backgrounds are discussed further in section 4.4.

2.7 Current Constraints on the Standard Model Higgs

Previous experiments at LEP provided direct search constraints on standard model Higgs production. In combination, ALEPH, DELPHI, L3, and OPAL set a lower limit on the mass of this Higgs of 114.4 GeV at 95% confidence [18]. Other precision measurements of electroweak parameters of the standard model give an indication of the preferred Higgs mass and provide an upper limit on the Higgs mass based on a fit of these parameters at different Higgs masses. Figure 2.12 shows the $\Delta\chi^2$ of a fit to these parameters as a function of the Higgs mass where $\Delta\chi^2 = \chi^2 - \chi^2_{min}$. This provides an indirect implication of the mass of the Higgs which appears in

loop corrections to these measurements as shown in figure 2.11. The minimum $\Delta\chi^2$ indicates that the fit prefers a lower mass Higgs at 84 GeV and gives an upper limit of 154 GeV at 95% confidence. This limit increases to 187 GeV if you include the direct search limit from LEP in the fit. It should be noted that while this is an indication of the preferred Higgs mass it is by no means proof that the Higgs must lie in this range or must exist at all. While the $\Delta\chi^2$ has its minimum at 84 GeV the χ^2_{min} itself is between 1.4 and 1.6 depending on the parameters being fit [19].

Two parameters in this fit which both have a significant impact on the fit itself and are of primary interest at the Tevatron are the mass of the W boson and of the top quark, along with their uncertainties. The mass of the W boson, top quark, and Higgs boson are all intimately tied together as shown in the loop corrections of figure 2.11. Figure 2.13 shows the current knowledge of these two masses along with potential Higgs masses. Here the 68% (1σ) confidence interval overlaps slightly with the tail end of the LEP direct exclusion.

From the partial wave analysis of WW scattering amplitudes one can derive an upper limit on the Higgs mass of approximately 1 TeV [56] given by

$$M_H < \left(\frac{8\sqrt{2}\pi}{3G_F}\right)^{\frac{1}{2}} \approx 1 \text{ TeV}. \tag{2.23}$$

Contributions to the WW scattering amplitude from diagrams involving a Higgs are crucial in canceling terms with otherwise violent high energy behavior. This upper limit demands partial wave unitarity and if this limit is violated it implies that the perturbative methods used to construct the limit itself are not necessarily valid. It may also indicate that the weak interactions become much stronger at high

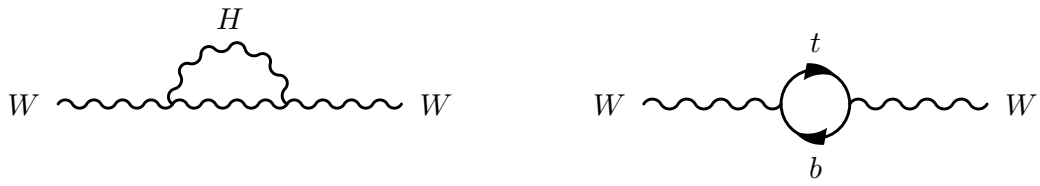

Figure 2.11: Loop corrections to the W boson mass involving a fermion loop (*left*) and the Higgs boson (*right*).

enough energies such that perturbation theory will not suffice.

2.8 Higgs Beyond the Standard Model

Although the standard model Higgs is the topic of this thesis, it should be noted that this is not the only theory which attempts to explain electroweak symmetry breaking and particle masses. Several other theories exist such as supersymmetry (SUSY), a minimal supersymmetric standard model (MSSM), technicolor, and fourth-generation models to name a few.

SUSY in particular interrelates fermions and bosons, giving each a super-partner. As a result of the supersymmetry this model predicts two bosonic Higgs doublets and their spin-$\frac{1}{2}$ sHiggs super-partners. SUSY also predicts not only a neutral Higgs, but charged Higgs' as well.

MSSM also predicts two Higgs doublets. In this minimal SUSY model some couplings to *down* type fermions can be greatly enhanced such that a Higgs-like object might couple to b quarks and τ leptons much more strongly.

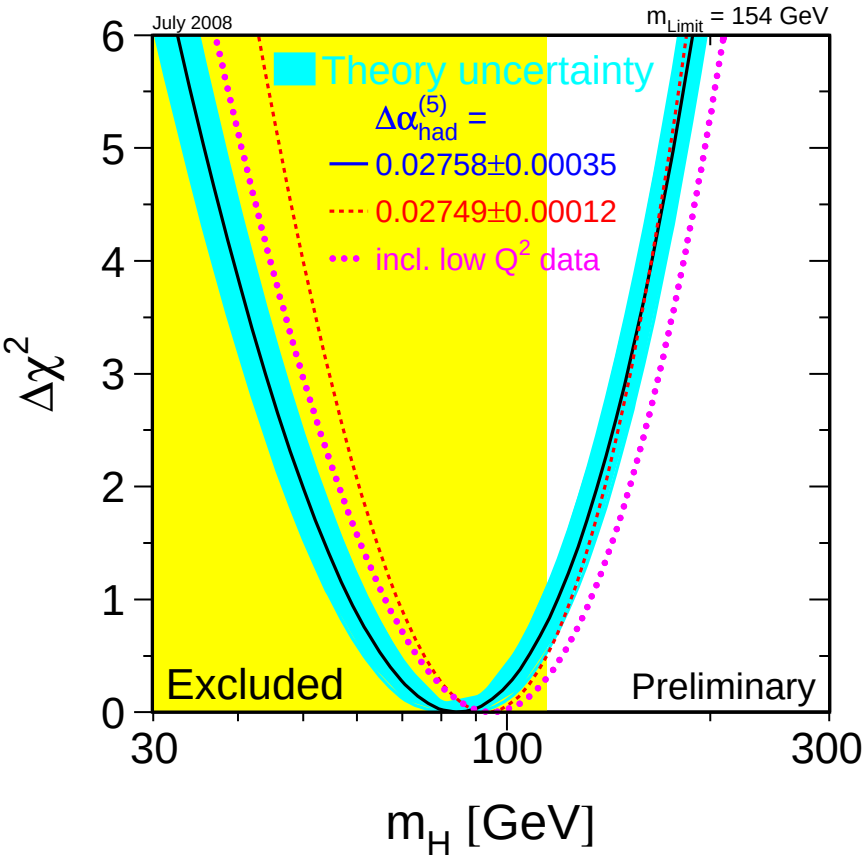

Figure 2.12: $\Delta\chi^2$ as a function of the Higgs mass using precision electroweak data from LEP, SLD, CDF, and D0 as of July 2008 [39]. The yellow shaded region indicates the direct search exclusion from LEP.

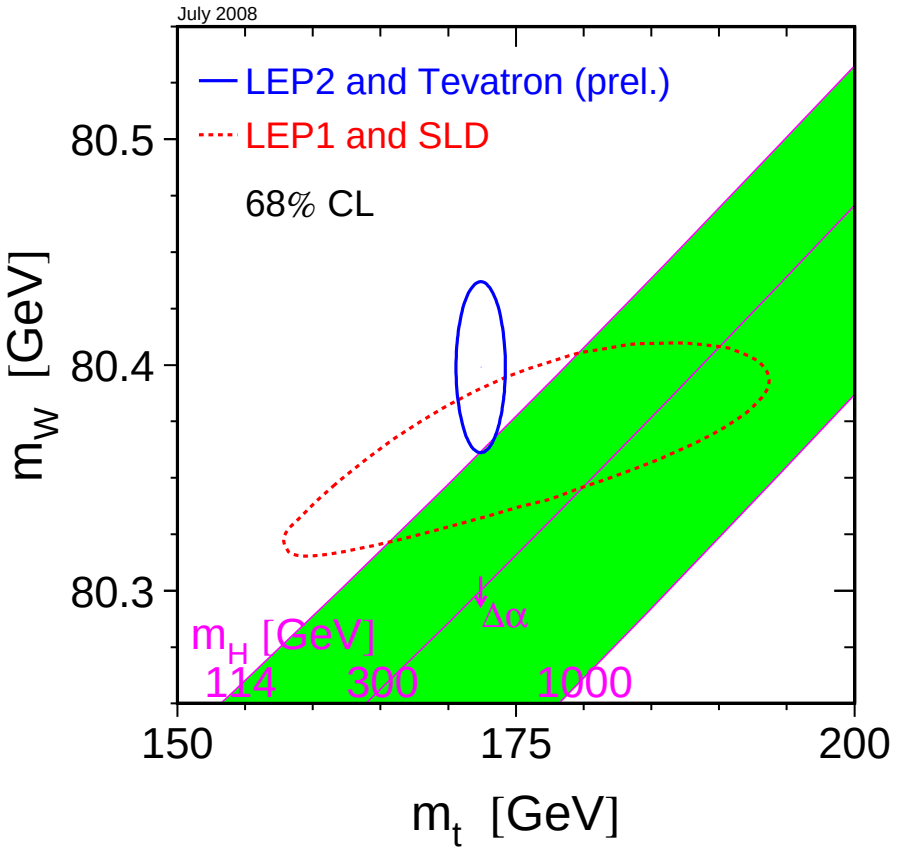

Figure 2.13: M_W vs. M_t 68% confidence intervals from several experiments as of July 2008 showing the compatibility with different potential Higgs masses [39].

Chapter 3

The Tevatron and CDF II Detector

In this analysis high energy collisions between protons and anti-protons are investigated. Through a series of accelerators, protons and anti-protons are accelerated to a final colliding center of mass energy of 1.96 TeV in the Tevatron. The CDF II detector is situated at a collision point on the Tevatron ring and is used to investigate the products of these collisions. The Fermilab accelerator chain and CDF II detector are described in this chapter.

3.1 The Tevatron and Accelerator Complex

Fermilab's Tevatron is currently the world's highest energy operational hadron collider. There are 8 accelerators total which in the end provide proton-anti-proton ($p\bar{p}$) collisions at $\sqrt{s} = 1.96$ TeV. A diagram of the chain of accelerators is shown in figure 3.1. The different accelerators are discussed in the following sub-sections.

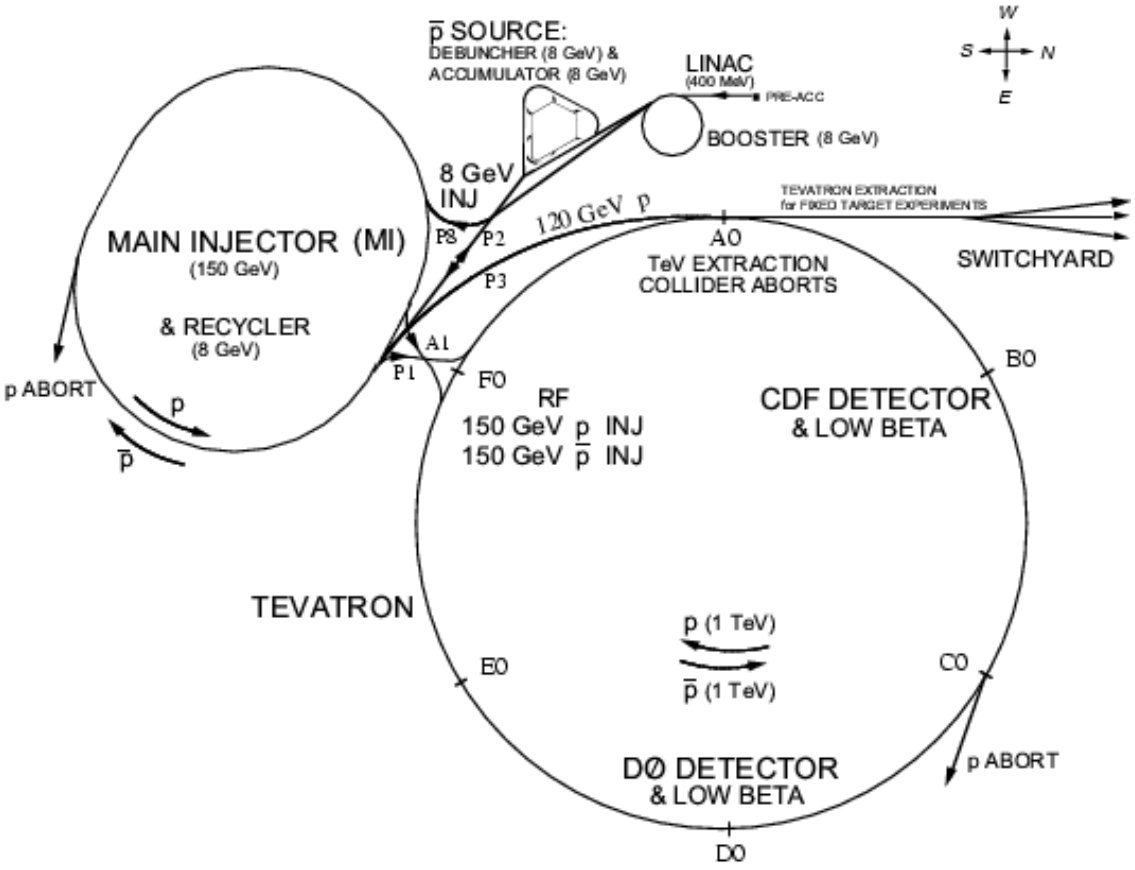

Figure 3.1: The Fermilab accelerator complex.

3.1.1 Cockcroft-Walton

The starting point in the accelerator chain begins with the Cockcroft-Walton, which is a Van de Graff accelerator that provides a continuous beam of H^- ions at 750 keV. The H^- ions begin as hydrogen gas. The hydrogen gas is placed in an electric field which strips the hydrogen atoms of an electron to become H^+. These protons (H^+) are then attracted to a cesium anode where they attach and acquire two electrons to become H^- which is then repelled by the anode. These H^- ions are then accelerated by the Cockcroft-Walton to 750 keV.

3.1.2 Linac

The linear accelerator accepts H^- ions from the Cockcroft-Walton at 750 keV. These ions are accelerated by electric fields between successive drift tubes of increasing length. This field is varied at high frequency (RF) such that when exiting a drift tube some of these negative ions will see an electric field pointing in the opposite direction of their velocity in each gap region, which increases their energy. The ions which arrive out of phase with the RF system will be decelerated, and not make it through the entire linac. The result of this is a beam consisting of bunched H^- ions in the linac. These bunches are accelerated to an energy of 400 MeV by the linac. At the end of this 130 m accelerator the H^- ions pass through a thin carbon foil where the electrons are stripped away from H^- leaving H^+ (protons).

3.1.3 Booster

The booster is the first of several synchrotrons in the accelerator chain which accelerates 400 MeV bunches of protons from the linac to an energy of 8 GeV. This is done in 16,000 revolutions where each revolution is about 475m. This is on average in increase of 475 keV per revolution.

3.1.4 Main Injector

The main injector accepts protons from the booster or anti-protons from the accumulator or recycler (see section 3.1.5) at 8 GeV. This synchrotron accelerates protons and anti-protons (not simultaneously) from 8 GeV to either 120 GeV for production of anti-protons or to 150 GeV for injection into the Tevatron.

3.1.5 Anti-Protons

Accumulating a sufficient amount of anti-protons for collisions in the Tevatron is a difficult task. Protons at 120 GeV from the main injector are sent into a nickel target which creates many different particles and only a few anti-protons. Roughly, for every million protons that are sent to the nickel target about 20 anti-protons will be produced with an energy that will be accepted by the accumulator. The particles that are created from the protons interacting with the target are focused using a lithium lens and then the anti-protons are separated using a magnetic field. The rate at which anti-protons are accumulated is on the order of tens of mA per hour. For perspective, at a rate of 20 mA/h for six years (which is roughly the data-set this thesis investigates) continuously, this would amount to a grand total

of 20 picograms of anti-protons.

Debuncher, Accumulator, and Recycler

After the anti-protons are created and filtered out they enter the debuncher in bunches which tend to have a large energy spread. The debuncher stochastically cools this beam translating the large energy spread into a large time spread such that the anti-protons have a more uniform energy distribution. Roughly every 1.2 seconds these anti-protons are sent from the debuncher to the accumulator. The accumulator is an 8 GeV storage ring that is used to collect successive injections of anti-protons from the debuncher. After the accumulator has collected a sufficient amount of anti-protons they will be transferred to the recycler which is an 8 GeV storage ring made of permanent magnets. Anti-protons will be transferred from the recycler to the main injector before they are put into the Tevatron.

3.1.6 Tevatron

The Tevatron is the world's highest energy operational particle accelerator. It is roughly 4 miles in circumference, consists of just over 1000 superconducting dipole magnets, and is capable of colliding protons with anti-protons at a center of mass energy of 1.96 TeV.

The Tevatron accepts proton and anti-proton bunches from the main injector at 150 GeV. Protons circulate clockwise in the Tevatron while anti-protons circulate counter-clockwise (as viewed from above). There are 36 bunches of protons and 36 bunches of anti-protons in the Tevatron in usual operation. Each proton bunch typically consists of about 10^{11} protons. The anti-proton bunches are smaller due

to the difficulties in collecting them and typically consist of about 10^{10} anti-protons per bunch.

Once the proton and anti-proton bunches are loaded into the Tevatron, the energy is ramped from 150 to 980 GeV, the beams squeezed, extraneous particles orbiting around the beam (beam halo) removed, and the bunches made to collide head on. The instantaneous luminosity for such collisions can be written as

$$\mathcal{L}_{inst} = fn\frac{N_p N_{\bar{p}}}{4\pi\sigma_x\sigma_y} \tag{3.1}$$

where f is the frequency of revolution, n the number of bunches (36 in this case), N_p ($N_{\bar{p}}$) the number of protons (anti-protons) per bunch, and $\sigma_{x,y}$ are the Gaussian beam profiles in the transverse direction assuming that both p and $\bar{p}$ beams have the same profile and completely overlap. The Tevatron typically achieves initial instantaneous luminosities of $2.8 \times 10^{32}\text{cm}^{-2}\text{s}^{-1}$ with a record initial instantaneous luminosity of $3.3212 \times 10^{32}\text{cm}^{-2}\text{s}^{-1}$ recorded on November 4, 2008. The luminosity essentially gives the available area for interactions. Multiplying the instantaneous luminosity by the cross section for a process gives the rate with which that particular process will occur.

3.2 The CDF II Detector

The CDF II detector is a multi-purpose particle detector. It sits at the B0 location on the Tevatron where protons and anti-protons collide. The CDF II detector consists of different layers, which are designed to measure different properties of

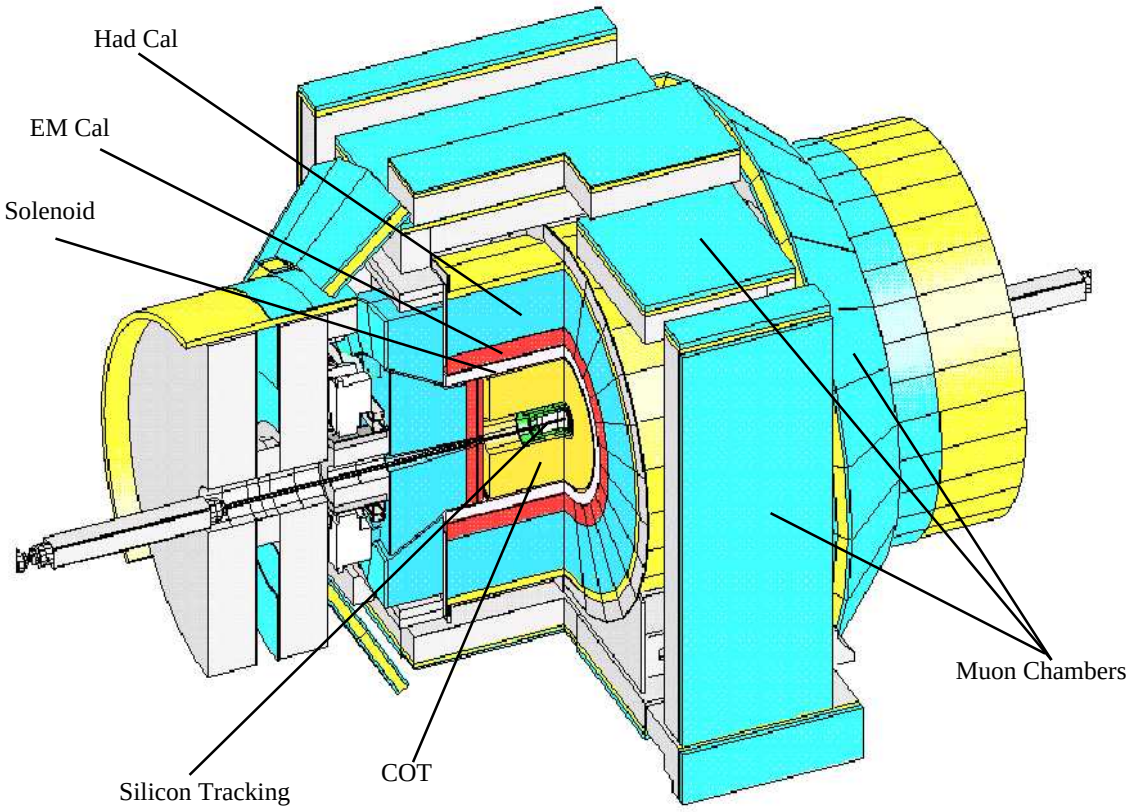

Figure 3.2: The CDF II detector.

particles traversing them. The inner-most layers are made up of tracking detectors inside of a magnetic field which are able to reconstruct the momentum of charged particles. Outside of the tracking volume are the calorimeters, which measure energy deposited by particles as they either stop in or pass through them. The outermost portions of the detector are muon chambers which identify charged particles that have passed through the rest of the detector. A basic picture of the CDF II detector is shown in figure 3.2.

Every 396 nano-seconds a proton bunch and an anti-proton bunch collide in the

middle of the beampipe which lies at the center of the detector. At present time it is not possible to record all of the data which would have to be read out every 396 ns. An online hardware triggering system quickly looks at some of the data for each event and decides if it is an interesting enough event to keep or should be discarded. This significantly reduces the amount of data which must be read out from the detector and written to storage media.

The relevant components of the CDF II detector to this analysis are discussed along with the CDF trigger system in the remainder of this chapter. For more details of various detector components see the CDF II Technical Design Report [10].

3.2.1 The CDF II Coordinate System

The CDF coordinate system is a right handed coordinate system defined such that the positive z direction is in the direction of the proton beam at the nominal (z_0) collision point. The positive y direction is defined to point vertically upward. This leaves the x direction pointing outward (roughly northwest) where unit vectors satisfy $\hat{z} = \hat{x} \times \hat{y}$.

A useful kinematic variable in high energy physics is rapidity, defined as:

$$Y = \frac{1}{2} \ln \left(\frac{E + p_z}{E - p_z} \right). \tag{3.2}$$

Pseudo-rapidity (η) is the massless approximation of this quantity, which for the particles energies considered in this analysis gives an exceedingly good approximation. The pseudo-rapidity is given by setting $E = P$ in equation 3.2 resulting

in:

$$\eta = -\ln\left(\tan\frac{\theta}{2}\right) \tag{3.3}$$

where θ is the polar angle from the z-axis (beam direction). In high energy physics experiments a particles direction is often expressed in terms of η. For example, objects which are more forward (pointed more along the z-axis) have a higher absolute value of pseudo-rapidity and $\eta = 0$ corresponds to $\theta = 90°$. This quantity can be calculated for a particle regardless of what z position it was created at. Another very similar quantity is the detector pseudo-rapidity, η_{det}, which is typically in reference to the pseudo-rapidity as defined from the z_0 of the detector.

3.2.2 Tracking Detectors

There are two types of inner tracking detectors used at CDF II. The innermost detector is a silicon microstrip based detector which provides very precise charged particle tracking and is especially useful for identifying decays which are slightly displaced from the initial interaction point. Outside of this is the central outer tracker (COT) which is a wire drift chamber filled with gas which charged particles will ionize as they traverse the detector. These detectors and their use in this analysis is described below. The tracking detectors are shown in figure 3.3. The entire tracking volume is surrounded by a solenoid which provides a magnetic field of 1.4T in the $\hat{z}$ direction. Charged particles in this volume will travel on helical trajectories and it is the curvature of these orbits which are measured by the tracking detectors. Measuring the curvature is equivalent to measuring the momentum of these particles.

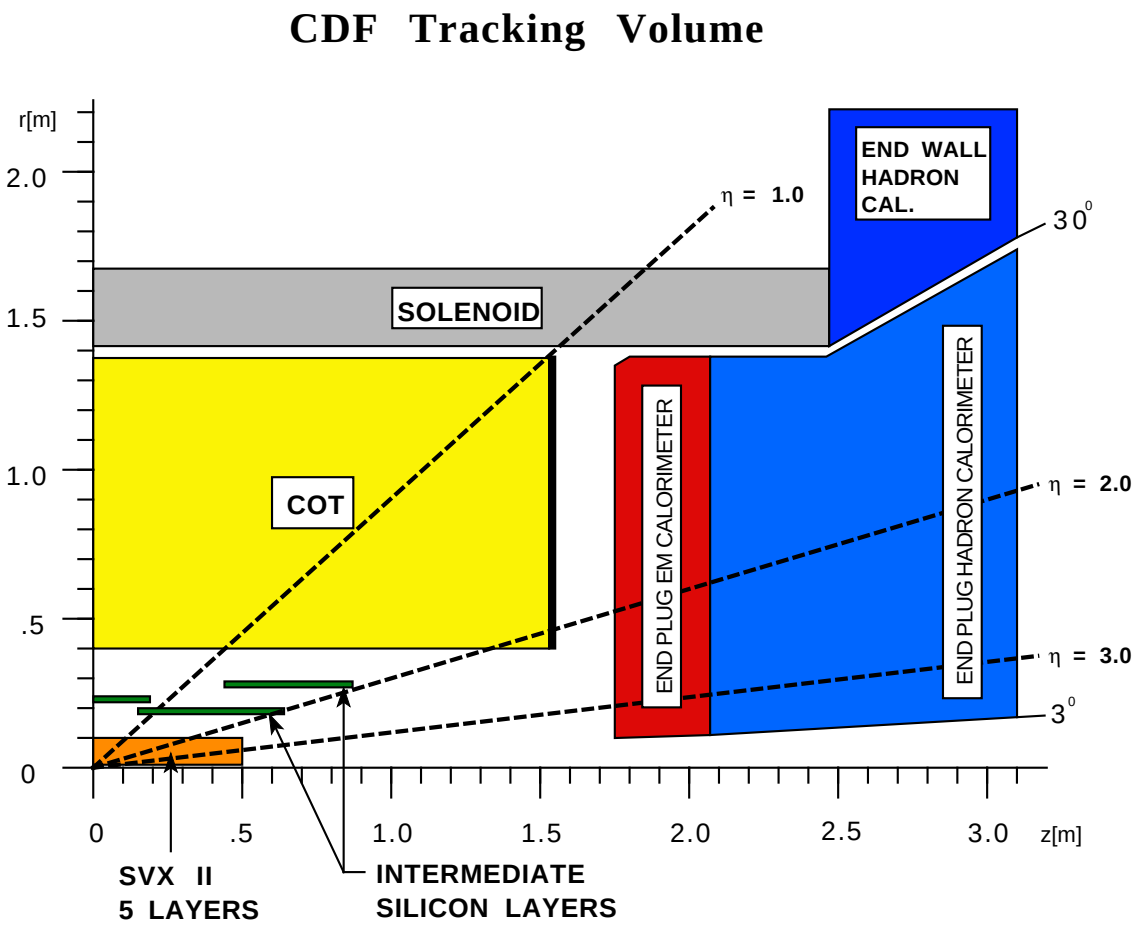

Figure 3.3: Longitudinal view of the CDF II tracking volume and plug calorimeter.

Silicon Tracking Detector

The innermost tracking detector is the silicon detector which consists of 3 major components: L00, SVXII, and the ISL. L00 (layer zero zero) is a single sided silicon micro-strip detector mounted on the beam-pipe at a radius of 1.1 cm. It is 87 cm long centered at $z = 0$ and provides complete coverage in ϕ. The SVXII consists of 5 layers of silicon micro-strip detectors from a radius of 2.44 cm to 10.6 cm. It is 87 cm long which provides coverage out to $|\eta_{det}| < 2.0$ and partial coverage to $|\eta_{det}| < 3.0$. These dual-sided silicon strips in the SVXII provide information in ϕ as well as information in z from the stereo side which is situated at 90° for layers 0, 1, and 3 while the stereo side of layers 2 and 4 are at ±1.2°. The intermediate silicon layers (ISL) sit between the SVXII and the COT occupying the range between 20 and 30 cm. There is one layer which extends out to $|\eta_{det}| < 1$ and two layers covering the range $1 < |\eta_{det}| < 2$.

The silicon tracker is used in this analysis for 2 reasons. First, silicon tracking is used to identify high momentum tracks (presumably from electrons or muons) in the forward region $1 < |\eta| < 2$. Second, it is used to identify jets which have a vertex which is not from the primary interaction point. The displacement of these vertices is typically less than a millimeter, which is too small to be determined from the COT alone.

Central Outer Tracker

The central outer tracker (COT) is an open-cell drift chamber consisting of 96 layers. The COT covers the radial region between 40 and 137 cm. The 96 layers are divided

into 8 super-layers which are alternating axial and stereo super-layers. The stereo layers are angled at $\pm 3^\circ$ and provide z-position information. Each super-layer is subdivided into cells which consist of sense wires, potential wires, shaper wires, and field panels as can be seen in figure 3.4 for super-layer 2. The COT provides charged particle tracking out to $|\eta_{det}| < 1.1$.

The COT is filled with an Argon-Ethane gas mixture. As a charged particle travels through the COT it will ionize the gas. The free electrons are then attracted to the sense wires. As the free electrons migrate toward the sense wires a cascade of electrons are freed from the gas from ionization. This cascade of electrons bombards the sense wires and is counted as a hit. A track can be reconstructed from multiple sense wires with hits and the timing information of those hits. From the curvature of the reconstructed track one can accurately measure the momentum of the charged particle traversing the detector.

The COT by itself has a momentum resolution of $0.15\%P_T$. Combined with the silicon detector the momentum resolution is $0.07\%P_T$. For tracks with a transverse momentum greater than 10 GeV the tracking efficiency of the COT is greater than 99% [16].

In this analysis the COT is particularly useful in identifying high momentum tracks from electrons and muons as well as jets. All central ($|\eta| < 1.1$) leptons identified in this analysis are required to have a good quality track in the COT. Tracking information from the COT is also used at the trigger level to identify events which may contain a high-P_T lepton.

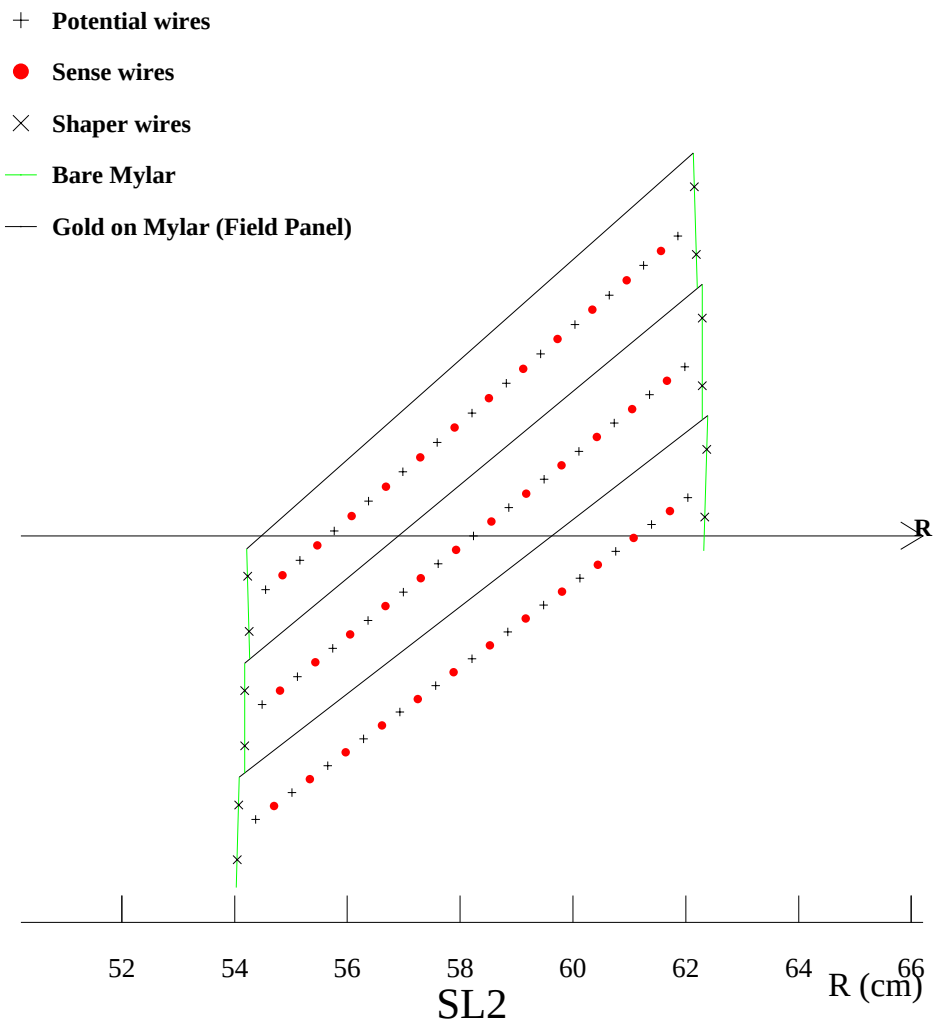

Figure 3.4: A COT cell showing the sense wires, potential wires, shaper wires, and field panels.

3.2.3 Calorimetry

The calorimeters surround the solenoid and tracking volume and measure the energy of particles which stop in or pass through them. The calorimeters consist of layers of scintillator sandwiched between layers of heavy metal. Electrons and photons traversing a calorimeter will interact with the heavy metal which creates a shower of electrons and photons. Similarly, hadrons will shower and deposit their energy in the calorimeters as well (though they will typically travel through more material). This shower excites atoms in the scintillator which then emit photons as they return to their ground state. These photons are then amplified by photomultiplier tubes and the amplitude gives a measurement of the energy deposition.

The central calorimeters cover a pseudo-rapidity range of $|\eta_{det}| < 1.1$ and radially occupy the range from 173 to 347 cm. They consist of an EM (electro-magnetic) portion, a HAD (hadronic) portion, and a shower-maximum detector (CES). Electrons and photons typically deposit most of their energy in the lead layers of the EM portion of calorimeter. The shower maximum sits at a radius of 185 cm and measures a transverse shower profile which is used in electron and photon identification. The hadronic calorimeter is situated behind the EM calorimeter and consists of layers of steel and scintillator.

There are 48 total central calorimeter wedges which each occupy 15° in ϕ (there are 24 on each side of $z = 0$). Each wedge is internally segmented into towers which are 0.1 in η wide.

The energy resolution of the central EM calorimeter is

$$\sigma(E)/E = 13.5\%/\sqrt{E[\text{GeV}] \times \sin(\theta)} + 2\%. \tag{3.4}$$

The CES has a position resolution of 2 mm at 50 GeV. The central hadronic calorimeter has an energy resolution of $\sigma(E)/E = 0.5/\sqrt{E}$.

The forward calorimeter (plug calorimeter) is similar in nature to the central calorimeters. It also consists of an EM portion and a HAD portion as well as a shower-maximum detector, the PES. This detector covers a range in η of $1.1 < |\eta_{det}| < 3.6$. The energy resolution of the EM and HAD portions of the detector are

$$\sigma(E)/E = 13.5\%/\sqrt{E[\text{GeV}] \times \sin(\theta)} + 1\% \tag{3.5}$$

and

$$\sigma(E)/E = 80\%/\sqrt{E[\text{GeV}] \times \sin(\theta)} + 5\%. \tag{3.6}$$

A cross section of the plug calorimeter is shown in figure 3.5.

3.2.4 Muon Detectors

There are three muon detectors used in this analysis: CMU, CMP, and CMX. They are situated in the outermost regions of the detector. The reason for this is that most particles will not penetrate the many layers of lead and steel in the calorimeters. A muon will typically traverse the entire calorimeter depositing only a very small fraction of its energy in it. Muon detectors allow for the identification of a particle which has passed through the entire detector by detecting its position which can then be matched to a track in the tracking detectors. The muon system consists of drift tube chambers and scintillator material which will detect when a charged particle enters the detectors.

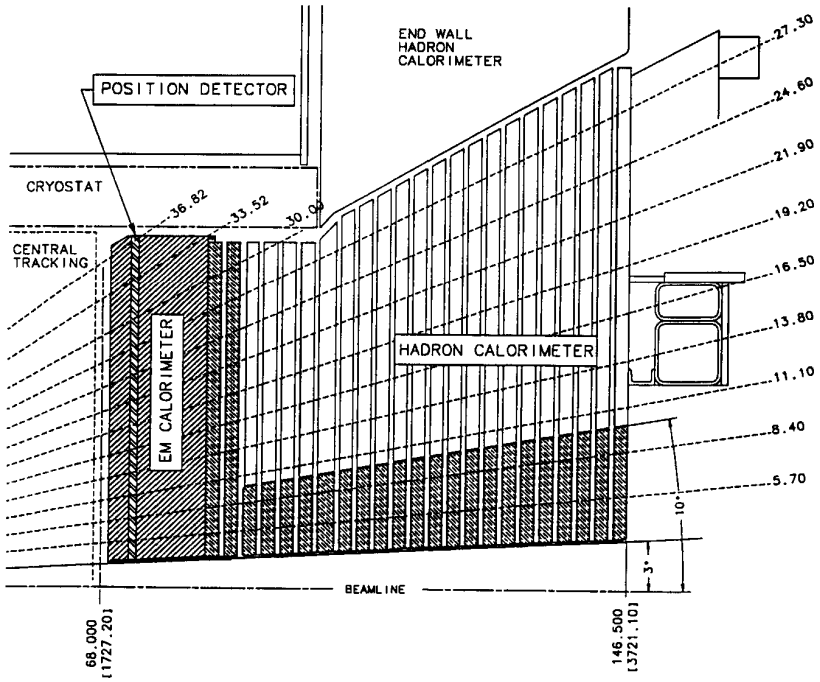

Figure 3.5: Cross sectional view of the plug calorimeter.

The CMU detector is embedded in the outermost region of the central calorimeters and covers a range in η of $|\eta_{det}| < 0.68$ The CMP detector sits outside of this and behind an additional 60 cm of steel absorber. The CMP detector partially overlaps with the CMU detector and it covers a range out to $|\eta_{det}| < 0.68$. This outer detector is used to confirm hits in the CMU detector where they overlap. The CMX detector covers a slightly more forward region in the range of $0.65 < |\eta_{det}| < 1$. The muon system coverage in η_{det} and ϕ is shown for these detectors in figure 3.6.

3.2.5 Luminosity Measurement

The instantaneous luminosity at CDF is measured using the Cherenkov Luminosity Counter (CLC). The CLC consists of 2 m long tubes filled with gas which are situated on either side of the detector at high η_{det}. Charged particles radiate in the gas giving off photons which are collected by photomultiplier tubes. Counting hits in the photomultiplier tubes and knowing the inelastic $p\bar{p}$ cross section allows one to calculate the instantaneous luminosity. The measured error in the CLC combined with the uncertainty in the inelastic $p\bar{p}$ cross section gives a total error of 5.9% where 4% is coming from the uncertainty in the inelastic $p\bar{p}$ cross section [54].

3.2.6 Trigger System

With collisions every 396 ns it is neither possible to fully process every event nor to store every event. For this reason CDF employs a 3-level online trigger system. The goal of this system is to quickly pick out events that may contain interesting properties and store them. This is done using a hardware trigger system at level-1

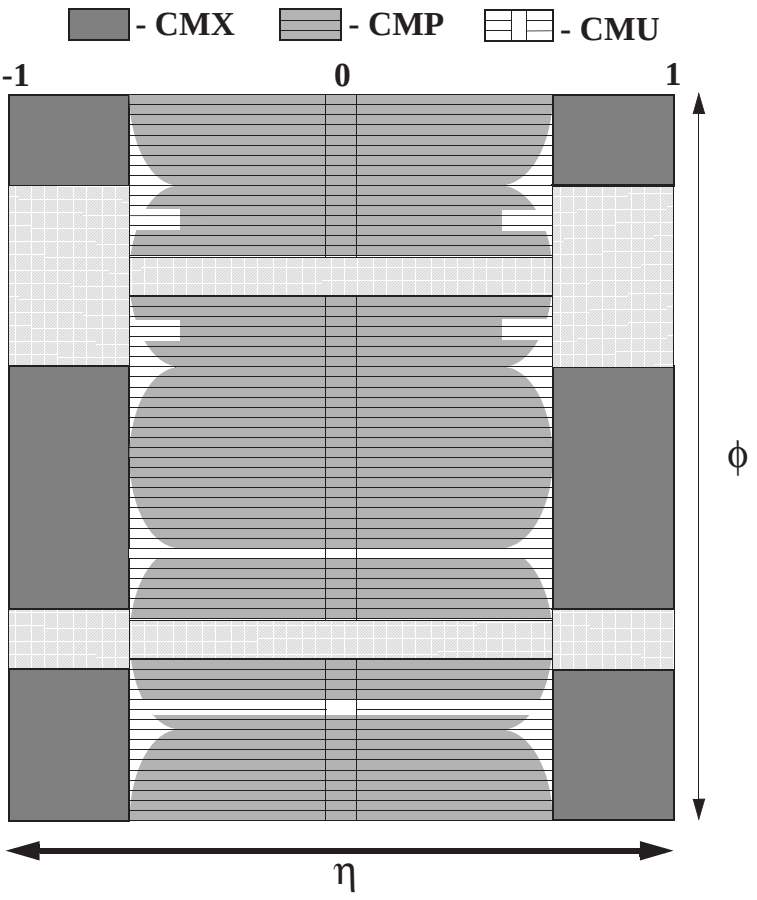

Figure 3.6: Muon system coverage in η_{det} and ϕ for the CMU, CMP, and CMX detectors.

and level-2 and using a farm of computers at level-3. The bunch crossing rate is about 2.5 MHz which must be reduced to a rate of about 100 Hz which is the rate at which events can be recorded.

Level 1

The level-1 trigger uses basic calorimeter information, tracks reconstructed in the COT by the eXtremely Fast Tracker (XFT), and stubs reconstructed in the muon chambers to make a decision about the event. As events stream into level-1 they are placed into a data pipeline which gives the level-1 trigger about 5.5 μs to find tracks, match them to muon stubs, examine calorimeter energy deposits, look at energy imbalances in the calorimeters, and make a decision. If a decision is not reached within that time the event is lost. The maximum accept rate of the level-1 trigger is about 20 kHz.

Level 2

The level-2 trigger has 4 buffers which allows for about 20 μs to make a decision. The level-2 trigger additionally considers tracking information from the silicon detector and shower-maximum detectors as well as has better (but slower) resolution and identification algorithms. The accept rate for the level-2 trigger is about 300 Hz.

Level 3

The level-3 trigger consists of two parts: The Event Builder (EB) and the L3 decision farm. The EB packages the raw detector output and the L3 farm makes decisions based on higher level objects such as clustered calorimeter energies and

more sophisticated tracking from both the COT and silicon detectors. The accept rate for the level-3 trigger is about 75 Hz. Once the level-3 trigger has identified an event which should be kept it is written to permanent storage.

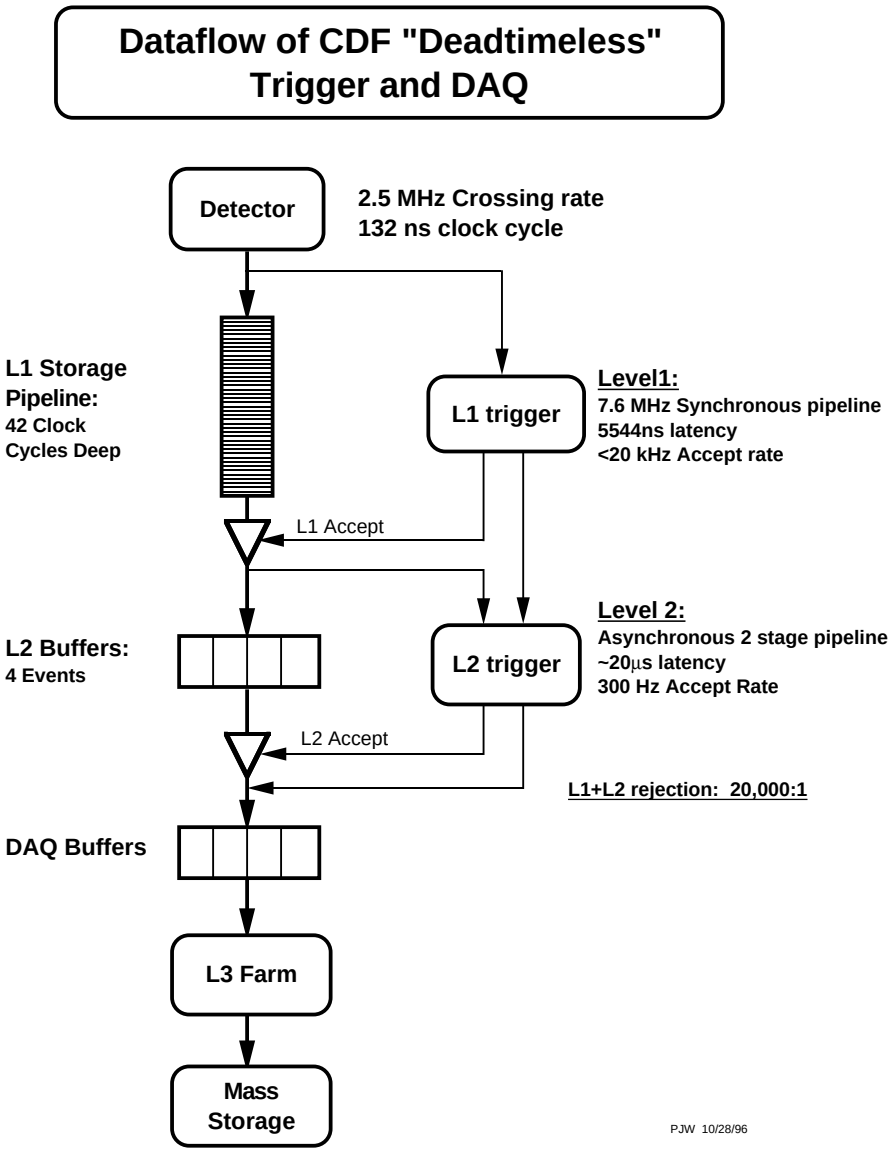

Figure 3.7: Diagram of the CDF II trigger system and data flow.

Chapter 4

High-P_T Object Identification

The starting point for any high-P_T analysis in high energy physics is the careful definition of the objects which one will use in a given analysis. This analysis is fundamentally based on high-P_T leptons (electrons and muons), jets, and missing transverse energy ($\not\!\!E_T$). The lepton types are defined such as to accept as much signal as reasonably possible, which in turn increases the overall sensitivity in terms of possibly finding or excluding a standard model Higgs boson. Once the lepton types are defined, the efficiencies for their identification in both simulation and data must be measured and compared in order to properly account for any possible deficiencies in the simulation. The high-P_T objects used in this analysis are defined in the following sections. The lepton efficiencies and scale factors are discussed in section 4.5 and 4.6.

4.1 Lepton Identification

Two lepton flavors (e and μ) are considered in this analysis. Electrons and muons are categorized by how they are reconstructed in the CDF II detector. There are 7 categorizations in total. TCE and PHX refer to electron types while CMUP,

TCE	Tight Central Electron: $\|\eta\| < 1.1$.
PHX	Forward electron which relies on silicon tracking: $1.2 < \|\eta\| < 2.0$.
CMUP	Central muon which has hits in both the CMU and CMP muon detectors: $\|\eta\| < 0.6$.
CMX	Muon which has hits in the CMX detector: $0.65 < \|\eta\| < 1.0$.
CMIOCES	Muon which does not satisfy the hit requirements of CMUP or CMX but is fully fiducial to the central calorimeter.
CMIOPES	Similar to CMIOCES, but in the forward region.
CrkTrk	High P_T track which points to a crack in the detector. It is assumed to be either an electron or a muon.

Table 4.1: Brief description of each lepton category used in this analysis.

CMX, CMIOCES, and CMIOPES refer to muon types. CrkTrk is the remaining type which is a high-P_T track that enters into a crack in the calorimeter coverage and is presumed to be either an electron or a muon. A very brief outline of these lepton categories is given in table 4.1. Electron, muon, and track identification are discussed further in sections 4.1.1, 4.1.2, and 4.1.3 respectively. These lepton categories and the tools used to identify them preceded this analysis. They were first introduced in order to increase the acceptance from the standard CDF lepton selection for WW and WZ analyses [48].

In addition to the identification requirements listed in sections 4.1.1, 4.1.2

and 4.1.3, a track isolation requirement is made on all lepton types other than PHX electrons (see below). This isolation requirement is given by

$$\frac{\sum_{i\neq seed}^{N} P_T^i}{P_T^{seed}} < 0.1 \tag{4.1}$$

where N is the number of tracks within a cone or $\Delta R < 0.4$ of the seed (or candidate) track. This requirement helps reduce the number *fake* leptons accepted and is satisfied by almost all leptons from W or Z decays.

4.1.1 Electron Identification

High-P_T electrons traversing the CDF II detector are expected to leave a track in both the silicon detector as well as the COT. Electrons, having a relatively low mass and being electrically charged, will deposit most of their energy into the EM portion of the calorimeter. An electromagnetic cluster with a reconstructed track pointing to it is essentially the starting point for electron identification, further details of which are explained in this section.

In this analysis electrons are identified in both the central ($|\eta| < 1.1$) and forward ($1.1 < |\eta| < 2.0$) regions. Table 4.2 gives the specific quantitative values for the parameters used to select both Tight Central Electrons (TCE) and forward (PHX) electrons. PHX electrons are named after the PHOENIX algorithm used to identify forward electrons by matching plug EM calorimeter information to SVX hits. The meanings of identification variables are given below.

- Region : A flag indicating if the track is fiducial to the central or plug calorimeters. This flag comes from the FidEle routine in CDF offline software.

Central Electrons (TCE)	
Region	Central ($\|\eta\| < 1.1$)
Fiducial	Track fiducial to CES
Track P_T	≥ 10 or ≥ 5 if $E_T < 20$ (GeV)
Track $\|z_0\|$	≤ 60 cm
# Axial SL	≥ 3 with ≥ 5 hits
# Stereo SL	≥ 2 with ≥ 5 hits
Conversion Flag	$\neq 1$
Isolation/E_T	≤ 0.1
E_{HAD}/E_{EM}	$< 0.055 + 0.00045 \cdot E$
L_{shr}	≤ 0.2
E/P	$< 2.5 + 0.015 \cdot E_t$
CES ΔX	$-3 \leq q \cdot \Delta X \leq 1.5$

Forward Electrons (PHX)	
Region	Plug
η_{PES}	$1.2 < \|\eta\| < 2$
E_{HAD}/E_{EM}	< 0.05
PEM 3x3 Fit	true
χ^2_{PES}	≤ 10
PES 5x9 U	≥ 0.65
PES 5x9 V	≥ 0.65
Isolation/E_T	≤ 0.1
ΔR(PES,PEM)	≤ 3.0
Track Matched	true
# of Silicon hits	≥ 3
Track $\|z_0\|$	≤ 60 cm

Table 4.2: Central (TCE) and forward (PHX) electron identification requirements.

- Fiducial : In the case of TCE the track must be fiducial to the CES.

- Track P_T : The transverse component of the momentum which is measured explicitly using the track curvature.

- Track z_0 : The longitudinal (z) position of the track where it intersects the beamline.

- Axial and Stereo SL : The number of axial and stereo superlayers in the COT which have at least 5 hits associated with this track.

- Conversion flag : A routine is implemented to identify electrons which may have come from photon conversion [6]. These electron candidates have their conversion flag set to one and are rejected.

- Isolation/E_T : The energy deposited in the calorimeter in a cone of radius $\Delta R \leq 0.4$ around the electron cluster (muon track) excluding the energy of the electron cluster energy (deposited by the muon) divided by the E_T (P_T) of the electron (muon) candidate.

- E_{HAD}/E_{EM} : The ratio of energy which is deposited in the hadronic (CHA or WHA) portion of the calorimeter to the energy deposited in the electromagnetic (CEM or PEM) portion of the calorimeter.

- L_{shr} : A variable that compares the lateral shower profile in towers next to the seed tower to an expected profile given by

$$L_{shr} = 0.14 \frac{\sum_i (M_i - P_i)}{\sqrt{(0.14\sqrt{E_{EM}})^2 + \sum_i (\Delta P_i)^2}} \tag{4.2}$$

where i denotes the adjacent towers, M_i the measured energy, and P_i the predicted energy in the ith tower [66].

- E/P : The ratio of the energy measured in the calorimeter to the momentum calculated from the measurement of the track curvature.
- CES ΔX : The difference in the $r-\phi$ plane between the best CES match and the COT beam-constrained track extrapolation to the CES.
- η_{PES} : The pseudo-rapidity as measured by the best matched PES cluster.
- PEM 3x3 Fit : A χ^2 fit to electron test beam data of 9 PEM towers.
- χ^2_{PES} : A χ^2 fit to electron test beam data for shower-maximum profile
- PES 5x9 U/V : The ratio of the central 5 tower energy to the total 9 tower energy.
- ΔR(PES,PEM) : The difference in the $r-\phi$ plane between the best PES match and the PEM measurement.
- Track Matched : PHX electrons must have a track that is matched to the PEM cluster and event vertex.
- # of Silicon hits : The number of hits in the silicon detector associated with a specific track. The maximum number of hits is 8 (for L00, SVX, and ISL combined).

4.1.2 Muon Identification

Muons are minimum ionizing particles which can traverse the entire CDF II detector. Muons are characterized by the track they leave in the tracking volume, very little energy deposited in the calorimeter which they pass through, and in cases where they are fiducial to muon chambers they will also leave track, often called a *stub*, in these detectors.

This analysis considers four categories of muons: CMUP, CMX, CMIOCES, and CMIOPES. These types are essentially defined by (and named after) the detectors which they pass through. The detectors have different components, geometry, location, and hence different detector efficiencies and resolutions. Because of this the efficiencies are determined separatelyn for each category. These efficiencies are discussed further in section 4.5.

Some real muons may fall under the categorization of CrkTrk which is discussed in section 4.1.3. All muons must satisfy the base requirements listed in table 4.3. Muons are further categorized by the fiduciality of the high-P_T track to the muon detectors (CMU and CMP in the case of a CMUP muon and CMX in the case of a CMX muon). CMUP muons are required to have a stub in both the CMU detector which is confirmed by the outer CMP muon chambers. These cover a pseudo-rapidity range $|\eta_{det}| < 0.68$. CMX muons are required to have a stub in the CMX detector, which covers the range $0.65 < \eta_{det} < 1$

In cases where the track does not point to a reconstructed stub or is not fiducial to these muon detectors it is still possible to identify muons using a high-P_T track pointing to calorimeter energy consistent with that of a minimum ionizing particle,

but without the additional muon stub information. As expected, the probability of another object faking such muons is larger than for the CMUP and CMX categories (see section 4.4). In these cases the track must be fiducial to the central (for the CMIOCES category) or forward (for the CMIOPES category) calorimeters. Note that in the cases where a track is not CMUP but either CMU-only or CMP-only it will fall into the CMIOCES category and the stub information is not used (this could potentially change in the future).

Additional requirements for the four categorizations of muons are given in table 4.4. The meanings of the different cuts (which have not already been described in section 4.1.1) are given below.

- CM(U|P|X) x_{fid}, z_{fid} : The extrapolation of the track to the relevant muon detector is required to be fiducial to the detector and in the case of CMX must also not be within 3 cm in z_{fid} of the edge of the detector. Note: These coordinates refer to the face of the specific muon detector and not the CDF II coordinate system.

- $\Delta X_{\mathrm{CM(U|P|X)}}$: The distance between the actual stub in a given muon detector and the track position extrapolated to that detector.

- ρ_{COT} : The radius at which the track appears to leave the COT. This value is required to ensure that these muons are a type which can be triggered on by the CMX trigger track requirements.

- d_0 : The distance of closest approach of the fitted track to the beamline.

- χ^2 : This chi-squared compares the fitted track to the hit information in the

Base Muon Selection	
P_T	> 10 GeV
E_{EM}	$< 2 + \max(0, (p - 100) \cdot 0.0115)$
E_{Had}	$< 6 + \max(0, (p - 100) \cdot 0.028)$
Isolation/P_T	≤ 0.1
# Axial SL	≥ 3 with ≥ 5 hits
# Stereo SL	≥ 2 with ≥ 5 hits
Track $\lvert z_0 \rvert$	< 60 cm
Track $\lvert d_0 \rvert$	< 0.2 cm (< 0.02 cm with silicon)
χ^2/dof	< 4.0 (< 3.0 if Run > 186598)

Table 4.3: Base identification requirements for all muon types.

tracking detectors.

- Curvature significance : The measured track curvature divided by the curvature error.

4.1.3 Identification of Tracks of Unknown Lepton Types

In order to recover some of the lost acceptance due to uninstrumented regions or gaps in the calorimeter, high-P_T tracks which enter such "cracks" are counted in this analysis in a separate category (CrkTrk). These CrkTrk objects are predominantly electrons and muons that were otherwise unidentified, and are treated as such in this analysis. The definition of CrkTrk used here requires a well measured track which specifically points to a crack in the calorimeter as well as little calorimeter or track activity near the primary track. The identification requirements for CrkTrk leptons are given in table 4.5. As mentioned above a track isolation requirement (equation 4.1) is also made which is important for reducing the CrkTrk fake rate (see section 4.4) since this category does not have reliable calorimeter information

CMUP Muon	
CMU Fid	$x_{fid} < 0$, $z_{fid} < 0$ cm
CMP Fid	$x_{fid} < 0$, $z_{fid} < 0$ cm
ΔX_{CMU}	< 7 cm
ΔX_{CMP}	$< max(6, 150/P_T)$ cm

CMX Muon	
CMX Fid	$x_{fid} < 0$, $z_{fid} < -3$ cm
ΔX_{CMX}	$< max(6, 125/P_T)$ cm
ρ_{COT}	> 140 cm

CMIOCES Muon	
Uniqueness	Not a CMUP or CMX
$E_{EM} + E_{Had}$	> 0.1 GeV
# Stereo SL	≥ 3 with ≥ 5 hits
Fiducial	Track fiducial to CES
χ^2/dof	< 3.0

CMIOPES Muon	
Uniqueness	Not a CMUP or CMX
$E_{EM} + E_{Had}$	> 0.1 GeV
# Stereo SL	≥ 3 with ≥ 5 hits
Fiducial	Track fiducial to PES
COT hit fraction	> 0.6
Curvature significance	> 12.0

Table 4.4: Identification requirements for the various muon types.

CrkTrk	
Isolation/P_T	≤ 0.1 using CDF Muon or ≤ 0.1 using nearest EM cluster, $\Delta R < 0.05$
# Axial SL	≥ 3 with ≥ 5 hits
# Stereo SL	≥ 3 with ≥ 5 hits
Track $\lvert z_0 \rvert$	< 60 cm
Track $\lvert d_0 \rvert$	< 0.2 cm (< 0.02 cm with silicon)
χ^2/dof	< 3.0
Uniqueness	Not a CMUP or CMX
In Crack	Not CES or PES fiducial
Conversion	$\neq 1$

Table 4.5: Identification requirements for high-P_T tracks which are fiducial to a crack in the calorimetry (CrkTrk).

for further lepton identification. Since these tracks are not expected to leave any large fraction of their energy in the calorimeter they are treated the same as muons in any $\not\!\!E_T$ corrections which are discussed in 4.3.

4.2 Jet Identification

Jets are the result of the recombination and hadronization of quarks or gluons leaving the interaction point. In the CDF II detector jets are characterized by large localized energy deposits in both the electromagnetic and hadronic calorimeters as well as often having several collimated tracks pointing to these calorimeter clusters.

In this analysis a jet is defined as a calorimeter cluster of size $\Delta R < 0.4$ which has a total corrected transverse energy of $E_T > 15$ GeV and is within a pseudo-rapidity of $|\eta| < 2.5$. The raw detector energy for each jet is corrected for nonlinearaties in

calorimeter towers and energy loss in the uninstrumented portions of the detector[1]. The *absolute* scale corrections applied in this analysis are described in detail in [26]. Identified electrons will always satisfy the jet requirements and for this reason an object is not counted as a jet if it is within $\Delta R < 0.4$ of an already identified electron.

4.3 Missing Transverse Energy ($\not\!\!E_T$)

Neutrinos produced in the final state interact with matter only via the weak interaction and hence escape without detection carrying away with them some amount of energy which cannot be directly measured. A neutrino leaving the detector can however leave an energy imbalance in the detector. These neutrinos are the source of *real* missing energy. Since the z-component of momentum of the interacting partons within the protons are unknown one cannot determine the total z-component of the net "missing" energy. However, the momentum in the transverse plane is well known (*i.e.* is zero to a very good approximation) and is therefore what is used to define transverse missing energy.

The *raw* missing transverse energy ($\not\!\!E_T$) is defined as

$$\vec{\not\!\!E}_T^{raw} = -\sum_i \vec{E}_T^i \tag{4.3}$$

where $\vec{E}_T^i$ refers to the transverse component of the energy in the ith calorimeter tower as defined at $z_0 = 0$. At the trigger level the magnitude of $\not\!\!E_T^{raw}$ is used,

[1]Jet energy corrections are performed using the standard CDF JetUser package version jetCorr15.

however there are important corrections applied to this definition at the analysis level. The largest correction is due to muons which are minimum ionizing particles which do not leave much energy in the calorimeter and hence leave an apparent missing energy as most of their energy is carried away as they leave the detector. The $\not\!\!E_T$ is corrected for muons identified according to section 4.1.2 by adding back their track momentum measurement and subtracting any small amount of energy which they may have deposited in the calorimeters. High-P_T tracks which have been identified as CrkTrk leptons are treated the same as muons in this calculation since they enter a crack in the calorimeter. The $\not\!\!E_T$ is also modified to account for the corrections to raw jet energies discussed in section 4.2. The $\not\!\!E_T$ used at the analysis level is then

$$-\vec{\not\!\!E}_T = \sum_i \vec{E}_T^i + \sum_\mu \vec{P}_T^\mu - \sum_\mu \vec{E}_T^\mu(\text{Em} + \text{Had}) + \sum_j \vec{E}_T^j(\text{jet correction}) \qquad (4.4)$$

where the E_T have been corrected for the actual interaction z_0 since the transverse components are calculated according to $\sin\theta$ and vertex away from $z = 0$ will give a different θ.

The source of real $\not\!\!E_T$ in this analysis is from neutrinos created in electroweak interactions. There are also several sources of false $\not\!\!E_T$ which are often difficult to control. These sources include the mismeasurement of jet and lepton energies as well as when a lepton or photon enters a crack in the detector where it would not be possible to reconstruct its energy with any reasonable accuracy. The $\not\!\!E_T^{spec}$ ($\not\!\!E_T$ "special") cut used in this analysis is designed to minimize the impact of lepton and jet energy mismeasurement to the $\not\!\!E_T$ calculation. This is described further in

section 5.5.1.

4.4 Fake Lepton Probabilities

Occasionally a jet will pass the lepton selection criterion for a given lepton type. Due to the difficulty in modeling these low probability occurrences, the combination of Monte Carlo programs and CDF II simulation tend to give an unreliable estimate of this type of background. The probability with which a jet-like object will pass a particular lepton selection and falsely be counted as a real lepton is estimated from data samples which are dominated by QCD jets. These are the so-called *jet samples*. Four different jet-samples are used which correspond to different trigger requirements on the leading jet E_T which are 20, 50, 70, and 100 GeV jet based triggers respectively.

The prescription for determining this fake probability is to look at each jet sample independently and count the number of jet-like objects which pass a very minimal subset of the lepton ID cuts which are given in table 4.6. These objects will be counted as N^{Denom}. The probability is then the ratio of the number of these objects which pass the full lepton selection (N^{Pass}) to the number of these *denominator objects* (N^{Denom}). Additionally, this probability is corrected for electroweak contributions by estimating the number of real leptons which should appear in each of the jet samples from W and Z production, N_{EWK}. The estimated real lepton contribution from W and Z production is then subtracted from both the numerator

Fakeable Electrons
$E_T > 10$ GeV
$E_{Had}/E_{EM} < 0.125 + 0.00045 \times E$
Isolation < 0.3
Has a good quality track
Is not a conversion
Fiduciality

Fakeable Muons
Axial SL ≥ 2 with ≥ 5 hits
Stereo SL ≥ 2 with ≥ 5 hits
$P_T > 10$ GeV
Track $\lvert z_0 \rvert < 60$ cm
Track $\lvert d_0 \rvert < 0.2$ cm (< 0.02 cm with silicon)
$E/P < 1$
$\chi^2/dof < 4.0$ (< 3.0 if Run > 186598)
Fiduciality

Table 4.6: Fakeable object denominator definitions. The objects are also required to satisfy the fiducial requirements of each lepton type for which it is a fakeable object.

and denominator. The fake probability is then given by

$$P_{fake} = \frac{N^{Pass} - N^{Pass}_{EWK}}{N^{Denom} - N^{Denom}_{EWK}}. \tag{4.5}$$

In order to avoid any bias which the trigger might introduce, the leading jet is neither considered in N^{Denom} nor N^{Pass}.

The electroweak contribution is estimated using inclusive W and Z Monte Carlo sample generated using PYTHIA. Counting the number of events in these samples which have an identified jet that passes the trigger requirement for a given jet sample along with an identified lepton gives an estimate of the electroweak contribution.

The four jet samples give four independent measurements of the fake probability,

Fake Probabilities

Type	$10 \leq P_T < 20$	$20 \leq P_T < 40$	$40 \leq P_T < 80$	$P_T \geq 80$
TCE	3.0 ± 0.3	1.4 ± 0.4	1.0 ± 0.3	2.7 ± 0.2
PHX	6.2 ± 1.3	3.5 ± 0.8	2.7 ± 0.8	4.1 ± 0.5
CMUP	0.8 ± 0.1	1.6 ± 0.7	1.6 ± 0.6	1.6 ± 0.5
CMX	1.1 ± 0.2	1.8 ± 0.7	1.2 ± 1.0	0.1 ± 2.6
CMIOCES	1.4 ± 0.1	1.3 ± 0.4	0.8 ± 0.3	1.1 ± 0.1
CMIOPES	3.2 ± 0.6	7.4 ± 1.8	4.5 ± 1.9	0.4 ± 0.8
CrkTrk	11.9 ± 0.6	10.5 ± 2.1	7.4 ± 1.6	9.3 ± 0.4

Table 4.7: Fake probabilities for each denominator type by P_T or E_T given in %.

which are parametrized by P_T for muons and E_T for electrons. The fake probabilities used in this analysis are then an average of the fake probabilities from the four jet samples for each lepton denominator type. The uncertainty is estimated by adding a parameter α to the statistical uncertainty ($\sqrt{\text{stat.} + \alpha}$) in each P_T bin until all jet samples agree at the 1σ level. The fake probabilities are given in table 4.7 and shown graphically in figures 4.1 and 4.2.

These fake probabilities are the probability with which a denominator object will fake a lepton, but the probability with which a generic jet fakes a lepton is much lower than the fake probabilities quoted here. The probability with which a generic jet will fake an electron or muon is on the order of 10^{-3} and 10^{-4} respectively. One can vary the denominator definitions and obtain different fake probabilities, but as long as this variation is reasonable should give a similar fake yield prediction when the probabilities are applied to the denominator objects in a "fakeable" sample of events. The application of fake probabilities is discussed further in section 4.4.1.

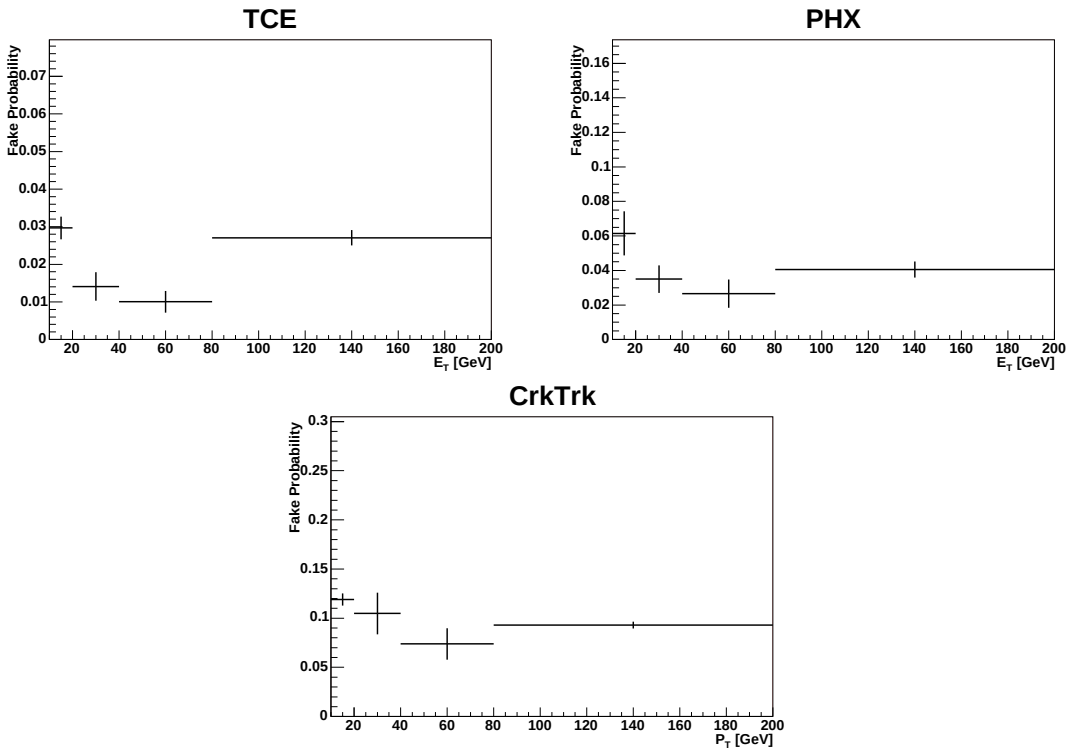

Figure 4.1: Average fake probabilities for each electron category and CrkTrk used in this analysis. These fake rates are calculated using jet triggered data samples.

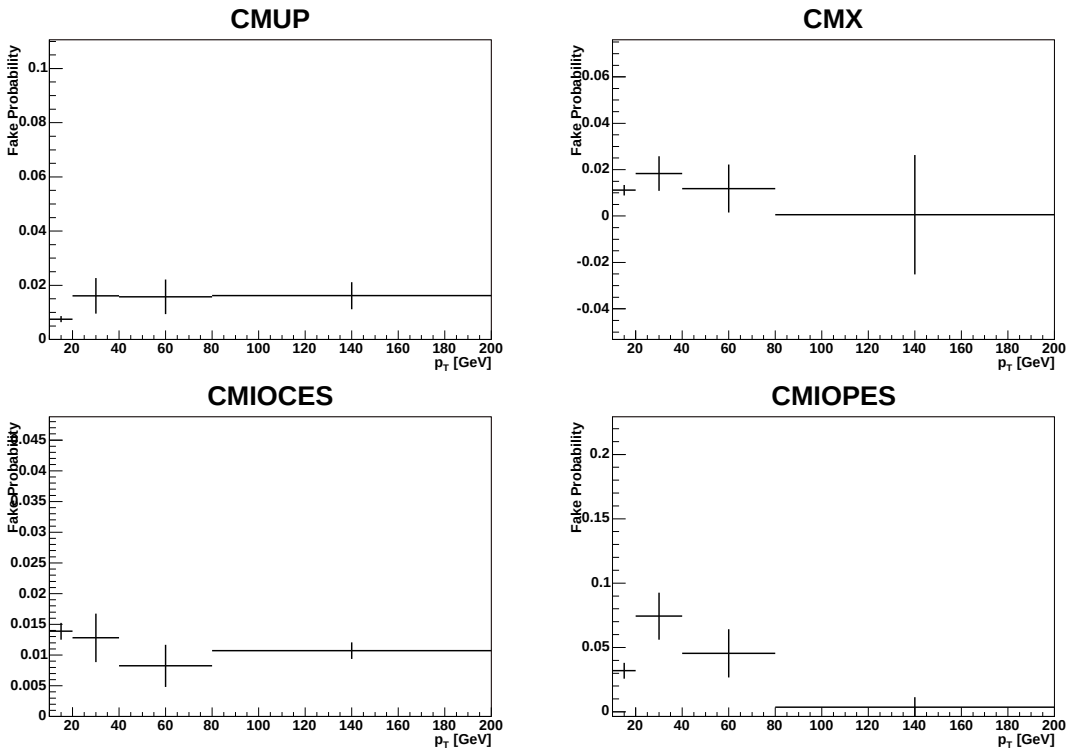

Figure 4.2: Average fake probabilities for each muon category used in this analysis. These fake rates are calculated using jet triggered data samples.

4.4.1 Application of Fake Probabilities

Once the fake probabilities are known they are applied to a data sample consisting of one identified trigger lepton and one or more jets that have passed the "denominator" requirements or table 4.6. This event is then propagated through the analysis, but given a weight equal to the appropriate fake probability. If a denominator object can fake different lepton categories they are counted in each category. If there are multiple denominator objects in the event they are all considered.

Not all lepton plus denominator objects are triggerable, however if the denominator object *had* faked a lepton it may also pass a lepton trigger. Consider the case where an event in the dilepton sample is of type TCE-CMIOPES, but where the TCE was a jet which faked a TCE (electron). This event would be picked up by the central electron trigger. In counting fakes from a lepton+jets sample which requires a lepton trigger this event would be missed if the fakeable object were of type TCE. To account for such non-triggerable fakes in the lepton+jets sample a scale factor derived from the number of triggerable and non-triggerable fakes in Monte Carlo is used. These scale factors are given in table 4.8

4.5 Lepton Efficiencies

All lepton efficiencies are measured using Drell-Yan events which have two electrons or two muons in the final state. This provides a high statistics sample of clean events in the data with which to measure these efficiencies. The efficiencies are measured in both data and Drell-Yan Monte Carlo samples. These efficiencies are then compared and a correction applied to the Monte Carlo predictions to account

	Base	Base Same Sign	Base Low $\not\!\!E_T^{sig}$
TCE-TCE	0.04 ±0.00	0.04 ±0.00	0.02 ±0.00
TCE-PHX	0.04 ±0.00	0.04 ±0.00	0.01 ±0.00
PHX-PHX	0.03 ±0.01	0.03 ±0.01	0.02 ±0.00
TCE-CMUP	0.04 ±0.00	0.04 ±0.00	0.04 ±0.01
TCE-CMX	0.04 ±0.01	0.04 ±0.01	0.00 ±0.00
TCE-CMIOCES	0.22 ±0.01	0.21 ±0.01	0.25 ±0.03
TCE-CMIOPES	0.18 ±0.01	0.18 ±0.01	0.19 ±0.03
PHX-CMUP	0.03 ±0.00	0.03 ±0.00	0.03 ±0.01
PHX-CMX	0.03 ±0.01	0.03 ±0.01	0.00 ±0.00
PHX-CMIOCES	0.41 ±0.03	0.40 ±0.03	0.62 ±0.10
PHX-CMIOPES	0.32 ±0.03	0.32 ±0.03	0.63 ±0.11
CMUP-CMUP	0.05 ±0.02	0.06 ±0.02	0.09 ±0.02
CMUP-CMX	0.05 ±0.02	0.06 ±0.02	0.09 ±0.02
CMUP-CMIOCES	0.50 ±0.06	0.49 ±0.06	0.47 ±0.06
CMUP-CMIOPES	0.54 ±0.07	0.53 ±0.07	0.59 ±0.08
CMX-CMX	0.00 ±0.00	0.00 ±0.00	0.00 ±0.00
CMX-CMIOCES	0.48 ±0.07	0.43 ±0.07	0.37 ±0.07
CMX-CMIOPES	0.27 ±0.05	0.27 ±0.05	0.33 ±0.08
TCE-CrkTrk	0.06 ±0.00	0.06 ±0.00	0.08 ±0.00
PHX-CrkTrk	0.12 ±0.01	0.11 ±0.01	0.12 ±0.01
CMUP-CrkTrk	0.21 ±0.02	0.21 ±0.02	0.21 ±0.02
CMX-CrkTrk	0.10 ±0.01	0.10 ±0.01	0.12 ±0.02

Table 4.8: Ratio of non-triggerable to triggerable fakes by category for the base region and two control regions (see sections 5.5 and 5.6.

Loose TCE	Loose PHX Trk	Loose PHX PEM
$E_T > 10$ GeV $P_T > 5$ GeV $\|z_0\| < 60$ cm	$E_{Had}/E_{EM} \leq 0.05$ PEM 3x3 FitTower = true PEM 3x3 $\chi^2 \leq 10$ PES 5x9 U/V ≥ 0.65 Isolation/$E_T \leq 0.1$ $\Delta R(\text{PES}, \text{PEM}) \leq 3.0$	$E_T > 10$ GeV $E_{Had}/E_{EM} \leq 0.125$ $1.2 < \eta^{2d}_{\text{PES}} < 2.0$ Has a PHX Track N silicon hits ≥ 3 $\|z_0\| < 60$ cm

Loose CMUP/CMX	CMIO(C|P)ES/CrkTrk
Stub: CMUP/CMX Fiducial CMUP/CMX $P_T > 10$ GeV $\|z_0\| < 60$ cm	Axial SL ≥ 3 with ≥ 5 hits Stereo SL ≥ 3 with ≥ 5 hits $P_T > 10$ GeV $\|z_0\| < 60$ cm

Table 4.9: Loose (denominator) definitions used to measure the identification efficiencies for different lepton types.

for any differences in the measured efficiencies from data and Monte Carlo. These correction factors derived from the Drell-Yan samples are applied to all simulated processes. Note that these corrections are not applied to the W+jets background since they are derived from data.

4.5.1 Tag and Probe

In order to isolate Drell-Yan events (particularly in the data, but the same selection is performed on the MC) first one tight lepton is selected as described in section 4.1. Then one looks for a second lepton which satisfies the much looser identification cuts given in table 4.9. If the tight lepton and other loosely selected object have an invariant mass in the Z-mass window ($76 < M_{\ell\ell} < 106$ GeV) then it is considered (or tagged) as a Z event and will be counted in the denominator of the efficiency measurement.

Once a Z event has been identified the loose leg is tested to see if it satisfies

Lepton Type	ϵ_{ID} (Data)
PHX Trk	0.887 ± 0.003
PHX PEM	0.799 ± 0.004
TCE	0.771 ± 0.005
CrkTrk e Iso	0.780 ± 0.012
CMX Reco	0.996 ± 0.014
CMX ID	0.860 ± 0.012
CMUP Reco	0.901 ± 0.007
CMUP ID Trk	0.884 ± 0.006
CMIOCES ID	0.353 ± 0.004
CMIOPES ID	0.827 ± 0.012
CrkTrk μ	0.845 ± 0.011

Table 4.10: Efficiencies for lepton identification as measured in the data.

the full lepton selection requirements as defined in section 4.1. The identification efficiency is given by

$$\epsilon_{ID} = \frac{2N_{TT}}{2N_{TT} + N_{TF}} \tag{4.6}$$

where N_{TT} is the number events which have two leptons which pass the full lepton selection and N_{TF} the number of events where the loose leg failed to pass all of the identification cuts.

The efficiency for PHX electrons is the product of two efficiencies, PHXTrk and PHXPEM. These refer to the tracking efficiency and calorimeter efficiencies which are measured independently. Similarly, the identification and muon stub reconstruction efficiencies (CMUP/CMX ID and CMUP/CMX Reco) for CMUP and CMX muons are measured independently.

An example of the efficiencies from data and Monte Carlo is given in table 4.10. In the analysis itself only the ratio of these efficiencies is used which are given in section 4.6.

Lepton Category	Period 0	Period 1-4	Period 5-7	Period 8-10
CMUP ID	1.027 ± 0.011	0.995 ± 0.008	0.986 ± 0.010	0.991 ± 0.007
CMUP Reco	0.944 ± 0.007	0.936 ± 0.007	0.938 ± 0.009	0.956 ± 0.006
CMX ID	1.013 ± 0.014	0.985 ± 0.013	0.994 ± 0.016	1.002 ± 0.010
CMX Reco	1.013 ± 0.008	1.014 ± 0.010	1.014 ± 0.012	0.998 ± 0.010
CMIOCES	1.049 ± 0.019	1.050 ± 0.016	1.078 ± 0.019	1.046 ± 0.013
CMIOPES	1.028 ± 0.012	0.994 ± 0.012	1.013 ± 0.014	0.985 ± 0.011
CrkTrk μ	0.953 ± 0.013	0.973 ± 0.010	0.963 ± 0.013	0.960 ± 0.010
TCE	1.009 ± 0.006	0.994 ± 0.005	0.987 ± 0.007	0.974 ± 0.005
PHXTrk	0.999 ± 0.005	1.008 ± 0.004	1.016 ± 0.005	0.999 ± 0.003
PHXPEM	0.951 ± 0.006	0.953 ± 0.005	0.943 ± 0.006	0.931 ± 0.004
CrkTrk e	0.934 ± 0.015	0.958 ± 0.014	0.932 ± 0.017	0.912 ± 0.013

Table 4.11: Lepton ID scale factors with and without track isolation cuts for data periods 0-10. No track isolation cut is applied to the PHX category.

4.6 Lepton ID Scale Factors

The ratio of ID efficiencies (ϵ_{ID}) measured in data and Monte Carlo is the scale factor used later when calculating overall acceptances (discussed in section 5.4.1). This is defined as

$$s_{\text{lep}} = \frac{\epsilon_{ID}^{\text{data}}}{\epsilon_{ID}^{\text{MC}}}. \tag{4.7}$$

These scale factors are calculated for different periods in data taking. Tables 4.11 and 4.12 give the actual scale factors applied to the Monte Carlo samples. Their application and corrections are further discussed in section 5.4.1.

Lepton Category	Period 11-12	Period 13	Period 14-17
CMUP ID	0.966 ± 0.008	0.975 ± 0.009	0.983 ± 0.007
CMUP Reco	0.940 ± 0.008	0.948 ± 0.008	0.925 ± 0.007
CMX ID	0.979 ± 0.014	0.998 ± 0.015	0.967 ± 0.014
CMX Reco	0.984 ± 0.013	0.992 ± 0.014	0.999 ± 0.014
CMIOCES	1.077 ± 0.016	1.073 ± 0.021	1.086 ± 0.014
CMIOPES	0.951 ± 0.015	1.011 ± 0.021	0.989 ± 0.014
CrkTrk μ	0.971 ± 0.013	0.952 ± 0.014	0.972 ± 0.013
TCE	0.964 ± 0.006	0.972 ± 0.007	0.981 ± 0.006
PHXTrk	0.995 ± 0.004	0.998 ± 0.005	1.024 ± 0.004
PHXPEM	0.938 ± 0.005	0.934 ± 0.006	0.943 ± 0.005
CrkTrk e	0.953 ± 0.017	0.931 ± 0.018	0.958 ± 0.015

Table 4.12: Lepton ID scale factors with and without track isolation cuts for data periods 11-17. No track isolation cut is applied to the PHX category.

Chapter 5

Dilepton Data Sample

This chapter describes the selection of dilepton events which are subsequently used in the search for $H \to WW \to \ell\nu\ell\nu$. Dilepton events are selected with the requirement of large missing transverse energy which is expected for Higgs signal events. In this chapter the signal region event selection is discussed as well as different event selection which define control regions that test different aspects of the data modeling in simulated events.

5.1 Trigger Requirements

Events considered in this analysis must first pass one of four specific trigger paths. The CDF trigger system is described in section 3.2.6. The four trigger paths used in this analysis are ELECTRON_CENTRAL_18, MUON_CMUP18, MUON_CMX18, and MET_PEM. The first three are specifically designed to trigger on high-P_T electrons and muons using a minimal set of identification cuts. The MET_PEM trigger is designed to trigger on events with a high-energy electromagnetic object in the forward calorimeter region, such as an electron or photon, and $\not\!\!E_T$. The specific trigger requirements are given in the following sub-sections. The overall efficiencies

for the different trigger paths and run periods are given in table 5.1.

5.1.1 CENTRAL_ELECTRON_18

The ELECTRON_CENTRAL_18 trigger path is designed to accept events which contain a high-P_T electron which enters the central calorimeter. This trigger path consists of the following level 1, 2, and 3 triggers:

- L1_CEM8_PT8 requires a central EM cluster with a measured E_T of at least 8 GeV, the ratio E_{Had}/E_{EM} to be less than 0.125, and an XFT track with $P_T > 8.34$ GeV.

- L2_CEM16_PT8 additionally requires an EM cluster with an E_T of at least 16 GeV which is in the range $|\eta_{det}| < 1.317$.

- L3_ELECTRON_CENTRAL_18 requires an L_{shr} less than 0.4, the Δz between the COT track extrapolation and the CES shower location measurement to be less than 8 cm, $E_T > 18$ GeV, and a COT track with $P_T > 9$ GeV. For these level-3 calculations the track z-vertex is used as well as a 3-tower EM cluster.

5.1.2 MUON_CMUP18

This trigger path is designed to accept events that contain a high-P_T muon where a high-momentum track points to hits in both the CMU and CMP detectors. The MUON_CMUP18 trigger consists of the following level 1, 2, and 3 triggers:

- L1_CMUP6_PT4 requires an XFT track with $P_T > 4.09$ GeV which is fiducial to the CMP and a CMP stub with a track having $P_T > 6$ GeV.
- L2_CMUP6_PT8 additionally requires a 4-layer XFT track with $P_T > 8.34$ GeV which is fiducial to both the CMU and CMP detectors.
- L3_MUON_CMUP_18 requires a COT track with $P_T > 18$ GeV whose extrapolation matches hits in the CMU and CMP detectors within a $\Delta x_{CMP} < 20$ cm and $\Delta x_{CMU} < 10$ cm.

5.1.3 MUON_CMX18

This trigger path is designed to accept events that contain a high-P_T muon where a high-momentum track points to hits in the CMX detector. The MUON_CMX18 trigger consists of the following level 1, 2, and 3 triggers:

- L1_CMX6_PT8_CSX requires a stub in the CMX with $P_T > 6$ GeV, an XFT track with $P_T > 8.34$ GeV, and a hit in the CSX.
- L2_CMX6_PT10 additionally requires a 4-layer XFT track with $P_T > 10.1$ GeV.
- L3_MUON_CMX18 requires a COT track with $P_T > 18$ GeV with a stub in the CMX matched to within $\Delta x_{CMX} < 10$ cm.

5.1.4 MET_PEM

The missing transverse energy calculation used in the online trigger system is the vector sum of raw transverse energy over all calorimeter towers, $\not\!\!E_T^{raw}$, which does not

include any energy corrections such as the corrections for muons and jets described in section 4.3. The MET_PEM trigger consists of the following level 1, 2, and 3 triggers:

- L1_EM8_&_MET15 requires at least a central or plug calorimeter cluster with $E_T > 8$ GeV, $E_{Had}/E_{EM} < 0.125$, $\not\!\!E_T^{raw} > 15$ GeV, and a minimum central and plug calorimeter $\sum E_T$ of 1 GeV.
- L2_PEM20_L1_EM8_&_MET15 additionally requires a plug calorimeter object with $E_T > 20$ GeV and $1.1 < \eta_{det} < 3.6$.
- L3_PEM20_MET15 additionally requires a plug calorimeter cluster using 3 towers with $E_T > 20$ GeV and $E_{Had}/E_{EM} < 0.125$.

5.2 Trigger Efficiencies

Trigger efficiencies are typically measured using an independent trigger path that contains an object of interest which, in principle, *should* have passed the trigger in question. The details on the methods used at CDF can be found elsewhere [40, 41, 43, 51]. Results of these measurements are briefly summarized here.

Trigger efficiencies are measured as a function of run number. The total average trigger path efficiencies are given in table 5.1. Additionally, E_T and η dependent corrections to the level-2 and level-3 electron trigger are applied which are of the form [11, 44]

$$\epsilon_{L2} = A + C\exp(-\sigma \cdot E_T) \qquad \epsilon_{L3} = A - C\exp[\sigma \cdot (E_T - E_0)] \tag{5.1}$$

	Efficiency			
Run Number	CENTRAL_ELECTRON	CMUP18	CMX18	MET_PEM
< 186598	0.9620	0.8977	0.9665	0.910
≥ 186598	0.9766	0.9180	0.9493	0.910
≥ 211312	0.9600	0.9180	0.9493	0.910
≥ 246231	0.9620	0.9180	0.9493	0.910

Table 5.1: Efficiencies for the level-3 trigger paths used in this analysis. Roughly, these are the probabilities that a lepton of sufficient energy and fiducial to the appropriate detector element, passes the trigger requirement.

$$\epsilon_\eta = A - \frac{C}{2\pi\sigma} \cdot \exp\left(-\frac{\eta^2}{2\sigma^2}\right) \tag{5.2}$$

where C, A, and σ are determined from a fit to the efficiency curve as a function of E_T (equation 5.1) or η (equation 5.2).

5.3 Good Run and Luminosity Accounting

This analysis uses up to 3.0 fb^{-1} of data collected by the CDF II detector between February 4, 2002 and April 16, 2008. Different portions of the detector may be operational or in-operational at different times. Lists are kept of which data taking runs have particular components both on and reliably working. This analysis uses several of these lists depending on the lepton types being identified. The luminosity totals for the different good run lists are given in table 5.2. The uncertainty on the luminosity measured from the CLC is estimated to be 5.9% [54].

The data is further divided into *periods* which will be referred to throughout this thesis. The periods along with the run numbers they span and corresponding luminosity are given in table 5.3.

Good run list	$\int \mathcal{L}dt$ (pb^{-1})
EM_NOSI	2960.5
EM_CMUP_NOSI	2922.9
EM_MU_NOSI_CMXIGNORED	2829.5
EM_SI	2820.5
EM_CMUP_SI	2785.4
EM_MU_SI_CMXIGNORED	2695.4

Table 5.2: Luminosity corresponding to the different good run lists (v23) used in this analysis.

Run Period	Run Number Range	Luminosity (pb^{-1})
0	138425 – 186598	550
1	190697 – 195408	130
2	195409 – 198379	130
3	198380 – 201349	100
4	201350 – 203799	95
5	203819 – 206989	135
6	206990 – 210011	110
7	210012 – 212133	50
8	217990 – 222426	210
9	222529 – 228596	180
10	228664 – 233111	280
11	233133 – 237795	264
12	237845 – 241664	185
13	241665 – 246231	317
14	252836 – 254683	45
15	254800 – 256824	159
16	256840 – 258787	142
17	258880 – 261005	188

Table 5.3: Run periods given with the run number that define them and the luminosity they correspond to.

Process	Period	Cross section (pb)	Generator
$W\gamma$	0-11	13.6	BAUR
WW	0-7	12.4	MC@NLO
WZ	0-17	3.65	PYTHIA
ZZ	0-17	1.511	PYTHIA
$Z/\gamma^* \rightarrow ee$	0-17	355×1.4	PYTHIA
$Z/\gamma^* \rightarrow \mu\mu$	0-17	355×1.4	PYTHIA
$Z/\gamma^* \rightarrow \tau\tau(M_{\ell\ell} > 10)$	0-11	1272×1.4	PYTHIA
$W +$ jets	0-17	-	Data

Table 5.4: A list of the background processes and generators used along with the cross sections and data periods modeled.

5.4 Monte Carlo Samples

Standard model backgrounds are modeled using simulated events from several Monte Carlo generators which are then passed through the full GEANT-4 [31] based CDF II detector simulation. The backgrounds considered in this analysis are given in table 5.4 along with the generator used, cross section, and run-dependent periods which are modeled by that particular sample. The exception among the SM backgrounds is the W+jets background which is obtained from the data. For a discussion of the W+jets background estimation see section 4.4.1.

The signal Monte Carlo is all generated using PYTHIA [61] as are several of the background process. The $W\gamma$ backgrounds are generated using BAUR [8]. The WW background, which is the most important background in this analysis is simulated using the next-to-leading-order (NLO) Monte Carlo generator MC@NLO [35].

The Monte Carlo is run dependent, meaning that the detector simulation is modeled in a time-dependent fashion which accounts for changes in the detector and differing instantaneous luminosity profiles over years of data taking. Different

samples have been generated using different run periods for previous analyses. The differences in lepton efficiencies in the run periods spanned by the different samples are accounted for and a systematic uncertainty assigned when necessary. It is particularly important to note that the WW sample was generated for periods 0-7 and is used to model periods 0-17. To account for differences in the run dependent modeling and luminosity profiles this sample is scaled according to the acceptance difference in a similar PYTHIA based WW sample between periods 0-7 and 0-17. The scaling is such that the scaled acceptance for the MC@NLO sample, $A_{MC@NLO}$, is given by

$$A_{MC@NLO} = A^{(0-7)}_{MC@NLO} \cdot \frac{A^{(0-17)}_{PYTHIA}}{A^{(0-7)}_{PYTHIA}} \tag{5.3}$$

where the superscript refers to the range of periods for which the detector was simulated for each sample. One can also think of this as scaling $w/\mathcal{L}$ where w is given in equation 5.4. Half of this acceptance difference is taken as a systematic uncertainty. The scaling and uncertainties are assigned according to jet multiplicity. For 0-jet events the scale applied to MC@NLO events is 0.923 and for 1-jet events is 0.964. The difference is very small for ≥ 2 jets so no scaling is applied, however a 1% error is assigned as a systematic in this channel to cover any difference.

Periods up to period 7 correspond to an integrated luminosity of 1.1 fb^{-1}, up to period 11 an integrated luminosity of 1.9 fb^{-1}, and up to period 17 corresponds to the entire dataset used in this analysis (3.0 fb^{-1}).

5.4.1 Weighting Monte Carlo Events

Many more events are simulated for a process than is expected in data, which is to say that the effective integrated luminosity of the Monte Carlo samples is generally much larger than the integrated luminosity of the data. Each Monte Carlo event is given a weight which accounts for this difference as well as for lepton identification, trigger, vertex, and filter efficiencies. Note that if the Monte Carlo and data efficiencies were exactly the same this weight would be equal to the ratio of the luminosities $\int \mathcal{L}_{\mathrm{Data}} dt / \int \mathcal{L}_{\mathrm{MC}} dt$.

The weight for each Monte Carlo event is given by

$$w = \frac{\sigma \cdot \mathcal{B} \cdot \epsilon_{\mathrm{filter}} \cdot \epsilon_{\mathrm{trig}} \cdot s_{\mathrm{lep}} \cdot \epsilon_{\mathrm{vtx}} \cdot \mathcal{L}}{N_{\mathrm{gen}}} \tag{5.4}$$

where

- σ is the cross section for the process considered.
- $\mathcal{B}$ is the branching fraction for the process considered.
- $\epsilon_{\mathrm{filter}}$ is the filter efficiency of any Monte Carlo event generation filters applied.
- ϵ_{trig} is an effective trigger efficiency determined from the probability that each lepton activated one of the triggers used in data.
- s_{lep} is a lepton ID scale factor based on the difference in efficiencies in data and simulation.
- ϵ_{vtx} is the efficiency of the z-vertex cut $|z_{\mathrm{vtx}}| < 60$ cm which is $0.9555 \pm 0.0004(stat) \pm 0.0031(syst)$ [60].

- $\mathcal{L}$ is the luminosity corresponding to the dilepton type.
- N_{gen} is the number of Monte Carlo events generated whose primary vertex is within the range $|z_0| < 60$ cm.

This weight is calculated for each event in the Monte Carlo. The absolute yield for a process given any event selection criterion will then be the sum of the weights for events which pass that criterion. The yield for W+jets is calculated somewhat differently since it is estimated directly from the data. This is explained further in section 4.4.1.

5.5 High Level Cuts

The event selection criteria described in this section apply specifically to the signal region, sometimes referred to as the base signal region. This analysis does not cut hard on any particular quantity, or even on very many variables. The underlying idea in this analysis is to keep as much signal as reasonably possible to increase the overall acceptance. Although the signal to background ratio as seen from a counting experiment perspective may be poor, there is an overall benefit in keeping more events and employing more sophisticated discriminating techniques (discussed in chapters 6 and 9) which will distinguish between signal and background.

5.5.1 $\not\!\!E_T^{spec}$: The Missing Transverse Energy Requirement

When selecting events with 2 high-P_T leptons from the CDF dataset by far the most predominant background is due to Drell-Yan production of $\ell^+\ell^-$ pairs. The $\not\!\!E_T^{spec}$

("$\not\!\!E_T$ special") cut is designed to cut out more than 99.9% of these events which have no real $\not\!\!E_T$ due to no neutrinos in the final state. The $\not\!\!E_T^{spec}$ variable is defined as

$$\not\!\!E_T^{spec} = \begin{cases} \not\!\!E_T & \text{if} \quad \Delta\phi(\vec{\not\!\!E}_T, \text{nearest } \ell \text{ or } j) > \pi/2 \\ \not\!\!E_T \sin[\Delta\phi(\vec{\not\!\!E}_T, \text{nearest } \ell \text{ or } j)] & \text{if} \quad \Delta\phi(\vec{\not\!\!E}_T, \text{nearest } \ell \text{ or } j) < \pi/2 \end{cases}.$$

If the $\vec{\not\!\!E}_T$ is close to a lepton or jet there is a significant probability that the $\not\!\!E_T$ is not coming from real physics, but rather coming from the mis-measurement of a lepton or jet. Any $\not\!\!E_T$ from Drell-Yan events must come from such mis-measurements. The $\not\!\!E_T^{spec}$ cut drastically reduces the number of Drell-Yan background while keeping 86% of the $gg \to H$ signal at $M_H = 160$ GeV. The cut on $\not\!\!E_T^{spec}$ depends on the dilepton type and for events to be considered in this analysis they must satisfy

$$\begin{array}{ll} \not\!\!E_T^{spec} > 25 \text{ GeV} & \text{for } ee \text{ and } \mu\mu \text{ events} \\ \not\!\!E_T^{spec} > 15 \text{ GeV} & \text{for } e\mu \text{ events} \end{array}.$$

For the purposes of this $\not\!\!E_T^{spec}$ cut dilepton categories containing a CrkTrk lepton are considered as ee and $\mu\mu$ events such that they must satisfy the high $\not\!\!E_T^{spec}$ requirement. The distribution of $\not\!\!E_T^{spec}$ before the $\not\!\!E_T^{spec}$ cut has been made is shown in figure 5.1.

5.5.2 Cosmic Rejection

High-P_T muons created from cosmic ray events originating in the upper atmosphere often traverse the CDF detector. These events, while interesting in their own right,

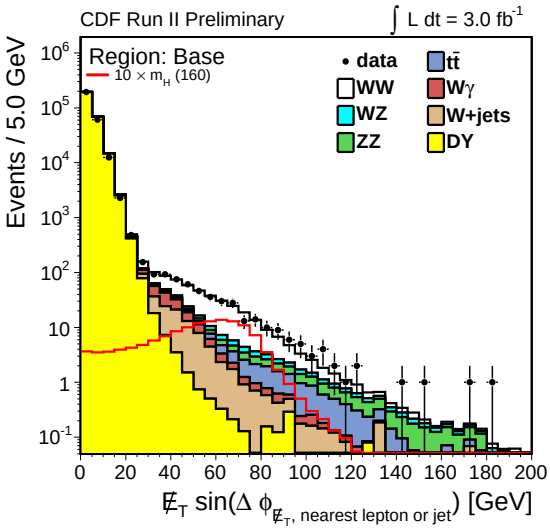

Figure 5.1: $\not\!\!E_T^{spec}$ distributions before any $\not\!\!E_T^{spec}$ selection cut has been made.

do not originate from the $p\bar{p}$ collisions and therefore must be removed from the data sample. They are typically high-momentum muons which do not necessarily pass through the center of the detector. These events are tagged and removed from the data sample using previously developed cosmic-ray identification methods [62, 63].

5.5.3 Conversion Veto

Electrons traversing the detector can emit photons due to bremsstrahlung radiation from the interaction with detector material. These photons can then convert to electron-positron pairs which are characterized by two tracks with a small opening angle and a vertex far from the primary interaction point. Events which contain such a conversion are identified and removed from the data sample. The algorithms for removal are described in [6, 42].

Dilepton Flavor	Dilepton Category
ee	TCE – TCE
ee	TCE – PHX
ee	PHX – PHX
$\mu\mu$	CMUP – CMUP
$\mu\mu$	CMUP – CMX
$\mu\mu$	CMX – CMX
$\mu\mu$	CMUP – CMIOCES
$\mu\mu$	CMUP – CMIOPES
$\mu\mu$	CMX – CMIOCES
$\mu\mu$	CMX – CMIOPES
$e\mu$	TCE – CMUP
$e\mu$	TCE – CMX
$e\mu$	TCE – CMIOCES
$e\mu$	TCE – CMIOPES
$e\mu$	PHX – CMUP
$e\mu$	PHX – CMX
$e\mu$	PHX – CMIOCES
$e\mu$	PHX – CMIOPES
e Trk	TCE – CrkTrk
e Trk	PHX – CrkTrk
μ Trk	CMUP – CrkTrk
μ Trk	CMX – CrkTrk

Table 5.5: Dilepton categories used in this analysis.

5.5.4 Dilepton Requirements

This analysis requires that there are two high energy leptons of opposite sign. The leading lepton P_T (or E_T for electrons) must be greater than 20 GeV to satisfy the trigger requirements given in section 5.1. The sub-leading lepton may have a P_T (E_T) as low as 10 GeV. The dilepton categories considered in this analysis are listed in table 5.5.

5.6 Control Regions

As a check that the data is being well modeled by the simulation it is desirable to have selection regions which are independent of the signal sample region. Examining carefully chosen sub-samples of the data will establish that the simulation is appropriately modeling the data in various aspects discussed in the following sections as well as give one confidence that the signal region is also being well modeled.

Several distinct selection criteria (regions) are discussed below. Two checks that are done in addition to examining these control regions are measuring the WW and $t\bar{t}$ cross sections. These measurements are discussed in chapter 7 and section 5.6.5 respectively.

5.6.1 Drell-Yan Control Region

The Drell-Yan ($Z/\gamma^* \rightarrow e^+e^-$ / $\mu^+\mu^-$ / $\tau^+\tau^-$) control region is designed to test the accuracy of luminosity accounting, the measurement of trigger efficiencies, and the corrections on lepton efficiencies (scale factors) applied to the Monte Carlo in an attempt to match the data. This is a very high statistics sample due to the very large Drell-Yan cross section. It should be noted that the Drell-Yan sample is very similar to the sample used to actually measure the lepton efficiencies discussed in section 4.5. One may notice small modeling difficulties in figure 5.3 especially in events where the leptons have a large opening angle between them. This discrepancy is a result of imperfect QCD radiation modeling in the Monte Carlo and is more pronounced in samples containing no real $\not\!\!E_T$. The majority of these events do not pass the signal selection criteria and are not a concern in this analysis.

Category	WW	WZ	ZZ	$t\bar{t}$	DY	$W\gamma$	W+jets	Total	Data
$e\ e$	6.6	38.3	33.8	1.3	104622.3	1.9	517.1	105221.1	102213.0
$e\ \mu$	6.3	0.1	0.1	1.1	82.9	0.4	31.2	122.2	99.0
$\mu\ \mu$	6.1	31.3	29.4	1.4	82223.1	0.0	369.7	82661.1	80382.0
e trk	5.9	12.4	11.3	1.2	32387.7	0.7	533.4	32952.6	30240.0
μ trk	3.8	10.8	10.0	0.8	27673.3	0.0	312.0	28010.7	26750.0
Total	28.7	92.9	84.6	5.9	246989.3	3.0	1758.8	248963.0	239684.0

Table 5.6: Yields in the Drell-Yan control region for 3.0 fb^{-1}.

Events in this region must satisfy the following criterion:

- Dilepton invariant mass consistent with the Z mass: $76 < M_{\ell\ell} < 106$ GeV
- Lepton charges of opposite sign: $\ell^+\ell^-$
- Low missing transverse energy: $\not\!\!E_T < 25$ GeV

The predicted yields from the different dilepton sources along with the number of observed events from data is shown in table 5.6. Note that the contribution to the $e\mu$ channel for Drell-Yan will come predominantly from leptonic τ decays ($\tau \to e\bar{\nu}_e$ and $\tau \to \mu\bar{\nu}_\mu$) with a small portion coming from one of the leptons being faked, most of the time due to a muon track creating a large electromagnetic energy deposit from bremsstrahlung. Several distributions for various variables used subsequently in the analysis are shown in figures 5.2 and 5.3. In general, there is good agreement between the predicted and observed rates and kinematic shapes.

5.6.2 Base Low $\not\!\!E_T^{sig}$ Control Region

This region is the same as the base selection region with the extra requirement of low $\not\!\!E_T^{sig}$applied where

$$\not\!\!E_T^{sig} = \not\!\!E_T / \sqrt{\sum E_T}. \tag{5.5}$$

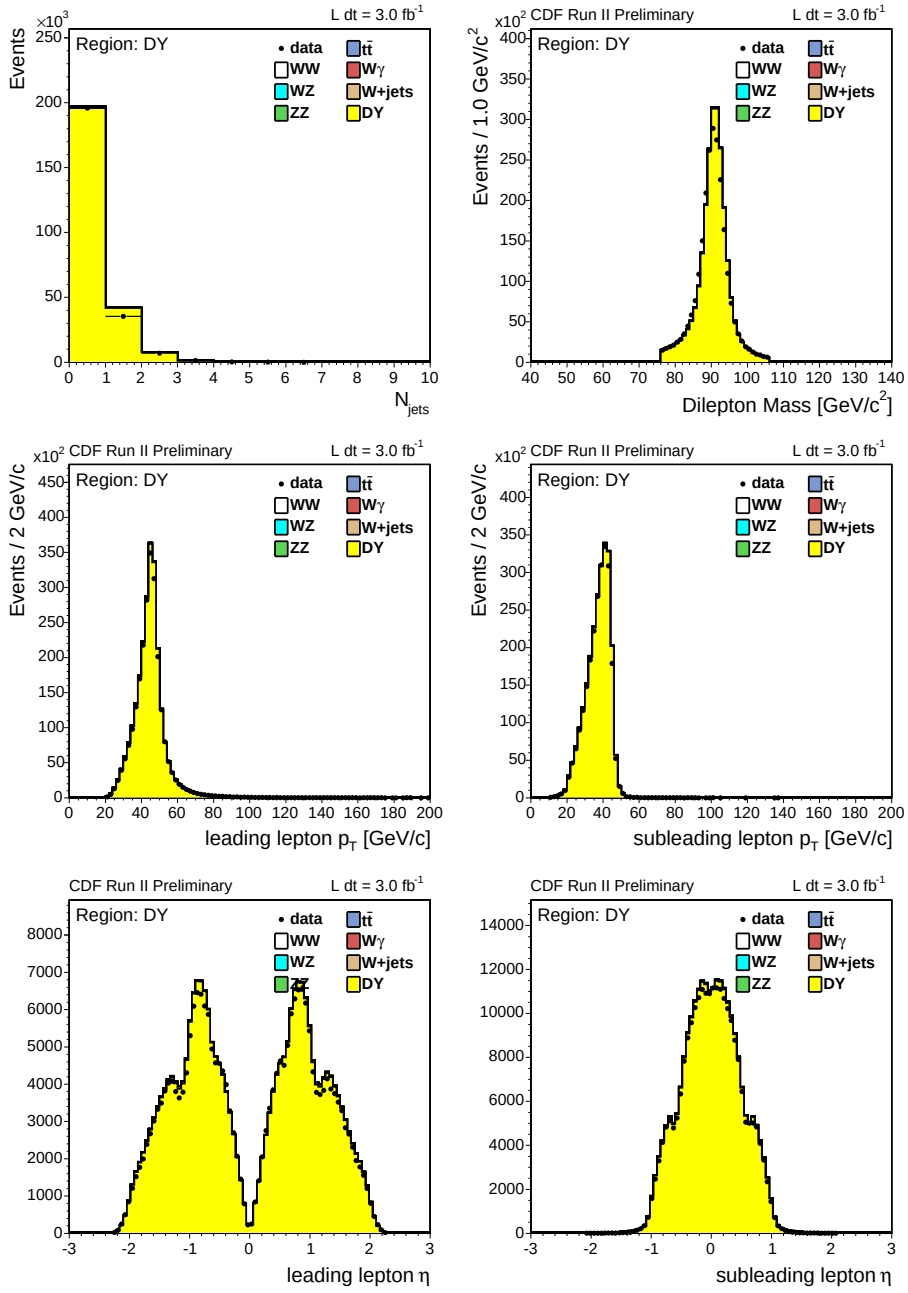

Figure 5.2: Drell-Yan control region showing N_{jets}, $M_{\ell\ell}$, lepton momenta, and lepton η distributions.

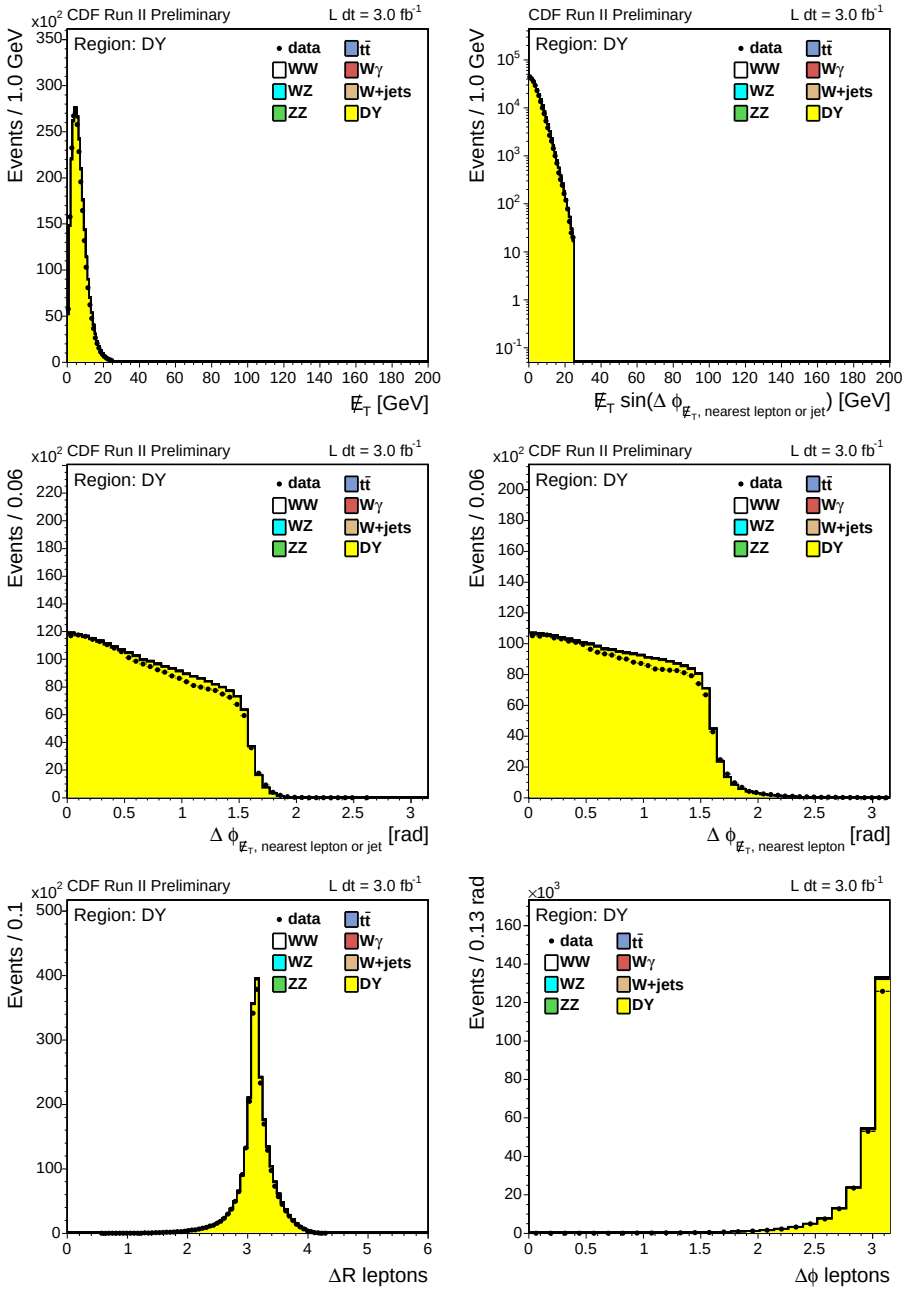

Figure 5.3: Drell-Yan control region showing $\not\!\!E_T$ related variables as well as lepton separation distributions.

Category	WW	WZ	ZZ	$t\bar{t}$	DY	$W\gamma$	W+jets	Total	Data
$e\ e$	4.1	0.9	0.7	0.3	33.2	3.7	6.0	49.0	44.0
$e\ \mu$	0.0	0.0	0.0	0.0	0.0	0.0	0.0	0.0	0.0
$\mu\ \mu$	3.3	0.7	0.6	0.3	21.4	0.0	1.2	27.5	34.0
e trk	3.5	0.5	0.3	0.3	13.0	0.9	2.1	20.7	23.0
μ trk	2.0	0.3	0.2	0.2	6.9	0.1	1.0	10.7	6.0
Total	13.0	2.3	1.8	1.2	74.5	4.8	10.3	107.8	107.0

Table 5.7: Yields in the base low $\not\!\!E_T^{sig}$ control region for 3.0 fb^{-1}.

This quantity is particularly useful in distinguishing events which have large $\not\!\!E_T$ relative to the total measured energy of the other objects in the event. Specifically the $\not\!\!E_T^{sig}$ is required to be less than 2.5 GeV$^{1/2}$. This region serves as a cross check of the $\not\!\!E_T$ simulation. It largely consists of Drell-Yan and is used to assess the $\not\!\!E_T$ uncertainty on the Drell-Yan in the signal region. This region tests the mis-measurement of multiple leptons and jets as well as mis-measured unclustered energy. The yields for data and simulation are given in table 5.7. Note that the rates are not particularly large because the base selection region requires large $\not\!\!E_T^{spec}$ which mostly translates to large $\not\!\!E_T^{sig}$ except for the relatively few cases where significant $\not\!\!E_T$ results from poorly measured leptons and jets. Various distributions for this region are shown in figures 5.4 and 5.5.

5.6.3 Low $\not\!\!E_T^{spec}$, High $\not\!\!E_T$ Control Region

This region is another test of the $\not\!\!E_T$ modeling correlated to the base low $\not\!\!E_T^{sig}$ control region but providing a slightly different test. Requiring low $\not\!\!E_T^{spec}$ and high $\not\!\!E_T$ implies that the $\not\!\!E_T$ is predominantly along the direction of a single lepton or jet. This region gives an indication of how well the mis-measurement of single objects

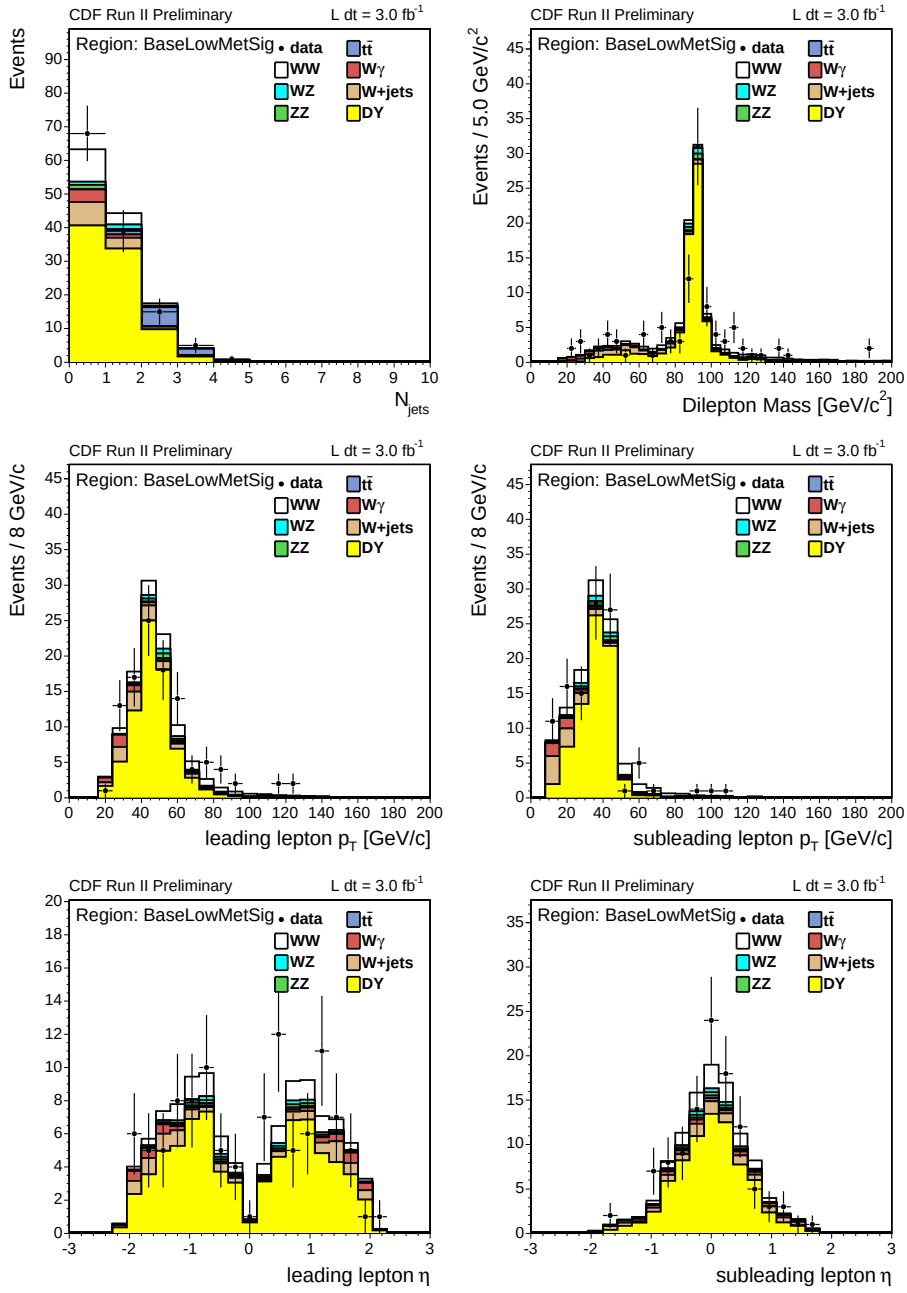

Figure 5.4: Base low $\not\!\!E_T^{sig}$ control region showing N_{jets}, $M_{\ell\ell}$, lepton momenta, and lepton η distributions.

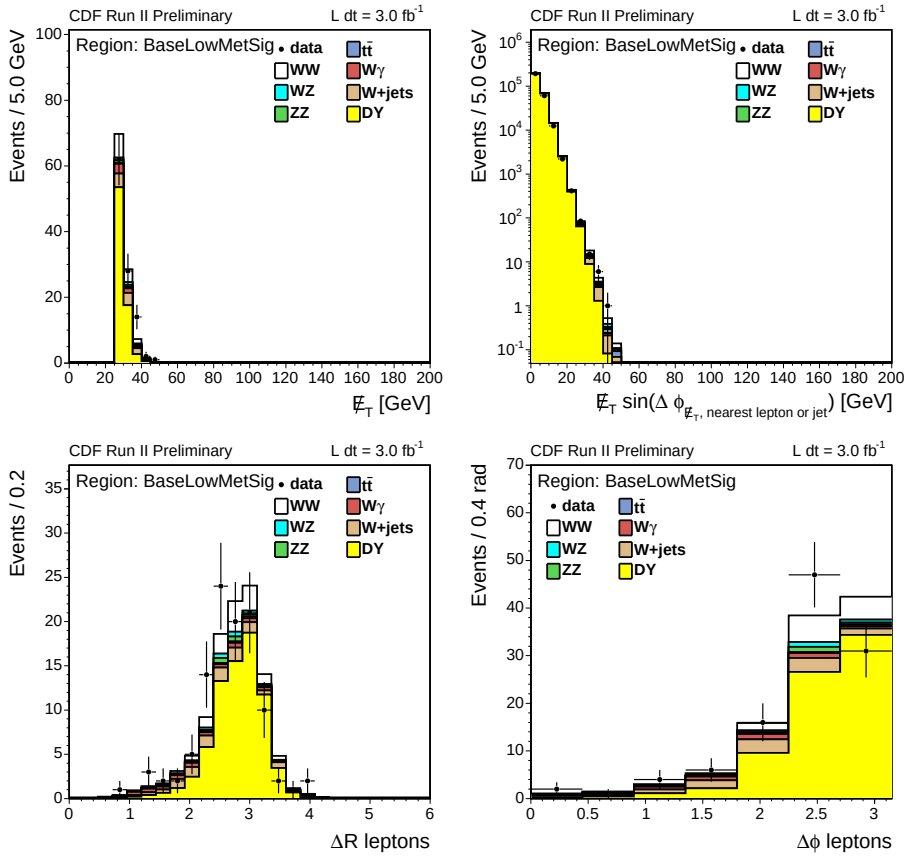

Figure 5.5: Base low $\not\!\!E_T^{sig}$ control region showing $\not\!\!E_T$ related variables as well as lepton separation distributions.

Category	WW	WZ	ZZ	$t\bar{t}$	DY	$W\gamma$	W+jets	Total	Data
e e	5.4	1.4	1.1	0.6	60.4	3.7	7.1	79.7	60.0
e μ	8.5	0.4	0.1	0.8	46.6	2.6	6.1	65.1	41.0
μ μ	4.0	1.0	0.9	0.6	48.8	0.0	2.1	57.3	73.0
e trk	4.3	0.7	0.5	0.5	59.4	0.8	4.8	71.0	58.0
μ trk	2.6	0.4	0.3	0.3	13.3	0.1	2.0	19.0	22.0
Total	24.9	3.8	2.9	2.8	228.5	7.2	21.7	291.8	254.0

Table 5.8: Yields in the low $\not\!\!E_T^{spec}$ high $\not\!\!E_T$ control region for 3.0 fb^{-1}.

is modeled. The yields for data and simulation are given in table 5.8. Various distributions for this region are shown in figures 5.6 and 5.7.

The requirements for this region are the same as the base region, however the $\not\!\!E_T$ and $\not\!\!E_T^{spec}$ are required to be

$$\begin{aligned} \not\!\!E_T &> 25 \text{ GeV} \\ \not\!\!E_T^{spec} &< 25 \text{ GeV}. \end{aligned}$$

5.6.4 Base Same Sign Control Region

The same sign region is very similar to the base signal region except that the opposite sign (charge) lepton requirement is reversed and a same sign lepton pair is required. There are few SM processes which give a same sign lepton pair with significant $\not\!\!E_T$. These include small contributions from $t\bar{t}$ involving the semi-leptonic decay of a b-quark and WZ and ZZ where one lepton (or two in the case of ZZ) was not found. There will also be some contamination from opposite sign events where the charge of one lepton is misidentified. The probability for charge mis-identification

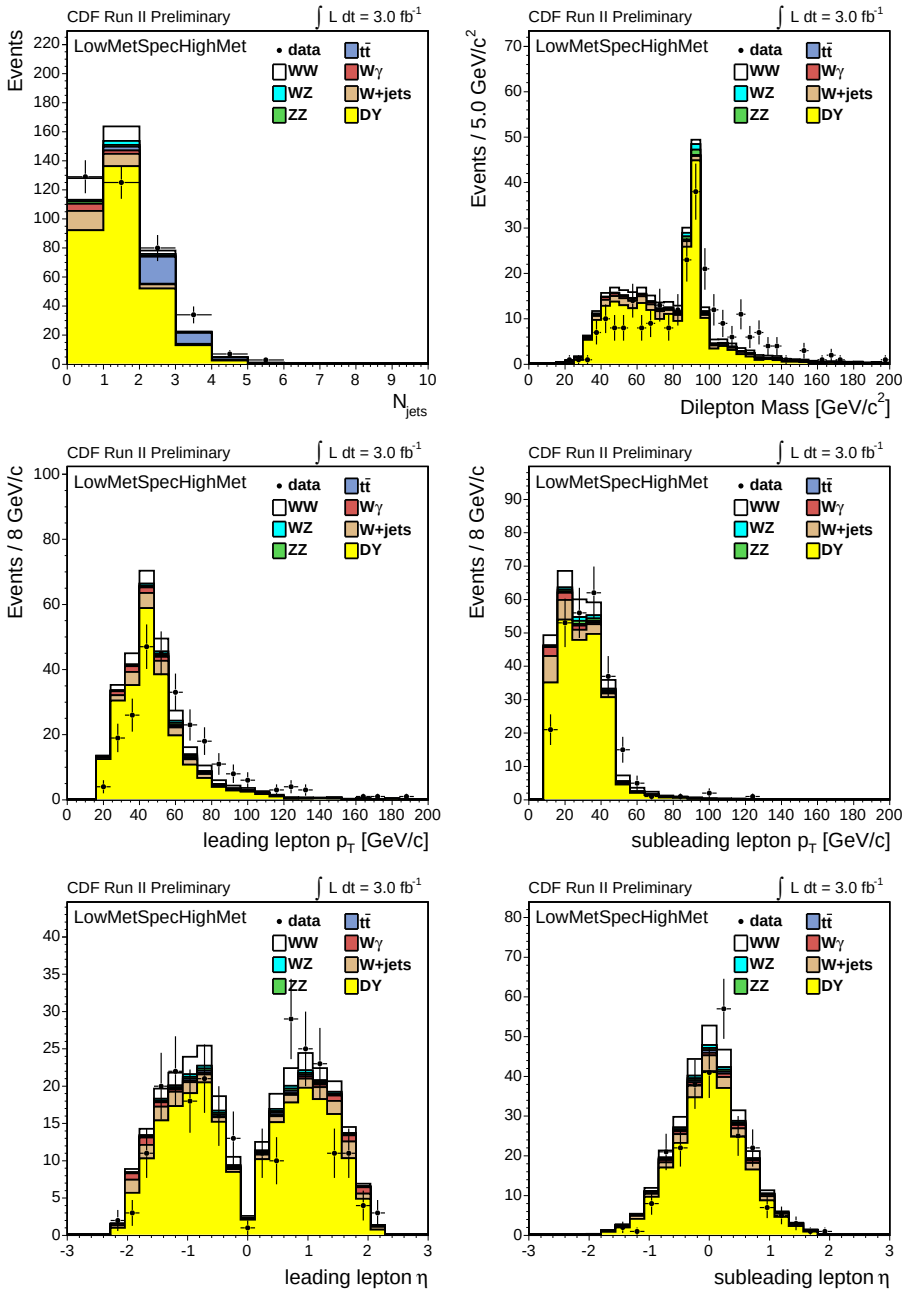

Figure 5.6: Low $\not\!\!E_T^{spec}$ high $\not\!\!E_T$ control region showing N_{jets}, $M_{\ell\ell}$, lepton momenta, and lepton η distributions.

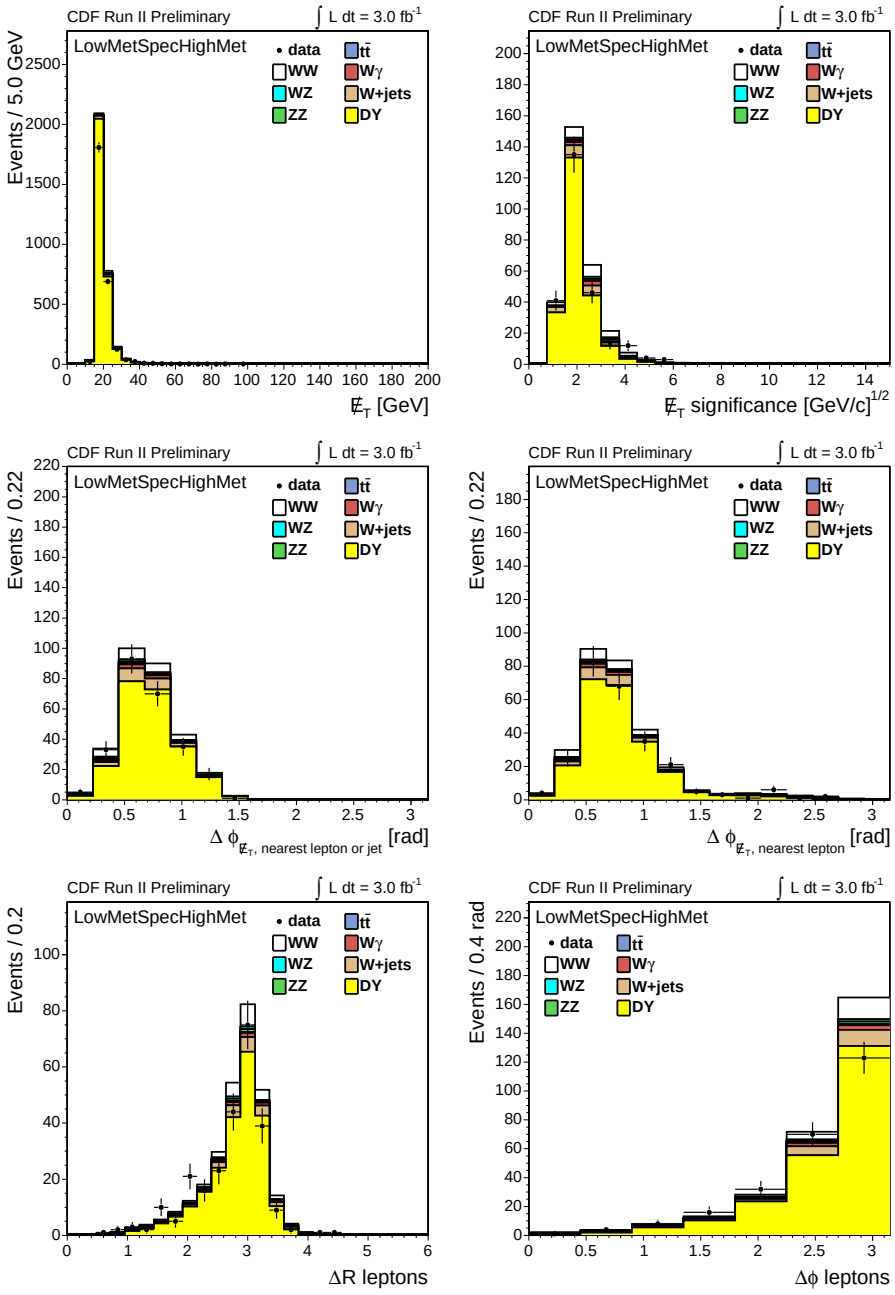

Figure 5.7: Low $\not\!\!E_T^{spec}$ high $\not\!\!E_T$ control region showing $\not\!\!E_T$ related variables as well as lepton separation distributions.

Category	WW	WZ	ZZ	$t\bar{t}$	DY	$W\gamma$	W+jets	Total	Data
$e\ e$	4.2	2.2	0.6	0.2	3.9	41.3	32.9	85.4	83.0
$e\ \mu$	5.0	4.6	0.4	0.3	9.4	39.0	36.6	95.1	99.0
$\mu\ \mu$	0.0	1.5	0.2	0.0	0.1	0.0	3.2	5.1	5.0
e trk	1.7	1.6	0.2	0.1	1.5	9.8	9.7	24.5	27.0
μ trk	0.0	0.9	0.1	0.0	0.3	1.7	4.6	7.6	7.0
Total	10.9	10.8	1.4	0.6	15.2	91.8	84.9	215.5	221.0

Table 5.9: Yields in the low $\not\!\!E_T^{spec}$ high $\not\!\!E_T$ control region for 3.0 fb^{-1}.

is higher for very forward tracks where the COT does not provide full coverage and the silicon tracking detector is more heavily relied upon.

The dominant contributions to this sample are from $W\gamma$ and W+jet events where the photon or jet is falsely reconstructed as a lepton. The fakes from $W\gamma$ are predominantly in the forward regions of the detector where the photon fakes an electron. Jet fake probabilities are discussed further in section 4.4. Checks in this region demonstrate that estimates of the fake probabilities and photon fake rates are well understood. The yields for data and simulation are given in table 5.9. Various distributions for this region are shown in figures 5.8 and 5.9.

5.6.5 Two Jet B-Tag $t\bar{t}$ Control Region

In the $\geq$ 2 jets analysis discussed in section 9.3 events which have a secondary vertex tag are vetoed to eliminate most of the $t\bar{t}$ contribution which is the dominant background in the $\geq$ 2 jet events. Events which have at least one secondary vertex are thus a natural choice for an independent control region. The selection criteria for this region are the same as the $\geq$ 2 jets signal region, but requires at least one secondary vertex tag, which further enhances the $t\bar{t}$ contribution. This control

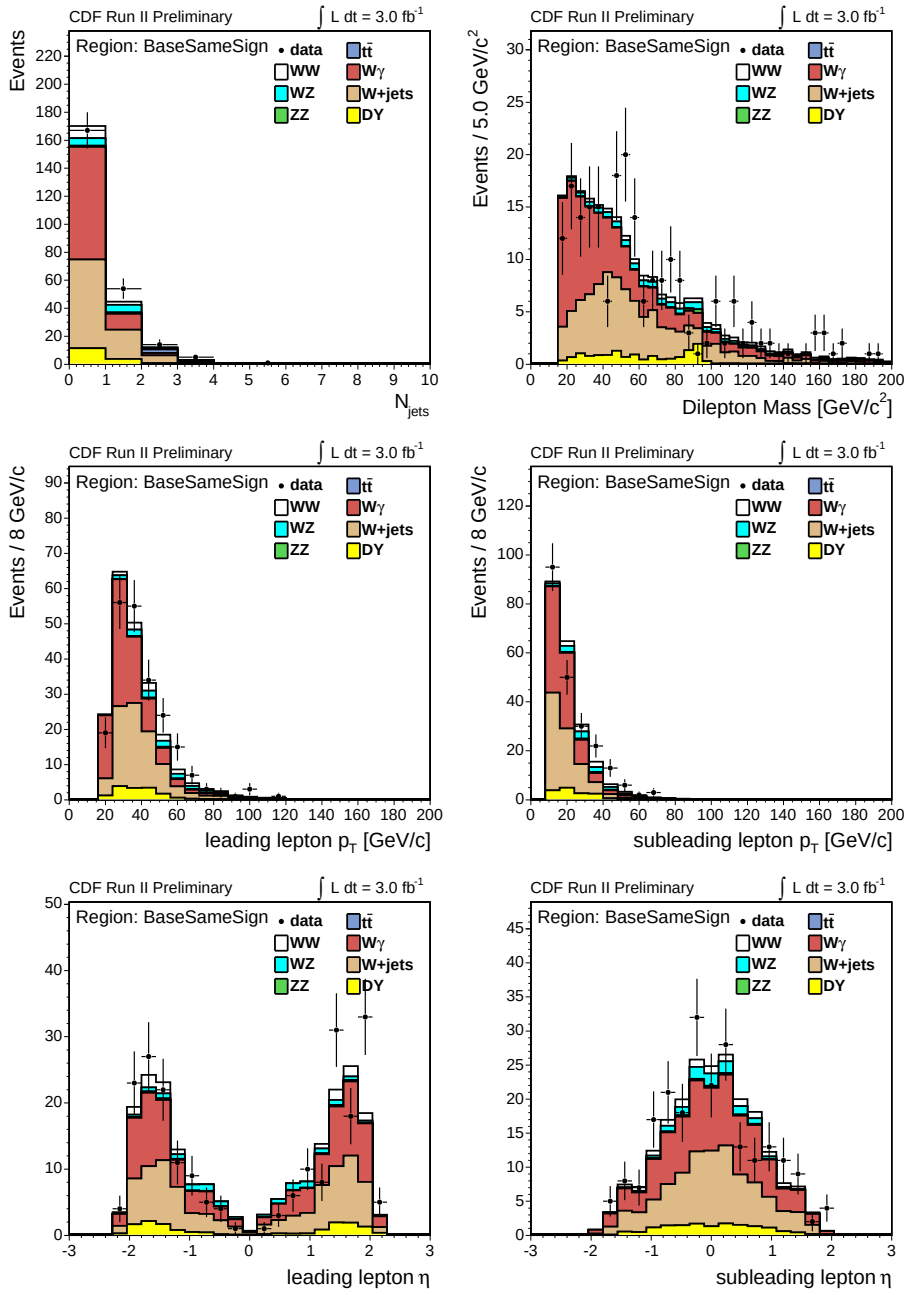

Figure 5.8: Same-sign control region showing N_{jets}, $M_{\ell\ell}$, lepton momenta, and lepton η distributions.

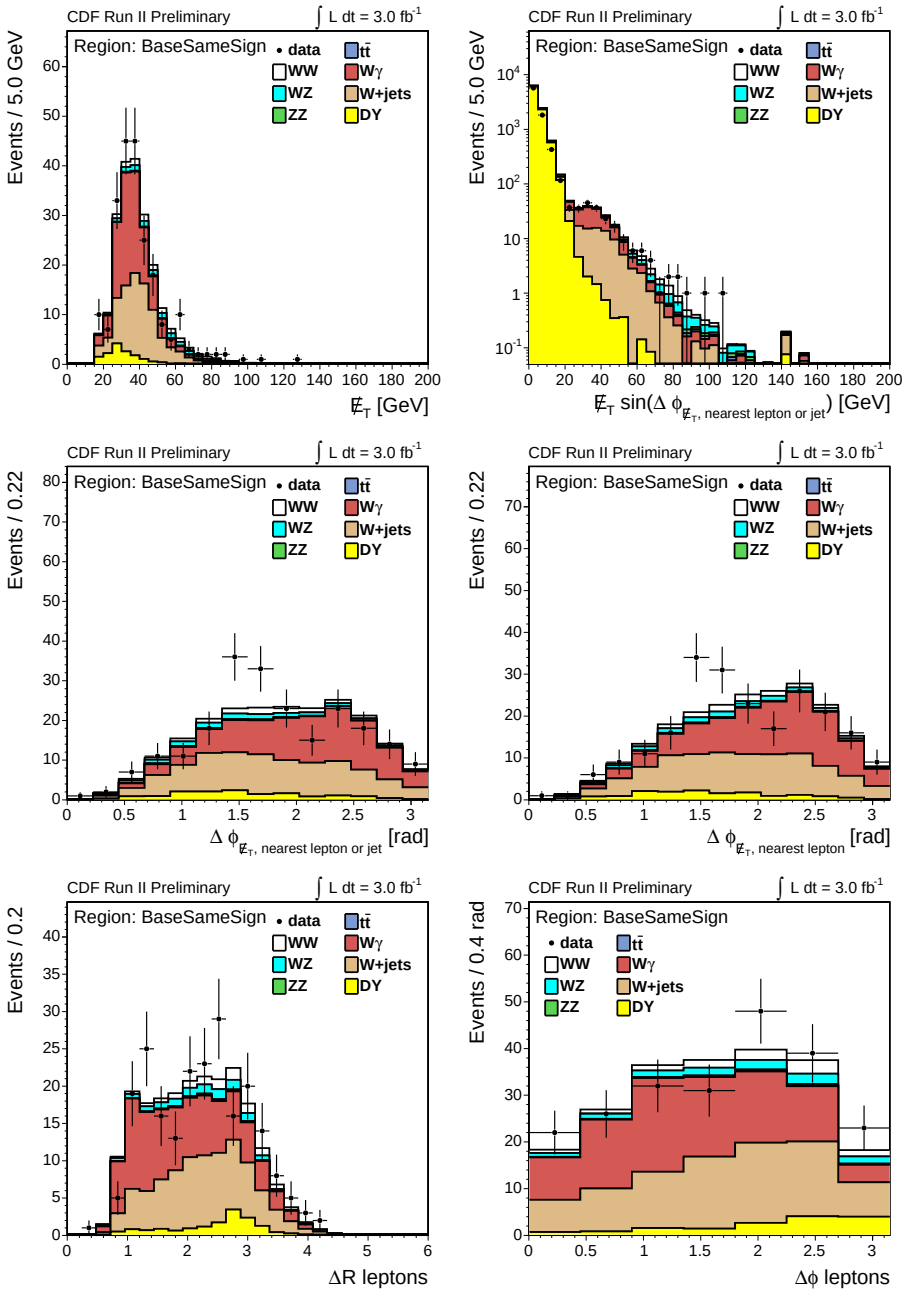

Figure 5.9: Same-sign control region showing $\not\!\!E_T$ related variables as well as lepton separation distributions.

region is dominated by $t\bar{t}$ events. The yields for this region are shown in table 5.10. Several kinematic distributions are shown in figures 5.10 and 5.11.

As well as verifying that the kinematics in this region are well modeled, the $t\bar{t}$ cross section can be measured. This is done by a simple counting experiment and background subtraction as given by

$$\sigma_{t\bar{t}}^{\text{measured}} = \frac{N_{\text{obs}} - N_{\text{BG}}}{A\mathcal{L}} \tag{5.6}$$

where N_{obs} is the number of events observed in data, N_{BG} is the number of predicted background events, A the $t\bar{t}$ acceptance, and $\mathcal{L}$ the luminosity. The $t\bar{t}$ cross section measurement from this control region is

$$\sigma_{t\bar{t}}^{\text{measured}} = 7.0 \pm 0.7(\text{pb}).$$

This measurement is consistent with the predicted SM cross section of $6.7^{+0.7}_{-0.9}$ pb (at $M_t = 175$) GeV [30] as well as other recent CDF measurements in the dilepton channel of $7.81 \pm 0.92 \pm 0.68 \pm 0.45$ pb [64] and $8.96 \pm 1.12 \pm 0.72 \pm 0.52$ pb [65].

$t\bar{t}$ Control Region	
DY	0.56 ± 0.12
WW	0.42 ± 0.05
W+jets	1.13 ± 0.29
$W\gamma$	0.07 ± 0.02
WZ	0.08 ± 0.01
ZZ	0.08 ± 0.01
Total background	**2.34 ± 0.32**
$t\bar{t}$	91.44 ± 16.92
Data	**98**

Table 5.10: Yields in the b-tag $t\bar{t}$ control region where $t\bar{t}$ is considered the signal in this sample.

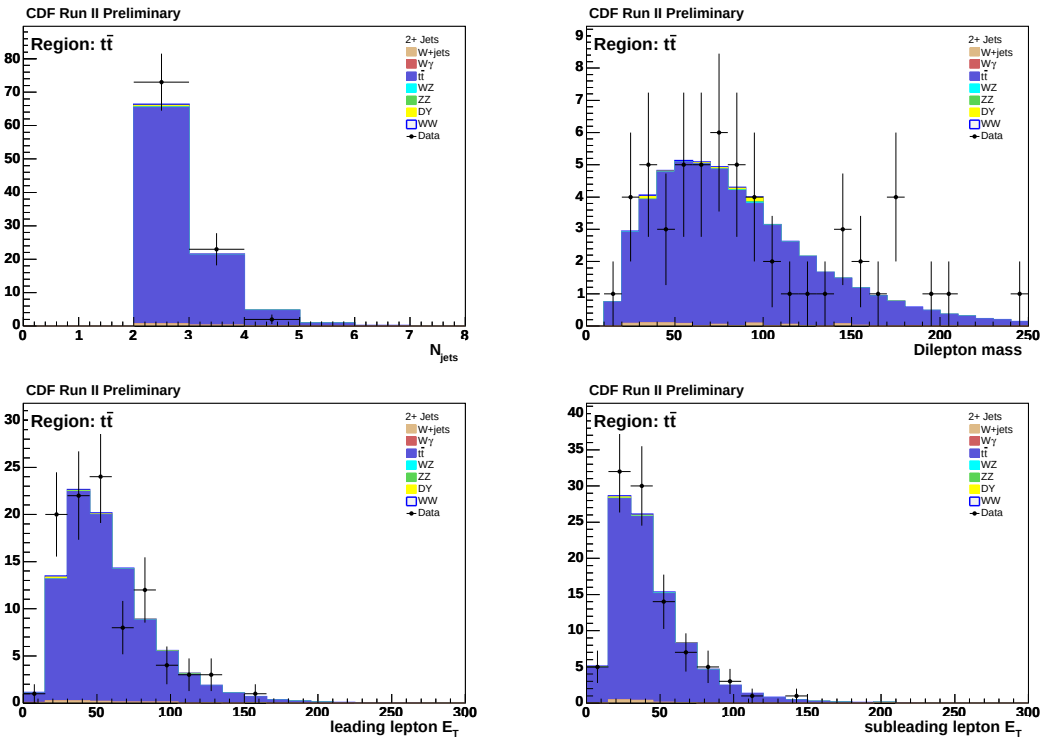

Figure 5.10: Distributions showing number of jets, dilepton invariant mass, and lepton E_T for the $t\bar{t}$ control region.

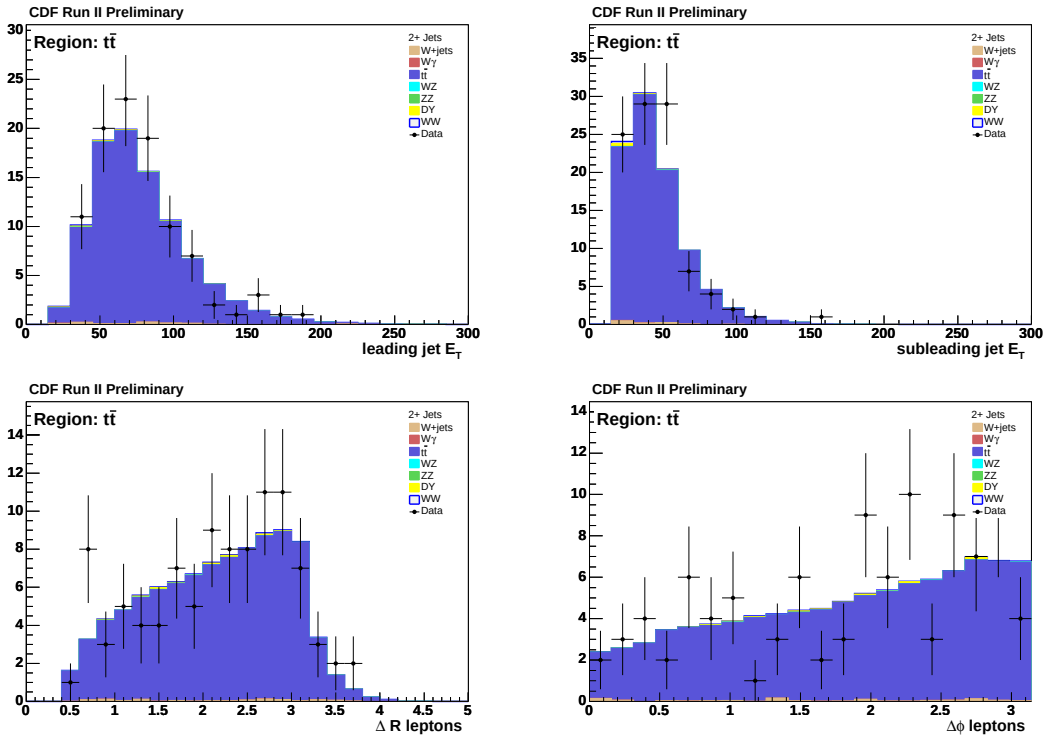

Figure 5.11: Distributions of the E_T for the 2 leading jets and lepton separation variables for the $t\bar{t}$ control region.

Chapter 6

Matrix Elements

One of the most powerful tools incorporated in this analysis is that of matrix element based event probabilities. The first inclusion of matrix element based probabilities in a $H \rightarrow WW$ search preceded this analysis and the tools previously developed [24] have been implemented in this analysis. Crudely, this assigns a probability that the kinematics of a given event are consistent with a given process based on matrix element calculations of that process. These event probabilities are calculated for five processes: WW, ZZ, $W\gamma$, W+jet, and $H \rightarrow WW$ (at each mass considered). The event probability for a process X is given by

$$P_X(\vec{x}_{obs}, \alpha) = \frac{1}{\langle \sigma_{LO}(\alpha) \rangle} \int \frac{d\sigma_{LO}(\vec{y}, \alpha)}{d\vec{y}} \, \epsilon(\vec{y}) \, G(\vec{x}_{obs}, \vec{y}) \, d\vec{y}. \tag{6.1}$$

This probability is a function of the observed momenta vectors of the leptons and $\not\!\!E_T$(denoted as $\vec{x}_{obs}$) as well as the Higgs mass and width (given by α). The true values of the observables are given by $\vec{y}$ which are unknown (or known only to the degree which they can be measured) but constrained by the measured quantities $\vec{x}_{obs}$, with transfer functions G representing the uncertainty in the measured quantities, and a detector acceptance and efficiency function ϵ. The differential cross

section $\frac{d\sigma_{LO}(\vec{y},\alpha)}{d\vec{y}}$ is integrated over all y and normalized by $1/\langle\sigma_{LO}(\alpha)\rangle$ such that

$$\int P(\vec{x}_{obs},\alpha)\, d\vec{x}_{obs} = 1.$$

Here, σ_{LO} is the leading order cross section as calculated by MCFM [14], which is also the matrix element calculator used in this analysis. The matrix elements will be denoted by $\mathcal{M}_X$ in the following sections.

The parton distribution functions (PDFs) used for these calculations are the CTEQ5l [55] set of functions and denoted by $f(x)$. Integration is performed by the FOAM [52] integration package. Each of the processes modeled are briefly discussed in the following sections.

6.1 Higgs - $H \rightarrow WW^*$

The $gg \rightarrow H \rightarrow WW^* \rightarrow \ell\nu\bar{\ell}\bar{\nu}$ mode is calculated at each of the 14 masses investigated (from 135 to 180 GeV in 5 GeV intervals). W^* indicates that one of the W bosons must be off-shell if $M_H < 2M_W$. The differential cross section is given by

$$\frac{d\sigma_H}{dx} = \frac{1}{16(2\pi)^8}\int \frac{f(x_1)f(x_2)|\mathcal{M}_H|^2}{16x_1x_2E_{Beam}^4}\frac{1}{|J|}\frac{dM_H dM_W d\nu_z d\bar{\nu}_z}{L_E^+ L_{\bar{E}}^- \nu_E \bar{\nu}_E} \tag{6.2}$$

where the Jacobian is given by

$$J = 4(W_E\frac{\nu_z}{\nu_E} - W_z)(H_E\frac{\bar{\nu}_z}{\bar{\nu}_E} - H_z).$$

The $L_E^{\pm}$ and ν_E are the lepton and neutrino energies respectively. ν_z and $\bar{\nu}_z$ are the neutrino z-momentum components. E_{Beam} is the energy in each beam, which is 980 GeV at the Tevatron. The $x_{1,2}$ refer to the momentum fraction of the initial interacting partons, H_E and H_z are the energy and z-component of momentum of the Higgs and are defined similarly for W. There are 16 total degrees of freedom, 6 of which are constrained by the outgoing lepton momenta, 4 constraints come in the form of energy-momentum conservation relationships, and two additional constraints come from $(\vec{\not{E}}_T)_x$ and $(\vec{\not{E}}_T)_y$. This leaves 4 degrees of freedom which must be integrated over.

6.2 WW

$p\bar{p} \to WW \to \ell\nu\bar{\ell}\bar{\nu}$ is the largest and most difficult background. In this case, like the signal, there are 4 remaining unconstrained parameters which are integrated over. The differential cross section for WW production can be written as

$$\frac{d\sigma_{WW}}{dx} = \frac{1}{16(2\pi)^8} \int \frac{f(x_1)f(x_2)|\mathcal{M}_{WW}|^2}{16x_1x_2E_{Beam}^4} \frac{1}{|J|} \frac{dM_{W_1}dM_{W_2}d\nu_x d\nu_y}{L_E^+ L_E^- \nu_E \bar{\nu}_E} \tag{6.3}$$

where the Jacobian is given by

$$J = 4(L_E^+ \frac{\nu_y}{\nu_E} - L_y^+)(L_E^- \frac{\nu_x}{\nu_E} - L_x^-) - 4(L_E^+ \frac{\nu_x}{\nu_E} - L_x^+)(L_E^- \frac{\nu_y}{\nu_E} - L_y^-).$$

The integral is now over $M_{W(1,2)}$ since the Ws are produced primarily on-shell.

6.3 $ZZ \to \ell\bar{\ell}\nu\bar{\nu}$

The ZZ mode considered here is $p\bar{p} \to ZZ \to \ell\bar{\ell}\nu\bar{\nu}$ which is the decay most likely to pass the event selection described in section 5.5. The differential cross section for this process can be written as

$$\frac{d\sigma_{ZZ}}{dx} = \frac{1}{16(2\pi)^8} \int \frac{f(x_1)f(x_2)|\mathcal{M}_{ZZ}|^2}{16x_1x_2E_{Beam}^4} \frac{1}{2L_{E_1}\bar{\nu}_z/L_{E_2} - 2\nu_z} \frac{d\nu_x d\nu_y d\nu_z dM_Z^2}{L_{E_1}L_{E_2}\nu_e\bar{\nu}_E}. \quad (6.4)$$

Only like flavor dilepton types are considered here. Dilepton types that are not like flavor are assigned a zero probability.

6.4 $W\gamma$

The decay considered here is that of $W\gamma \to \ell\nu\gamma$. It becomes a dilepton background when the photon has been falsely identified as an electron. Here there is only one neutrino which is only unconstrained in ν_z. The differential cross section is given by

$$\frac{d\sigma_{W\gamma}}{dx} = \frac{1}{8(2\pi)^5} \int \frac{f(x_1)f(x_2)|\mathcal{M}_{W\gamma}|^2}{16x_1x_2E_{Beam}^2} \frac{d\nu_z}{L_E\gamma_E\nu_E}. \quad (6.5)$$

6.5 W+Jet

Considered here is the process of $W(\to \ell\nu)$+parton. It gives a dilepton signature when the parton which fragments to give a jet has been misidentified as a lepton which is assumed in the calculation. As in $W\gamma$ there is only one unconstrained parameter which is the neutrino z-momentum ν_z, with the differential cross section

given by

$$\frac{d\sigma_{Wp}}{dx} = \frac{1}{8(2\pi)^5} \int \frac{f(x_1)f(x_2)|\mathcal{M}_{Wp}|^2}{16x_1x_2E_{Beam}^2} \frac{d\nu_z}{L_E p_E \nu_E} \tag{6.6}$$

6.6 Forming a Likelihood Ratio

The matrix element based probabilities described by equation 6.1 are combined into a likelihood ratio. This likelihood ratio is defined as

$$LR_X = \frac{P_X}{P_X + \sum_{i \neq X} k_i P_i} \tag{6.7}$$

where X is the signal of interest and the sum is over the background probabilities i. k_i is the relative yield for the process i among the backgrounds such that

$$\sum_{i \neq X} k_i = 1.$$

In practice the likelihood ratio is dependent on the dilepton types listed in table 9.1. That is, the relative fraction k_i for each process is different for the different dilepton types, and this difference is accounted for by computing LR_X specifically for the dilepton final state that is observed. The relative yield k_i is also computed by scaling the calculated yields from the values used in the analysis (which may be NLO, NNLO, NNLL, and so on) to the LO cross sections for consistency.

Figure 6.1 shows the likelihood ratios for the signals $X = (WW, ZZ, W + \text{jet}, \text{W}\gamma)$. The Higgs is not considered as a background in the likelihood ratios for these signals. The likelihood ratios for the HWW signal are shown for each mass in figures 6.2, 6.3, and 6.4.

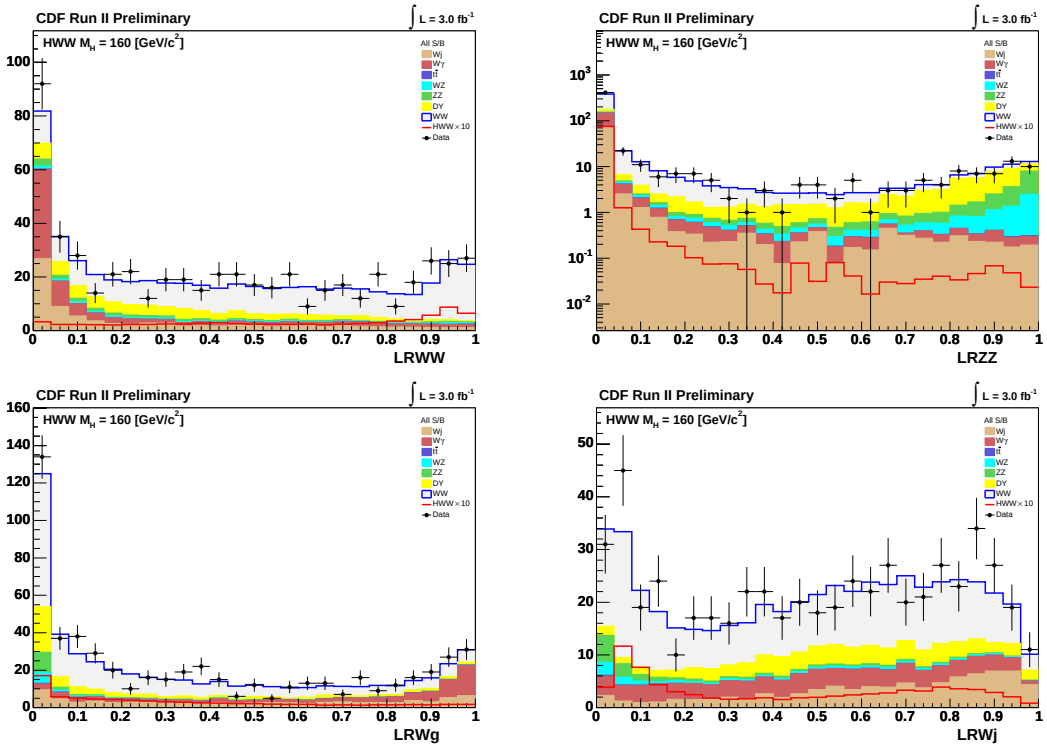

Figure 6.1: Likelihood ratios LR_X, clockwise from upper left $X = (WW, ZZ, W+$ jet, $\mathrm{W}\gamma)$.

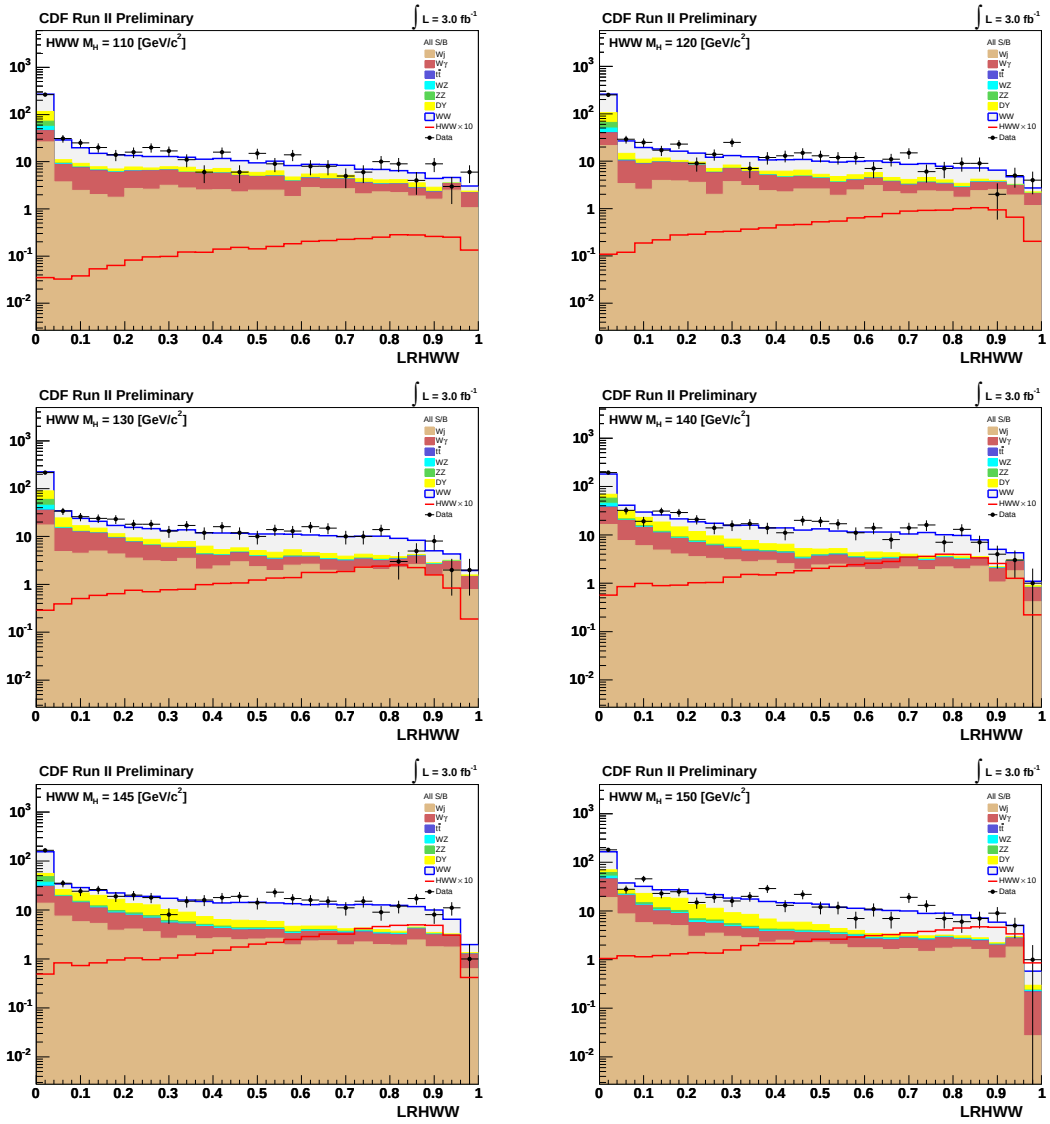

Figure 6.2: Likelihood ratios LR_{HWW} for $110 \geq M_H \geq 150$ GeV.

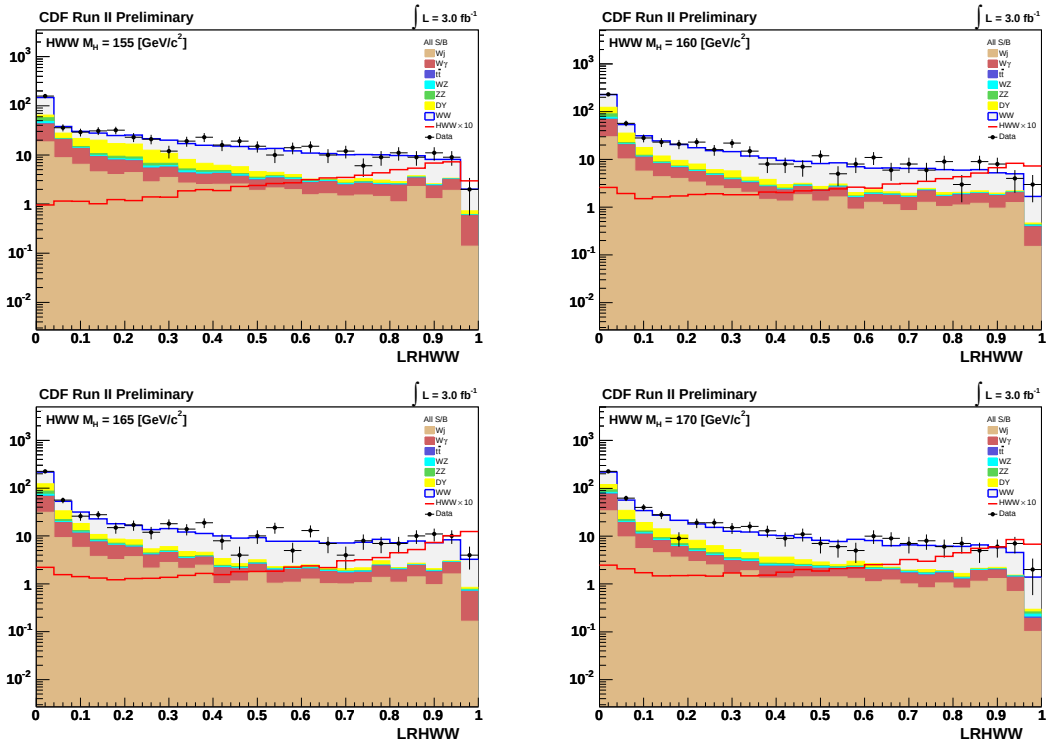

Figure 6.3: Likelihood ratios LR_{HWW} for $155 \geq M_H \geq 170$ GeV.

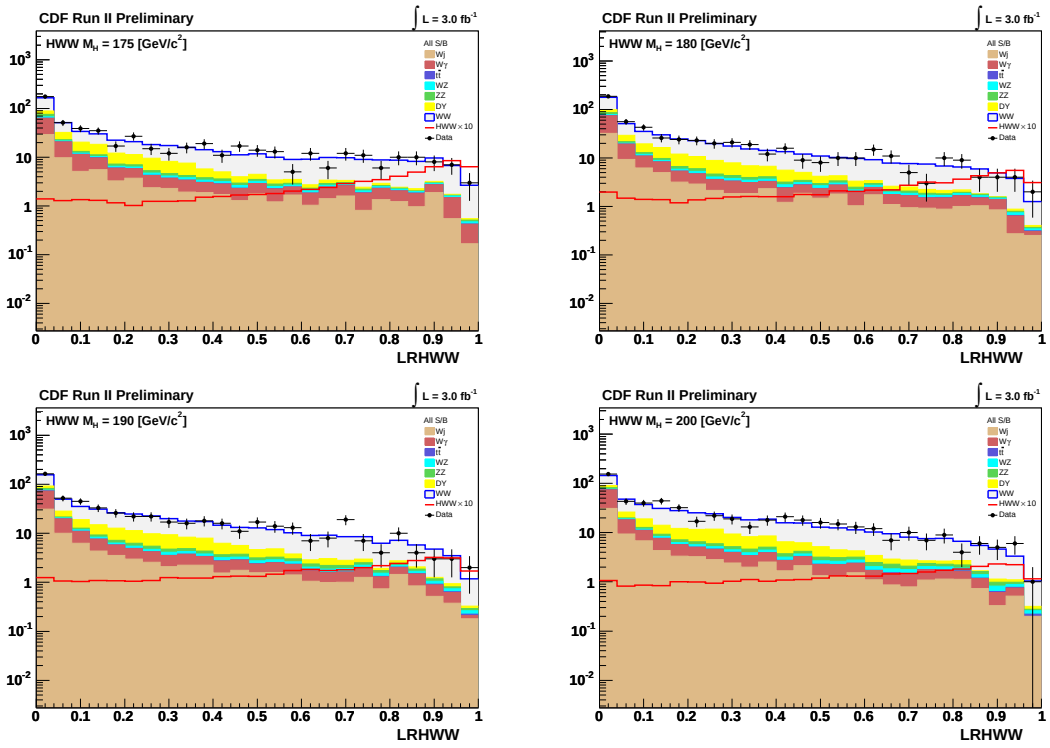

Figure 6.4: Likelihood ratios LR_{HWW} for $175 \geq M_H \geq 200$ GeV.

Chapter 7

Measuring the WW Cross Section

The most important background in this analysis is W boson pair production where both Ws decay leptonically giving two leptons and two neutrinos in the final state at leading order (recall figure 2.7 for the Feynman diagrams). This is the same final state as in the case of the process $gg \to H \to WW$. Since this single Higgs production is by far the largest among the signal processes at low jet multiplicity it is crucial that the WW process is both well modeled and well understood. The remainder of this chapter focuses on measuring the WW cross section as verification that this is well understood at in this analysis.

7.1 Theory and Previous Measurements

The theoretical value for the $p\bar{p} \to WW$ cross section at $\sqrt{s} = 1.96$ TeV is calculated at next-to leading order using MCFM [14]. This value is

$$\sigma_{WW}^{NLO} = 12.4 \pm 0.8 \text{ pb.} \tag{7.1}$$

Analysis	Measured cross section	$\int \mathcal{L}dt$ (pb^{-1})
CDF - Dilepton	$14.6^{+5.8}_{-5.1}$(stat) $^{+1.8}_{-3.0}$(syst) $\pm$ 0.9(Lumi) (pb)	184
CDF - Lepton+Track	24.4 ± 6.9(stat) $^{+5.2}_{-5.7}$(syst) $\pm$ 1.5(Lumi) (pb)	184
D0 - Dilepton	$13.8^{+4.3}_{-3.8}$(stat) $^{+1.2}_{-0.9}$(syst) $\pm$ 0.9(Lumi) (pb)	224-252

Table 7.1: Previous WW cross section measurements from CDF and D0 using between 184 and 252 pb^{-1}. The statistical, systematic and luminosity uncertainties are given separately.

Previous published measurements from both CDF [20] and D0 [22] using between 184 and 252 pb^{-1} of data are given in table 7.1. These measurements are the results of counting experiments only.

7.2 WW Signal Estimates

Here WW is treated as the signal and all other processes as backgrounds. No Higgs hypothesis is considered in measuring the WW cross section. The event selection criterion is exactly the same as that for the Higgs selection for 0 and 1 jets, as described in section 5.5. Table 7.2 gives WW and background estimates along with the number of events observed in data for events with 0 jets and events with ≤ 1 jet.

Process	0 Jets	0 or 1 Jet
Z/γ^*	66.9 ± 15.2	71.2 ± 16.2
WZ	12.2 ± 1.9	12.7 ± 2.0
$W\gamma$	79.2 ± 21.1	11.4 ± 3.0
W+jets	83.6 ± 20.1	26.2 ± 6.8
ZZ	17.3 ± 2.7	4.5 ± 0.7
$t\bar{t}$	1.0 ± 0.2	24.6 ± 4.8
Total Background	260.1 ± 37.1	150.6 ± 21.0
WW	280.4 ± 39.0	355.5 ± 47.7
Signal+Background	540.5 ± 64.8	766.2 ± 86.5
Data	**552**	**779**

Table 7.2: Expected events for 0 jet and 0+1 jet categories where WW is considered the signal. The integrated luminosity is 3.0 fb^{-1}.

7.3 LR_{WW} Distributions

The likelihood ratio LR_{WW} distribution is used to measure the WW cross section. The LR_{WW} distributions are shown in figure 7.1 for events with 0 jets as well as for events with 0 or 1 jet. The cross section is measured for both scenarios as a check of the robustness of this analysis.

7.4 Maximum Likelihood

A maximum likelihood method is used to measure the WW cross section. The LR_{WW} data distributions are fit to the expected component shapes, the normalizations of which all constrained withing their uncertainties except for that of WW which is allowed to float in the fit. The best fit, given by the maximum of the likelihood function, is then used to extract the WW cross section.

A likelihood function is formed from the Poisson probabilities for each bin in

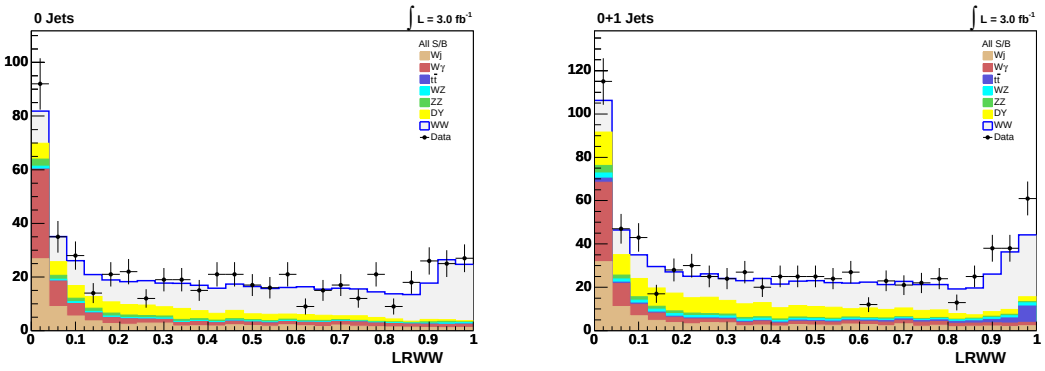

Figure 7.1: Likelihood ratio LR_{WW} for 0 jet events (*left*) and 0+1 jet events (*right*) used in the WW cross section measurement. Signal and backgrounds here are scaled to their absolute prediction.

LR_{WW} where the Poisson probability is given by

$$P_i = \frac{\mu_i^{n_i} e^{-\mu_i}}{n_i!}. \tag{7.2}$$

Here μ_i is the expected number of events in the i-th bin and n_i the number observed in data. The expected number of events in each bin is given by

$$\mu_i = \sum_k \alpha_k \left[\prod_c (1 + f_k^c S_c) \right] (N_k^{Exp})_i \tag{7.3}$$

where the sum k is over all signal and background processes considered. α_k is an overall normalization on the prediction for each process. This α_k is allowed to float freely for signal and is fixed at 1 for all backgrounds. The fractional uncertainty for a given systematic c for process k is given by f_k^c. The number of expected events from the process k in the i-th bin is given by $(N_k^{Exp})_i$. These systematics are the same systematics discussed in chapter 10. The only exception to this is that the error

on the theoretical cross section for WW has been removed since the cross section itself is what is being measured here. The systematics themselves are allowed to float in the fit. This floating parameter for each systematic c is represented by S_c and is constrained by a Gaussian function in the likelihood. This has the effect that the systematics are correlated in the likelihood across all processes and bins (where desired) and given that this S_c is a multiplicative factor of the fractional uncertainties, it adequately represents the $\pm 1\sigma$ uncertainties which are assumed to be Gaussian themselves.

The likelihood is then a product of the Poisson probabilities over all bins multiplied by the Gaussian constraints on the systematic uncertainties which is given by

$$\mathcal{L} = \left(\prod_i \frac{\mu_i^{n_i} e^{-\mu_i}}{n_i!} \right) \cdot \prod_c e^{\frac{S_c^2}{2}}. \tag{7.4}$$

with μ_i given in equation 7.3.

Maximizing this likelihood with respect to α_{WW} and the S_c parameters then gives a measurement of the WW yield as a ratio to the expected yield. This ratio (α_{WW}) is then interpreted as the ratio of the measured cross section to the input cross section in the expected yield calculation σ_{WW}^{NLO}.

In practice it is the negative log-likelihood which is minimized, which is equivalent to maximizing the likelihood. The minimization is performed by the MINUIT package [2].

7.5 Pseudo-experiments

Pseudo-experiments are generated by first fluctuating the number of expected events for each process by its systematic uncertainties in a correlated fashion giving G_k as the fluctuated mean which is defined by

$$G_k = N_k^{Exp} \prod_c (1 + f_k^c g_c). \tag{7.5}$$

Here g_c is an array of random numbers distributed according to a Gaussian distribution with a mean of zero and width of 1. Thus the systematic uncertainties are varied in a correlated fashion among all processes (where desired). Next a random Poisson number is drawn where G_k is given as the mean for each process k as in

$$P_k = \text{Poisson}(G_k). \tag{7.6}$$

This number, P_k, is then the number of events that will be drawn from the LR_{WW} template for process k according to its LR_{WW} probability distribution and added to the pseudo-data template.

Once this pseudo-data template is constructed it is run through the minimization exactly as if it were data. Results of 10,000 of these pseudo-experiments are then tallied. The results of these measurements for pseudo-experiments is shown in figure 7.2. The "true value" in figure 7.2 is the number of WW events generated in a pseudo-experiment divided by the nominal prediction and the "measured" value is the value returned by the fit. The measured positive and negative errors are shown in figure 7.3. These errors include all statistical, systematic, and luminosity

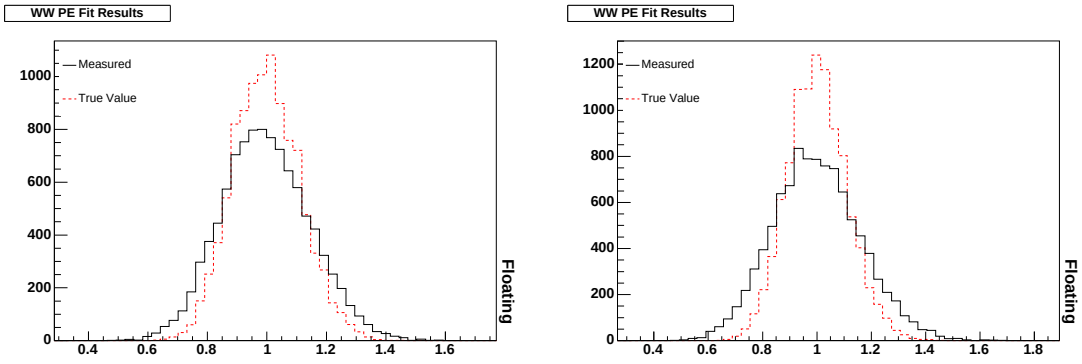

Figure 7.2: Results of the WW cross section measurement from pseudo-experiments. The cross section is given as a ratio to the NLO cross section for 0-jet events (*left*) and 0+1 jet events (*right*).

uncertainties and quantify what one should expect to measure in the data.

The pull for asymmetric errors is defined as

$$g = \begin{cases} \frac{\tau_g - \tau_m}{|\sigma_m^+|} & \text{for } \tau_m \leq \tau_g \\ \frac{\tau_m - \tau_g}{|\sigma_m^-|} & \text{for } \tau_m > \tau_g \end{cases} \tag{7.7}$$

where τ_g is the generated value and τ_m is the measured value. $\sigma_m^{\pm}$ are the positive and negative errors. Pull distributions for pseudo-experiments are shown in figure 7.4. While these distribution appear to be somewhat Gaussian, centered at zero with unit width thereby validating the procedure, it should be noted that for the case of asymmetric errors one does not always expect a unit Gaussian.

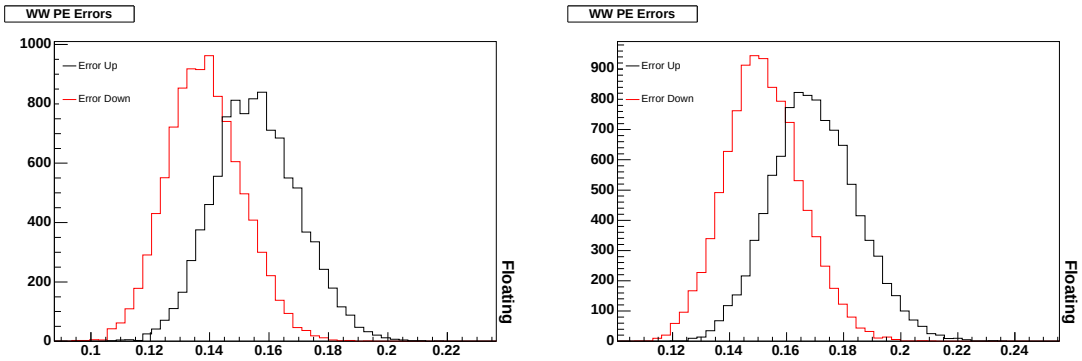

Figure 7.3: Fractional errors from pseudo-experiments for 0-jet events (*left*) and 0+1 jet events (*right*).

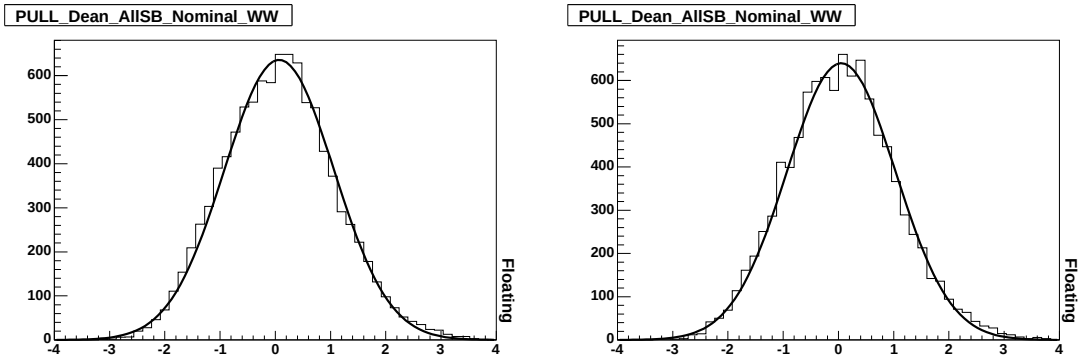

Figure 7.4: Pull distributions for σ_{WW} from pseudo-experiments for 0-jet events (*left*) and 0+1 jet events (*right*).

7.6 Results of the WW Cross Section Measurement

Interpreting α_k^{WW} as a measurement of the WW cross section for 0-jet events gives a cross section

$$\sigma(p\bar{p} \to WW) = 13.2^{+2.0}_{-1.8}(\text{pb}) \tag{7.8}$$

where the given uncertainties include statistical, systematic, and luminosity contributions. This is shown graphically in the LR_{WW} template in figure 7.5 where the colored histograms are scaled to the fit values for the systematic parameters S_c and α_k^{WW}. The nominal prediction for signal plus background is given by the dashed orange line.

When events with 0 and 1 jet are used in the fit the measured cross section is

$$\sigma(p\bar{p} \to WW) = 13.7^{+2.2}_{-1.9}(\text{pb}) \tag{7.9}$$

and is shown graphically in figure 7.6.

Both measurements of σ_{WW} are in very good agreement with the SM prediction at NLO given in equation 7.1. This is very convincing evidence that the WW cross section is well measured at CDF and in this analysis framework. It also gives confidence that the most crucial background in this $H \to WW$ search is well understood and well modeled.

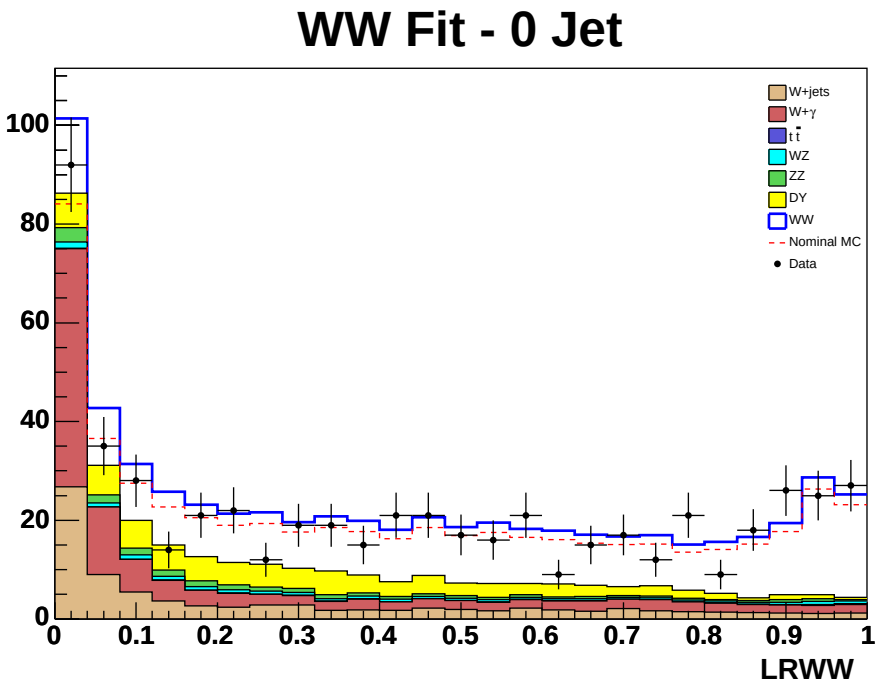

Figure 7.5: Results of maximization of the likelihood for 0-jet events with respect to the WW cross section and systematic uncertainties. The nominal prediction is shown as the dashed orange line.

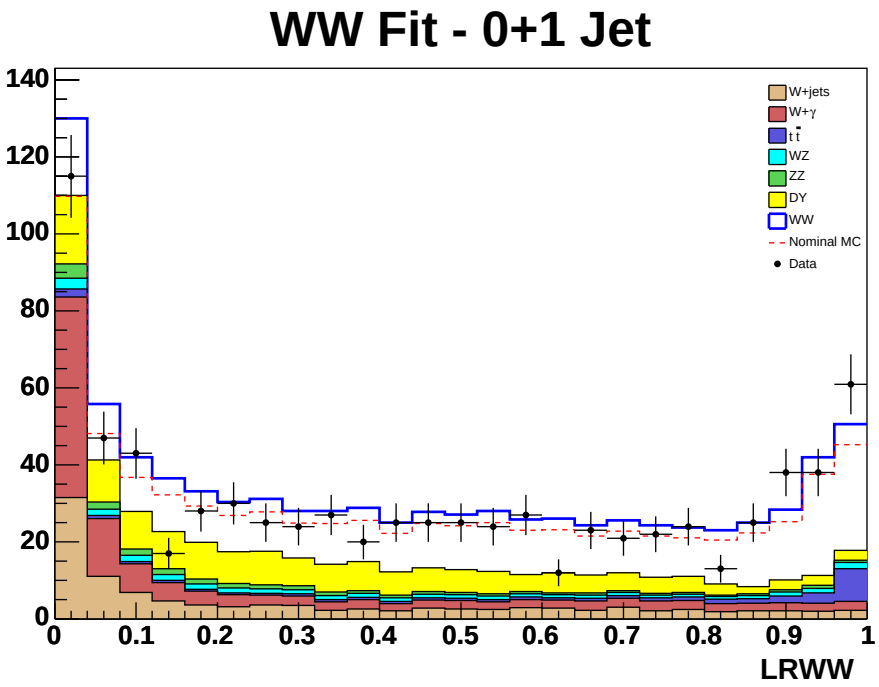

Figure 7.6: Results of maximization of the likelihood for 0 and 1 jet events with respect to the WW cross section and systematic uncertainties. The nominal prediction is shown as the dashed orange line.

Chapter 8

An Introduction to Artificial Neural Networks

In this analysis artificial neural networks are used to discriminate signal and background events. The type of neural network used in this analysis consists of 3 "layers" which are made up of "nodes". An example of this is shown in figure 8.1. The first layer is the input layer and the "input" to the nodes in this layer are chosen by the user. In this analysis the inputs to the first layer are kinematic variables and matrix element based likelihood ratios which describe the events of interest. Every node is essentially just a function, the output of which will be used as the input for the nodes in the next layer. The function typically used is the sigmoid function given by

$$g(x) = 1/(1 + e^{-x/T}) \tag{8.1}$$

and shown in figure 8.2.

Weights are assigned for the inputs to each node. The total input to a node j will then be the some of the inputs g from the nodes k times their weights w_{jk} as

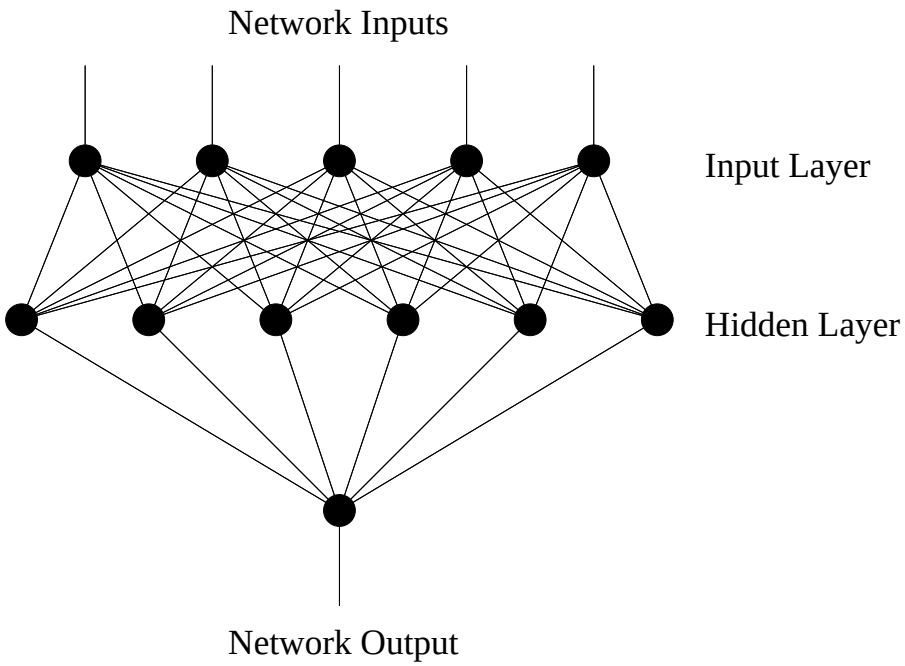

Figure 8.1: A typical neural network architecture consisting of 5 input nodes, 6 hidden nodes, and out output node.

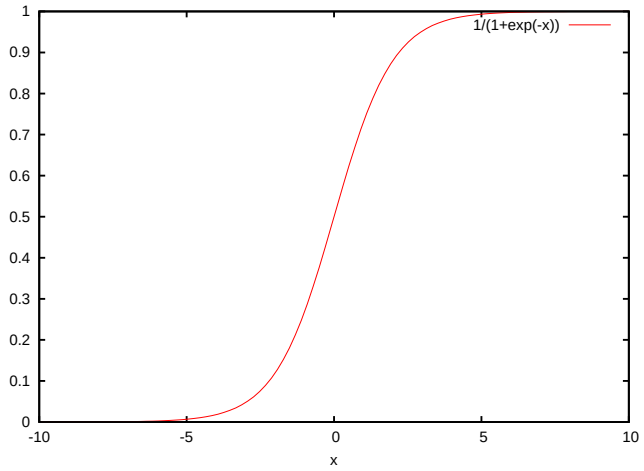

Figure 8.2: Sigmoid function which is typical of a node in a neural network.

given by

$$x_j = \sum_k w_{jk} g_k. \tag{8.2}$$

Once the sum of the inputs is calculated it can be input into equation 8.1 to calculate that nodes output value. The weights w_{jk} are initially randomized, but are adjusted, or "learned", in "training" the network based on the desired and actual output of the neural network.

The third layer consists of a single node which is called the output node. The output of this node is used to discriminate signal from background.

A neural network is trained using datasets with known signal and background events. In training, a neural network is given many variables as input for known events which it then uses to adjust the weights for each input connection in internal layers. Once the neural network is trained it can be used taking the same inputs form any data and typically gives an output ranging from -1 to 1 on, for the purpose of this analysis, what is a single output node.

The neural network package used in this analysis is the NeuroBayes® neural network package. NeuroBayes is a Bayesian neural network, which instead of considering the single set of weights which maximize the fit to the training data, considers a probability distribution of sets of network weights. These probability distributions are updated during training such that weight distributions which fit the training data well will be given a higher probability. The network can then provide not just a number for the output, but a probability distribution. In this analysis the maximum of this probability distribution is used. The details of the NeuroBayes package are explained elsewhere [33, 34].

When events are given to the neural network they are given with a weight which is considered by the network. The weights given to the network are such that each signal event has unity weight. The background event weights are then the event weights as described in section 5.4.1 which have been normalized such that the sum of these weights over all backgrounds is equal to the number of signal events given to the network.

Chapter 9

Analysis

This analysis considers only dilepton events which have significant missing transverse energy and satisfy the event selection described in section 5.5. Background estimates and observed events in data are the same for each Higgs mass investigated since the selection criterion is the same regardless of the Higgs mass in question.

The analysis is separated into 3 main channels by jet multiplicity. The definition of a jet is given in section 4.2. The first channel requires zero jets and makes use of both matrix element (see chapter 6) calculations as well as neural networks (see chapter 8). The second main channel, which makes use of neural networks, requires one and only one jet. The last channel consists of events which have two or more jets and makes use of neural networks.

These first two channels are both divided into two sub-channels denoted as *high S/B* and *low S/B* referring to their relative signal to background content. These sub-channels are defined by the dilepton types which they are composed of. The allowed dilepton types along with which sub-channel they belong to are listed in table 9.1.

The final discriminant for each of the channels is a neural network output. The three main channels are discussed individually in the following sections and the

High S/B	Low S/B
TCE-TCE	TCE-PHX
TCE-CMUP	PHX-PHX
TCE-CMX	PHX-CMUP
TCE-CMIOCES	PHX-CMX
TCE-CMIOPES	PHX-CMIOCES
CMUP-CMUP	PHX-CMIOPES
CMUP-CMX	PHX-CrkTrk
CMUP-CMIOCES	CMUP-CMIOPES
CMX-CMX	CMX-CMIOPES
CMX-CMIOCES	
TCE-CrkTrk	
CMUP-CrkTrk	
CMX-CrkTrk	

Table 9.1: Dilepton types sorted by high and low signal to background sub-channels.

combination of all channels in setting limits is discussed in section 11.4.

9.1 Zero Jet Events

For events with zero reconstructed jets, both matrix element calculations and neural networks are employed. The matrix element based likelihood ratios described in section 6.6 are used in conjunction with kinematic variables as input to a neural network.

The dominant background in the zero jet channel is WW production, which is somewhat unfortunate as it is also the background which is most difficult to distinguish from the Higgs signal. Of the signal production mechanisms discussed in section 2.5.1, only the direct production channel $gg \rightarrow H$ contributes significantly and is the only signal considered in this channel. The other production mechanisms

Process	High S/B			Low S/B			Total		
$t\bar{t}$	0.80	±	0.16	0.17	±	0.03	0.96	±	0.19
DY	39.01	±	8.87	27.86	±	6.33	66.88	±	15.20
WW	206.28	±	28.68	74.14	±	10.31	280.42	±	38.99
WZ	8.52	±	1.35	3.65	±	0.58	12.17	±	1.93
ZZ	12.72	±	2.02	4.57	±	0.72	17.29	±	2.74
W+jets	34.16	±	9.46	49.45	±	10.63	83.61	±	20.09
$W\gamma$	21.23	±	5.67	57.92	±	15.45	79.15	±	21.12
Total Background	**322.73**	±	**39.38**	**217.75**	±	**27.29**	**540.48**	±	**64.77**
$gg \to H$	6.84	±	1.06	1.54	±	0.24	8.38	±	1.29
Data	**322**			**230**			**552**		

HWW 0 Jet

Table 9.2: Summary of expected and observed events in the 0-jet channel. These background estimates are the same for each Higgs mass investigated. The $gg \to H$ prediction is given for $M_H = 160$ GeV for reference.

have either extra leptons or jets which do not lend themselves to this channel. Table 9.2 shows background prediction and the number of events observed in data along with the $gg \to H$ prediction at $M_H = 160$ GeV for the high and low S/B sub-channels. The signal predictions for each mass is shown individually in table 9.3.

Five variables are used as inputs to a neural network. Many variables were investigated, however these were determined to be the five most significant variables in this channel after many optimization studies [3]. The five input variables are LR_{HWW}, LR_{WW}, H_T, $\Delta\phi_{\ell\ell}$, and $\Delta R_{\ell\ell}$, where H_T is the scalar sum of the E_T in the calorimeter and the $\not\!\!E_T$ (both corrected for muons). Distributions for these five input variables are shown in figure 9.1.

A NeuroBayes neural network is trained on a weighted sample of simulated signal and background events. The event weighting is described in section 5.4.1. The one exception to this is the W+jets sample, which is not from simulation, but from the data itself. This sample of events does not overlap with the signal selection region.

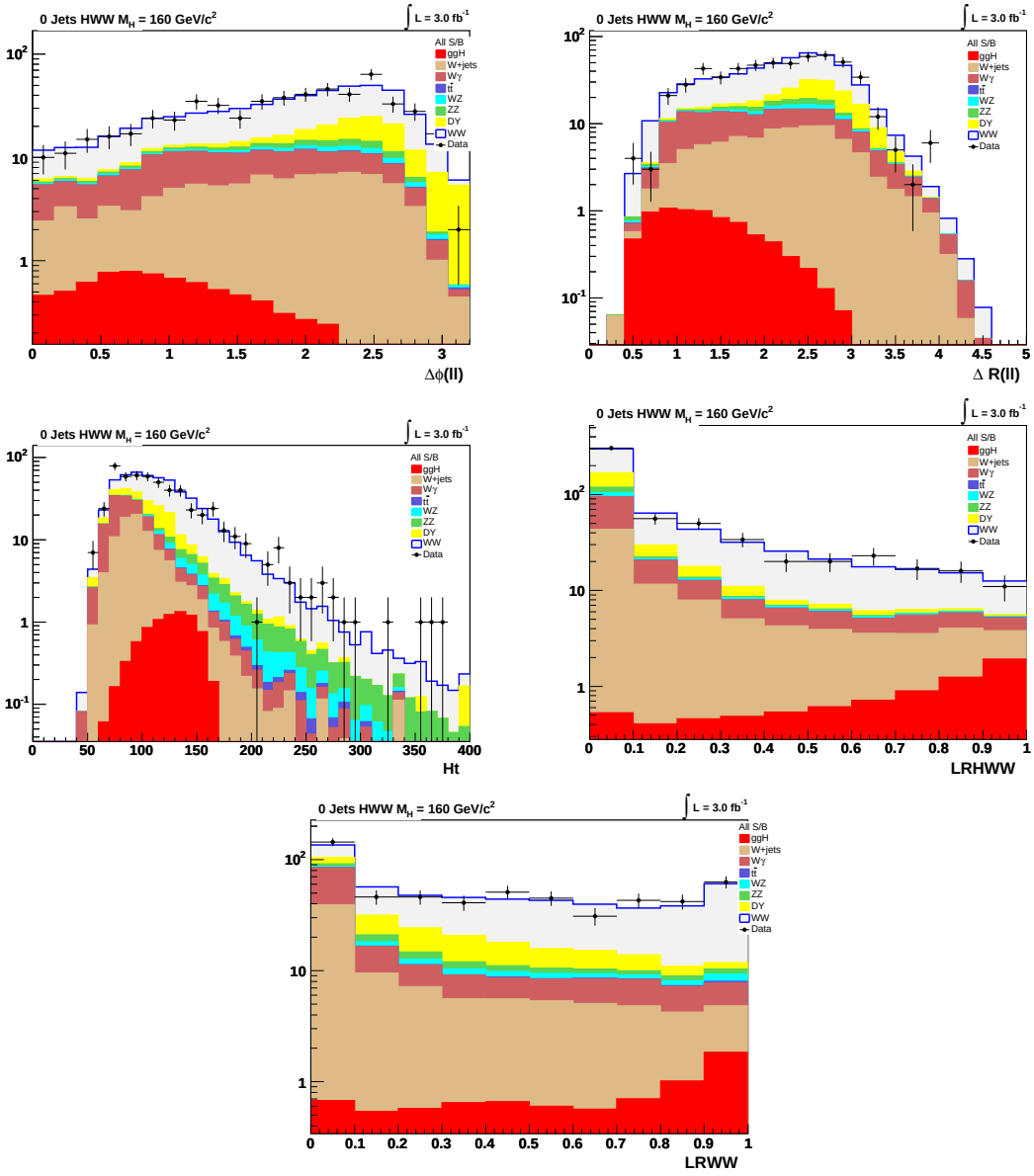

Figure 9.1: Input variables for the 0-jet neural network for $M_H = 160$ GeV.

M_H (GeV)	High S/B			Low S/B			Total		
110	0.32	±	0.05	0.08	±	0.01	0.40	±	0.06
120	1.11	±	0.17	0.28	±	0.04	1.39	±	0.22
130	2.55	±	0.39	0.63	±	0.10	3.18	±	0.49
140	4.10	±	0.63	1.06	±	0.16	5.16	±	0.80
145	4.75	±	0.73	1.19	±	0.18	5.93	±	0.92
150	5.38	±	0.83	1.36	±	0.21	6.75	±	1.04
155	6.13	±	0.95	1.49	±	0.23	7.62	±	1.18
160	6.84	±	1.06	1.54	±	0.24	8.38	±	1.29
165	6.64	±	1.03	1.51	±	0.23	8.15	±	1.26
170	6.13	±	0.95	1.41	±	0.22	7.54	±	1.16
175	5.45	±	0.84	1.31	±	0.20	6.76	±	1.04
180	4.87	±	0.75	1.17	±	0.18	6.04	±	0.93
190	3.29	±	0.51	0.82	±	0.13	4.11	±	0.63
200	2.57	±	0.40	0.66	±	0.10	3.23	±	0.50

HWW 0 Jet

Table 9.3: Expected signal events from $gg \rightarrow H$ in the 0-jet channel for high and low S/B channels for different Higgs masses investigated.

One neural network is trained for 0-jet events at each of the 14 masses investigated. The neural network for each mass is trained on both high and low S/B events without any distinction between the two (other than the inherent geometric and kinematic differences associated with the different dilepton types). The network is structured such that there are 5 input nodes (one for each of the variables shown in figure 9.1), 5+1 nodes in a single hidden layer, and one output node. The target output for signal is +1 and for background is -1.

Once the neural network has been trained, templates are created for the signal and background using all available events. Here a distinction is made between high and low S/B as the events are sorted into the two different sub-channels after passing through the same neural network. Neural network output for $M_H = 160$ and 170 GeV high and low S/B for are shown in figure 9.2. For completeness the

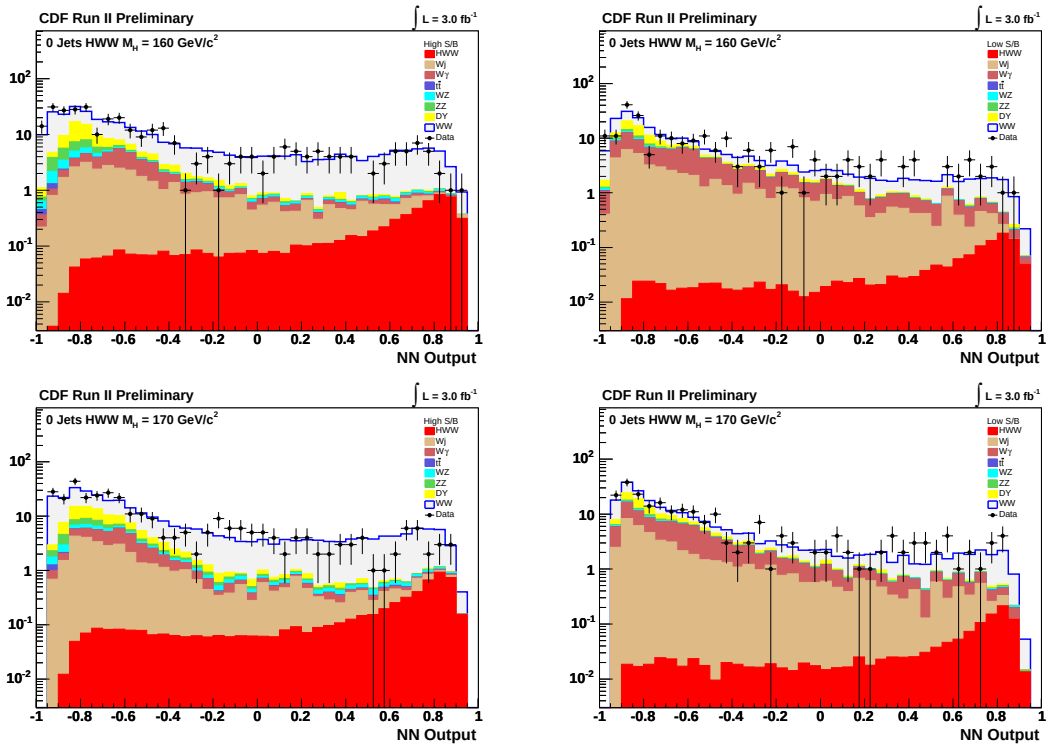

Figure 9.2: Neural network output for high S/B (*left*) and low S/B (*right*) 0-jet events for $M_H = 160$ GeV (*top*) and $M_H = 170$ GeV (*bottom*).

remainder can be found in appendix A. These templates are exactly what is used when computing limits on SM Higgs production which is discussed in chapter 11.

9.2 One Jet Events

Events in this channel are required to pass the event selection described in section 5.5 and have one and only one jet. A neural network is used to discriminate signal from background for events in this channel. Four signal production mechanisms are considered in the 1-jet channel which are $gg \to H$, WH, ZH, and VBF as described in section 2.5.1. The expected contributions of each of these signal processes for

Process	High S/B			Low S/B			Total		
$t\bar{t}$	20.10	±	3.90	4.47	±	0.87	24.57	±	4.77
DY	47.49	±	10.80	23.72	±	5.39	71.21	±	16.19
WW	57.05	±	7.86	18.05	±	2.43	75.10	±	10.11
WZ	8.66	±	1.37	4.05	±	0.64	12.71	±	2.02
ZZ	3.35	±	0.53	1.18	±	0.19	4.53	±	0.72
W+jets	10.28	±	3.24	15.95	±	3.54	26.23	±	6.78
$W\gamma$	2.53	±	0.67	8.82	±	2.33	11.35	±	3.00
Total Background	**149.45**	±	**18.43**	**76.24**	±	**9.19**	**225.69**	±	**27.27**
$gg \to H$	3.35	±	0.11	0.73	±	0.11	4.08	±	0.63
WH	0.46	±	0.06	0.10	±	0.01	0.57	±	0.08
ZH	0.17	±	0.02	0.04	±	0.01	0.21	±	0.03
VBF	0.28	±	0.05	0.05	±	0.01	0.33	±	0.06
Total Signal	**4.26**	±	**0.57**	**0.92**	±	**0.12**	**5.18**	±	**0.69**
Data	**143**			**84**			**227**		

HWW 1 Jet

Table 9.4: Summary of expected and observed events in the 1-jet channel. These background estimates are the same for each Higgs mass investigated. The four Higgs production mechanisms are shown for $M_H = 160$ GeV for reference.

each Higgs mass is given in tables 9.5 and 9.6 for the high and low S/B sub-channels.

A neural network is trained for each of the 14 masses investigated using 8 variables. The variables are $M_{\ell\ell}$, $\Delta R_{\ell\ell}$, H_T, E_ℓ^1 shown in figure 9.3 as well as $P_T(\ell_1)$, $P_T(\ell_2)$, $\not\!\!E_T^{spec}$, and the transverse mass using the leptons along with the $\not\!\!E_T$ shown in figure 9.4.

Once each neural network has been trained, signal and background templates are created from the network output and compared with the NN data distribution output. Both high and low S/B events are used to train the NN, but are separated into their respective sub-channels when creating templates. A sample of these templates is shown in figure 9.5 for $M_H = 160$ and 170 GeV. For completeness all of the 1-jet templates are given in appendix A.

Signal in the 1 Jet High S/B Sub-Channel					
M_H (GeV)	$gg \to H$	WH	ZH	VBF	High S/B Total
110	0.13	0.07	0.02	0.01	0.23 ± 0.03
120	0.48	0.17	0.05	0.04	0.75 ± 0.09
130	1.11	0.31	0.10	0.09	1.60 ± 0.20
140	1.89	0.40	0.14	0.15	2.58 ± 0.33
145	2.20	0.43	0.15	0.18	2.96 ± 0.38
150	2.63	0.45	0.16	0.21	3.45 ± 0.45
155	3.07	0.46	0.17	0.25	3.95 ± 0.52
160	3.35	0.46	0.17	0.28	4.26 ± 0.57
165	3.37	0.43	0.16	0.29	4.25 ± 0.57
170	3.12	0.39	0.15	0.28	3.94 ± 0.53
175	2.86	0.25	0.13	0.26	3.50 ± 0.48
180	2.57	0.31	0.12	0.24	3.24 ± 0.43
190	1.81	0.21	0.08	0.18	2.28 ± 0.30
200	1.49	0.16	0.06	0.15	1.49 ± 0.25

Table 9.5: Expected number of Higgs events in the 1-jet high S/B sub-channel for the different production mechanisms considered at each of the 14 masses investigated.

Signal in the 1 Jet Low S/B Sub-Channel					
M_H (GeV)	$gg \to H$	WH	ZH	VBF	Low S/B Total
110	0.03	0.02	0.01	0.00	0.06 ± 0.01
120	0.11	0.04	0.01	0.01	0.17 ± 0.02
130	0.26	0.08	0.02	0.02	0.38 ± 0.05
140	0.43	0.10	0.03	0.03	0.59 ± 0.08
145	0.50	0.10	0.03	0.04	0.67 ± 0.09
150	0.58	0.11	0.04	0.04	0.77 ± 0.10
155	0.68	0.11	0.04	0.04	0.87 ± 0.12
160	0.73	0.10	0.04	0.05	0.92 ± 0.12
165	0.72	0.09	0.04	0.06	0.91 ± 0.12
170	0.66	0.08	0.03	0.06	0.84 ± 0.11
175	0.61	0.05	0.03	0.05	0.74 ± 0.10
180	0.60	0.07	0.03	0.05	0.75 ± 0.10
190	0.41	0.05	0.02	0.04	0.51 ± 0.07
200	0.34	0.03	0.01	0.03	0.42 ± 0.06

Table 9.6: Expected number of Higgs events in the 1-jet low S/B sub-channel for the different production mechanisms considered at each of the 14 masses investigated.

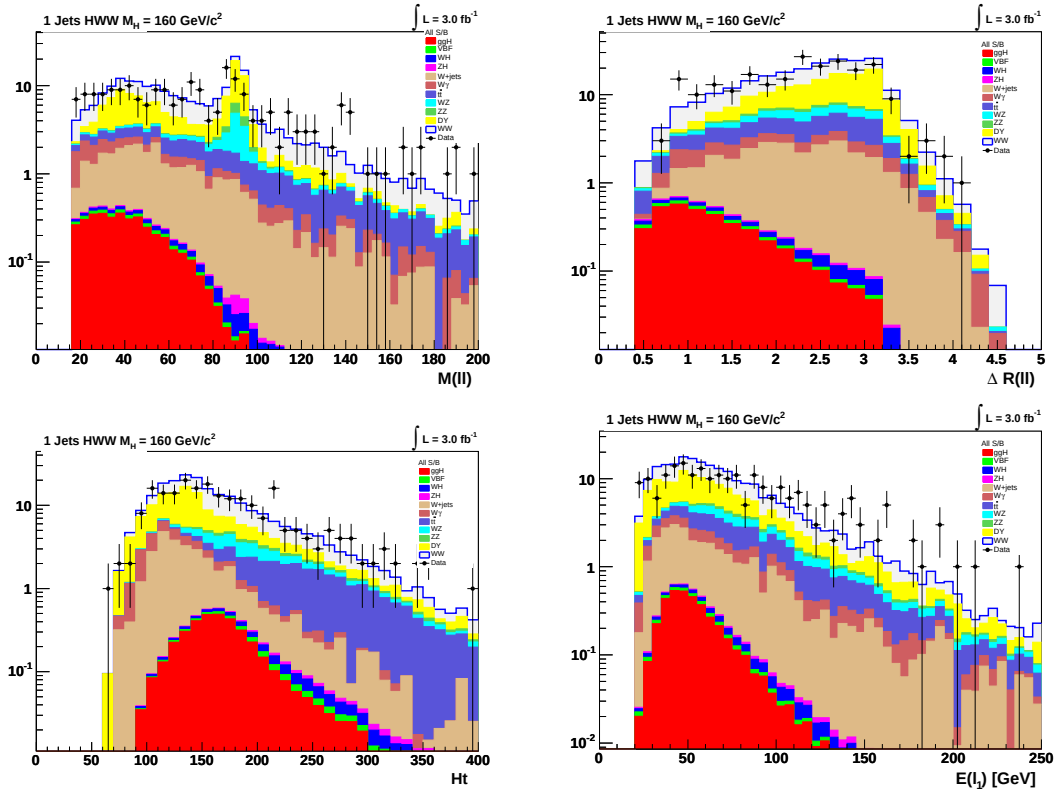

Figure 9.3: Input variables to the 1-jet neural network.

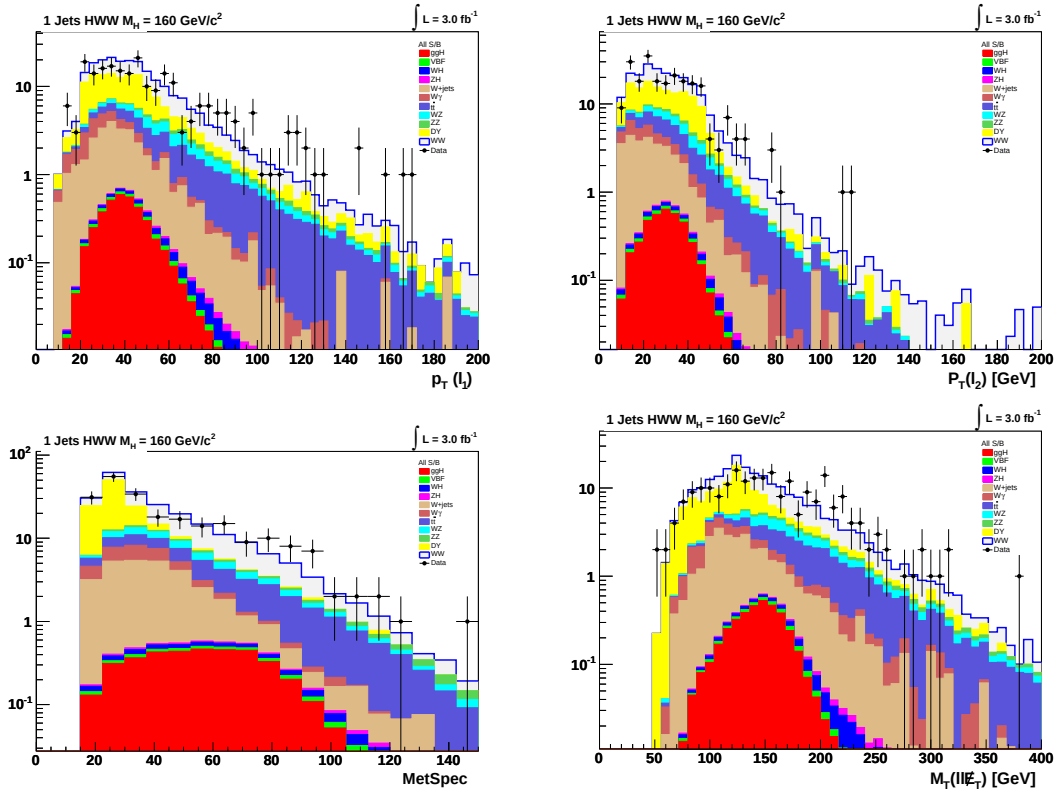

Figure 9.4: Input variables to the 1-jet neural network.

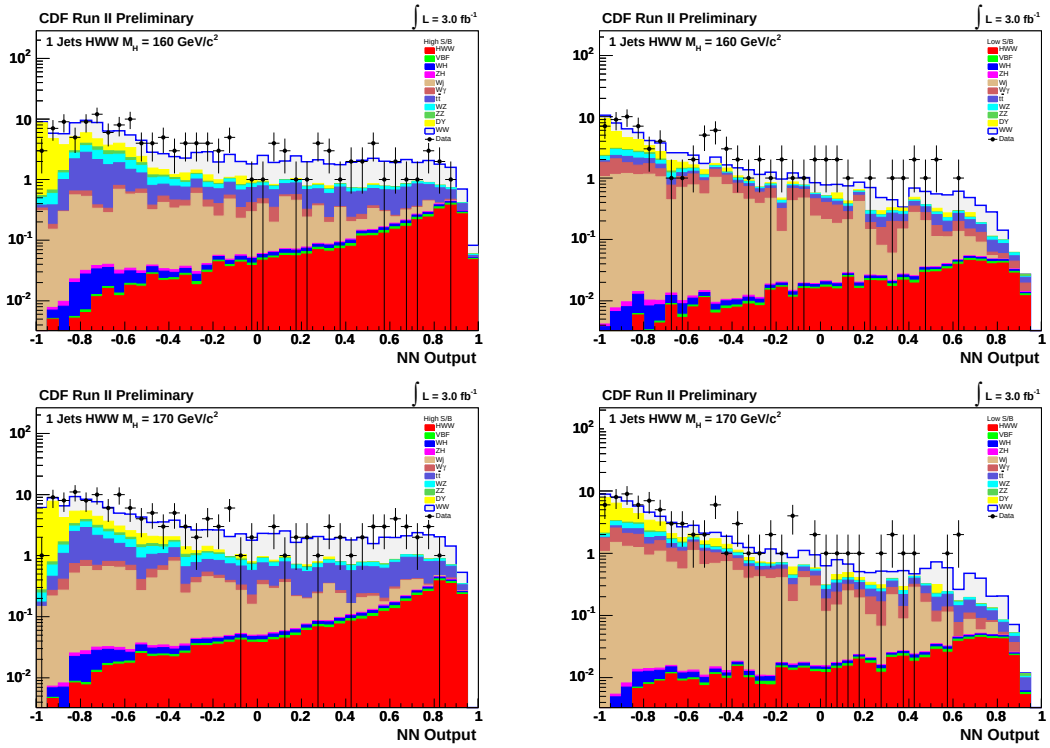

Figure 9.5: Neural network output for high S/B (*left*) and low S/B (*right*) 1-jet events for $M_H = 160$ GeV (*top*) and $M_H = 170$ GeV (*bottom*).

9.3 Two or More Jet Events

This channel consists of events passing the high-level cuts described in section 5.5 which have two or more reconstructed jets. The dominant background in this channel is $t\bar{t}$ where the final state has two leptons, $\not\!\!E_T$ from neutrinos, and two b-quark jets. Top quark pair production distinguishes itself from the other backgrounds with 2 or more jets and missing energy in that the b-quarks, which will form B mesons or hadrons, have a long enough lifetime that their decay can be identified by tracks which point back to a point which is displaced from the $p\bar{p}$ interaction point. These vertices are typically displaced on the order of a millimeter.

To reduce the background from top pair production, events in this region are required to not have a secondary vertex. This reduces the $t\bar{t}$ background by 57%. Signal events in a $H \to WW$ decay are not expected to have displaced vertices and are only minimally affected by tracking uncertainties which may lead to the false identification of a secondary vertex (b-tag). The expected number of events before and after this b-jet veto from the various backgrounds along with signal estimates for $M_H = 160$ GeV is given in table 9.7. An anti-b-tag scale factor is also applied to the $t\bar{t}$ Monte Carlo which is a result of a 95% b-tag scale factor applied to the Monte Carlo to account for the difference in b-tag efficiency in the Monte Carlo with respect to the data [37]. The tagging algorithm used in this analysis is the standard *tight* SecVtx algorithm which is described in [28].

Several signal processes naturally lend themselves to this channel. $WH \to WWW$ and $ZH \to ZWW$ will have at least 2 jets in the final state when one of the vector bosons decays hadronically. The W and Z decay hadronically 67.60%

Process	Before Veto			B-tag Veto		
$t\bar{t}$	161.78	±	33.27	70.34	±	14.46
DY	28.30	±	6.89	27.74	±	6.75
WW	16.10	±	2.54	15.68	±	2.47
WZ	3.41	±	0.55	3.33	±	0.53
ZZ	1.43	±	0.23	1.35	±	0.21
W+jets	9.51	±	2.58	8.38	±	2.27
$W\gamma$	1.86	±	0.49	1.80	±	0.47
Total Background	**222.40**	±	**36.06**	**128.62**	±	**18.37**
$gg \to H$	1.55	±	0.27	1.52	±	0.26
WH	1.24	±	0.16	1.18	±	0.16
ZH	0.67	±	0.09	0.59	±	0.08
VBF	0.62	±	0.12	0.61	±	0.12
Total Signal	**4.07**	±	**0.47**	**3.90**	±	**0.45**
Data	**237**			**139**		

HWW $\geq$ 2 Jets

Table 9.7: Signal and background estimates in the $\geq$ 2 jet channel before and after the b-tag veto. These background estimates are the same for each Higgs mass investigated. The signal is shown for $M_H = 160$ GeV for reference.

M_H (GeV)	$gg \to H$	WH	ZH	VBF	Total
110	0.05	0.08	0.04	0.02	0.20 ± 0.02
120	0.19	0.26	0.13	0.08	0.66 ± 0.08
130	0.46	0.53	0.26	0.19	1.45 ± 0.17
140	0.80	0.81	0.41	0.33	2.36 ± 0.27
145	0.97	0.91	0.45	0.39	2.72 ± 0.31
150	1.14	1.00	0.51	0.47	3.12 ± 0.36
155	1.34	1.10	0.56	0.54	3.54 ± 0.41
160	1.52	1.18	0.59	0.61	3.90 ± 0.45
165	1.56	1.12	0.59	0.63	3.90 ± 0.45
170	1.46	1.04	0.55	0.61	3.66 ± 0.43
175	1.38	0.67	0.50	0.57	3.12 ± 0.37
180	1.27	0.87	0.46	0.53	3.13 ± 0.37
190	0.91	0.60	0.32	0.40	2.23 ± 0.26
200	0.75	0.48	0.26	0.33	1.82 ± 0.21

HWW $\geq$ 2 Jets

Table 9.8: Expected number of Higgs events from different production mechanisms at the different masses investigated for the ≥ 2 jet channel.

and 69.91% of the time respectively [27]. Vector boson fusion ($qq \to qqH$) will have at least two jets in the final state from the outgoing quarks. The estimated number of events for each production mechanism is given in table 9.8 for each mass investigated.

Eight variables are used as inputs to a neural network whose distributions are shown in figures 9.6 and 9.7 where the signal is given as a sum of the production mechanisms considered at $M_H = 160$ GeV. A neural network is trained on a sample of weighted signal and backgrounds for each mass similarly to the 0-jet and 1-jet channels. Signal and background events are then passed through the network to create templates for each mass which are then compared to the data distributions. A sample of the neural network output templates is shown in figure 9.8. Unlike the previous channels, this channel is not divided into sub-channels. For completeness

all of the neural network templates are shown in appendix A.

Roughly one third of the signal in this channel is coming from the gluon fusion process. While the cross section for this this process is known at NNLL [15], the Monte Carlo generator used for this signal (PYTHIA [61] in this case) uses a leading order calculation combined with a parton shower model. Two jets coming from $gg \rightarrow H$ is inherently a higher order process This is in some sense estimated by the parton shower model, they not included in the PYTHIA event kinematic calculations. In this channel care has been taken to both reasonably avoid using jet angle correlation information and to check that PYTHIA is estimating central quantities (such as the Higgs P_T and η) in a reasonable fashion. These studies are described further along with systematics in chapter 10.

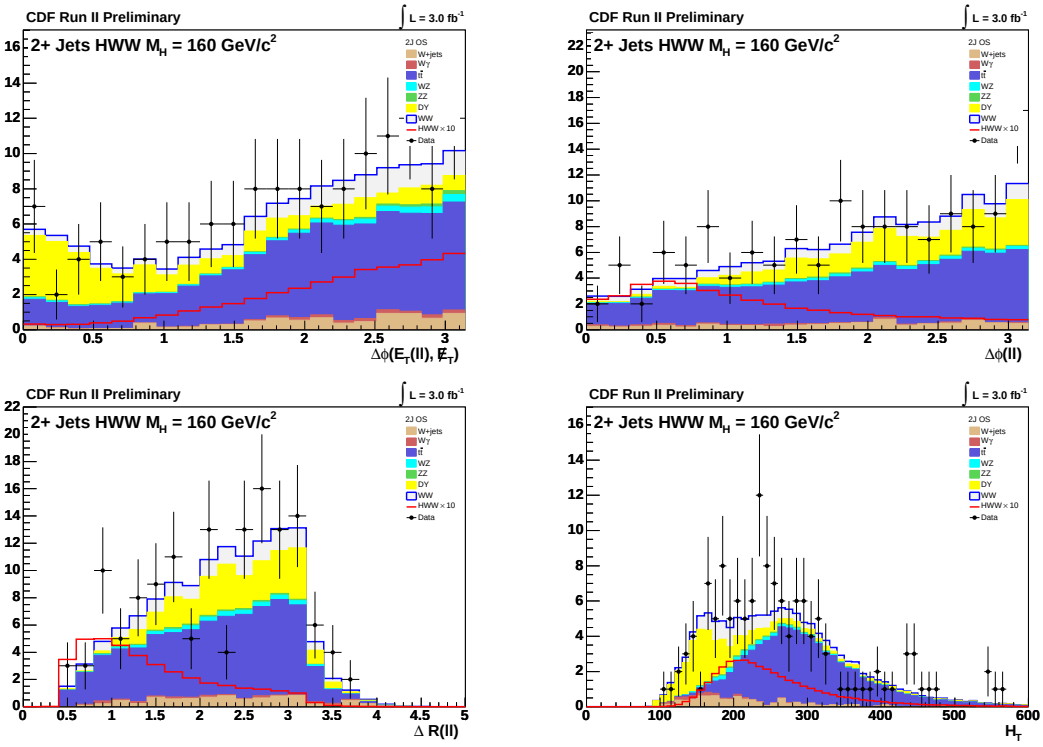

Figure 9.6: Input variables to the 2+ jet neural network.

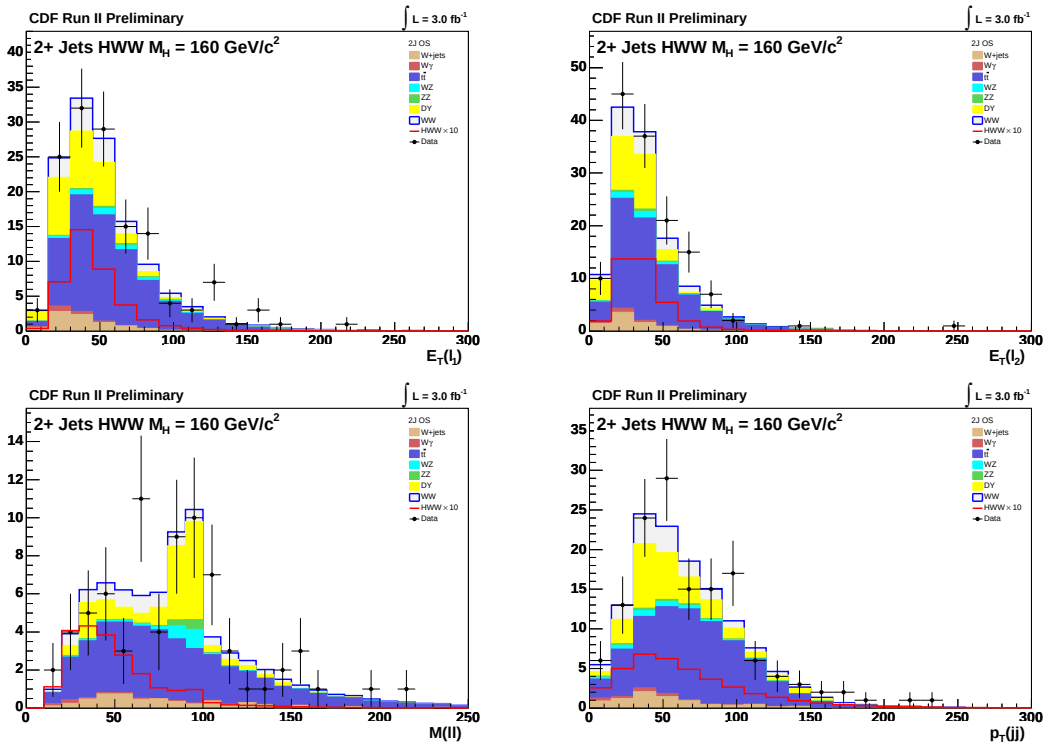

Figure 9.7: Input variables to the 2+ jet neural network.

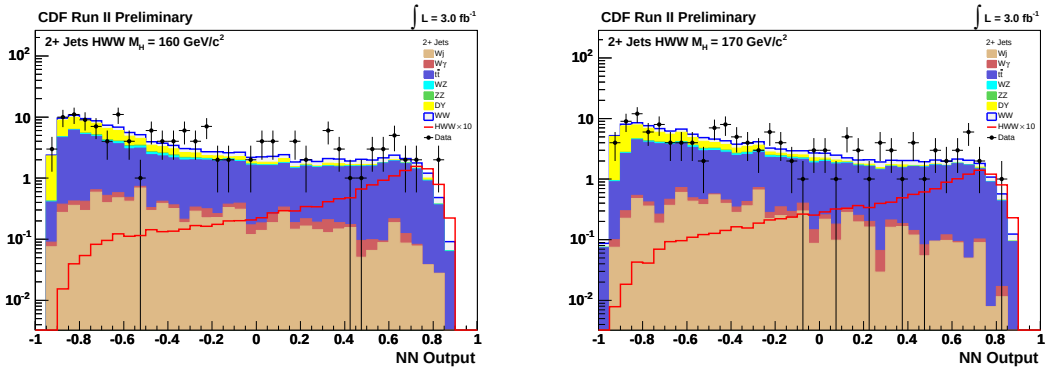

Figure 9.8: Neural network output for ≥ 2 jet events for $M_H = 160$ GeV (*left*) and $M_H = 170$ GeV (*right*).

Chapter 10

Systematic Uncertainties

Systematic uncertainties are assessed for all of the major known sources of error. Uncertainties on quantities are estimated and then propagated through to an uncertainty on the yield for each process. The uncertainties quoted in this section are all quoted as the fractional uncertainty.

There are two types of systematic uncertainties addressed in this analysis: rate uncertainties, which categorize the degree to which the yield is known with respect to a specific quantity and shape uncertainties which may effect the output, or shape of some final discriminant. Both rate and shape uncertainties are addressed and are the topic of this chapter.

10.1 Rate Systematics

Many uncertainties that effect the rate are considered. Uncertainties on fake rates, theoretical cross sections, unknown high order acceptance effects, as well as $\not\!\!E_T$ modeling and conversion modeling for Drell-Yan and $W\gamma$ respectively tend to be the larger uncertainties, though many others are considered. All rate systematics investigated in this analysis are summarized here.

Lepton ID Systematic

Process	0 Jets	1 Jet	≥ 2 Jets
WW	0.020	0.020	0.019
WZ	0.017	0.020	0.029
ZZ	0.020	0.022	0.019
$t\bar{t}$	0.020	0.018	0.019
Z/γ^*	0.019	0.020	0.019
$W\gamma$	0.014	0.020	0.019
W+jets	0.000	0.000	0.000
$gg \rightarrow H$	0.019	0.019	0.019
WH	-	0.019	0.019
ZH	-	0.019	0.019
VBF	-	0.019	0.019

Table 10.1: Fractional systematic uncertainty in each channel due to Lepton ID variations.

10.1.1 Lepton Identification

The estimate of the lepton ID uncertainty is a result of varying the lepton ID scale factors described in section 4.6 about their estimated uncertainties. The results are then compared to the nominal prediction for an estimate of the fractional uncertainty. All lepton ID scale factor are varied either all *up* or all *down* simultaneously. The yield is then calculated for each sample and compared to the nominal prediction. The fractional uncertainties due to this variation are given in table 10.1. No lepton ID uncertainty is assigned to the W+jets sample since it is derived from the data.

10.1.2 Missing Transverse Energy - $\not\!\!E_T$

For processes with real missing transverse energy this uncertainty is not very large. Drell-Yan is the most affected by $\not\!\!E_T$ modeling since the cut on $\not\!\!E_T^{spec}$ is essentially

$\not\!\!E_T$ Systematic		
Z/γ^*	Other MC	W+jets
0.200	0.010	-

Table 10.2: Fractional systematic uncertainty due to $\not\!\!E_T$ resolution. This uncertainty is applied to all channels.

cutting on a tail of a roughly exponentially falling distribution. Thus small changes in the $\not\!\!E_T^{spec}$ variable can have a large effect for this process. This uncertainty was estimated using 1.1 fb^{-1} of data by looking at the $\not\!\!E_T$ control regions and taking the largest statistical uncertainty, which in this case gives $1/\sqrt{29}$ which is rounded up to 20% [50].

The uncertainty for process with real $\not\!\!E_T$ is determined by by re-weighting the WW Monte Carlo by a data/MC factor determined from Drell-Yan events from data and MC [49]. The resulting uncertainty is less the 1%. Due to this small uncertainty, a 1% uncertainty is applied to all MC processes which contain real $\not\!\!E_T$. No uncertainty is applied to the W+jets sample since it is a data driven sample. The $\not\!\!E_T$ uncertainties are summarized in table 10.2.

10.1.3 Conversion Veto

The $W\gamma$ process will appear in the dilepton sample when the photon is falsely reconstructed as an electron. This is mostly due to photon conversions. Photon conversions are modeled in simulation however a scale factor of 1.3 is applied to the $W\gamma$ yield to compensate for modeling deficiencies. Combining the uncertainties from the conversion rate and scale factor used give a 20% uncertainty on the $W\gamma$ background [6]. This systematic is only applied to the $W\gamma$ sample.

Higher Order Acceptance Systematic						
WW	WZ	ZZ	$t\bar{t}$	Z/γ^*	$W\gamma$	W+jets
0.055	0.100	0.100	0.000	0.050	0.100	-

WH	ZH	VBF
0.100	0.100	0.100

Table 10.3: Fractional systematic uncertainty from estimates of higher order effects on the acceptance.

10.1.4 Higher Order Acceptance

Most of the Monte Carlo generators used are leading order generators. The one exception to this is WW sample which uses a NLO generator. A systematic associated with the acceptance change that may result from using a higher order calculation (which currently is not used or does not exist) is estimated. For the WW sample it is taken to be half of the acceptance difference between the leading order MC and NLO MC which is 5.5%. In this case the uncertainty would be an estimate of NNLO effects, nevertheless it serves as a guide for the rough magnitude of these effects. Estimates for this uncertainty are given in table 10.3. In this case the uncertainties in the Diboson, $t\bar{t}$, VBF, and other Higgs processes are correlated with themselves but decorrelated from each other. These systematics are not correlated across jet multiplicities.

10.1.5 PDF Uncertainties

Uncertainties from the limited knowledge of the momentum distribution of the constituent partons in the colliding protons are assessed using the 40 variations provided by CTEQ6M [59]. The effect considered here is the change in acceptance due to the PDF uncertainties. The standard CDF prescription is used where the

PDF Acceptance Systematic

WW	WZ	ZZ	$t\bar{t}$	Z/γ^*	$W\gamma$	W+jets
0.019	0.027	0.027	0.021	0.041	0.022	-

	$gg \to H$	WH	ZH	VBF
0 jet	0.015	-	-	-
1 jet	0.017	0.012	0.009	0.022
≥ 2 jet	0.020	0.012	0.009	0.022

Table 10.4: Fractional systematic uncertainties from PDF variations on the acceptance.

minimum and maximum difference in acceptance between the nominal PDFs and the variations is taken as the systematic. The formula for computing the difference is given by

$$\Delta A^+ = \sqrt{\sum_{i=1}^{20} \max(A_i^+ - A_0, A_i^- - A_0, 0)^2}$$

$$\Delta A^- = \sqrt{\sum_{i=1}^{20} \max(A_0 - A_i^+, A_0 - A_i^-, 0)^2}$$

The resulting fractional uncertainties are given in table 10.4.

The exception in table 10.4 is the $gg \to H$ acceptance uncertainty from PDFs. This uncertainty is obtained from re-weighting the Higgs η distribution to the HNNLO [38] Higgs η distribution using MRST99 [57] PDFs and varying the gluon luminosity up and down.

Other PDF uncertainties for the $gg \to H$ process are calculated in a similar way using the Higgs η and P_T distributions from HNNLO. A re-weighting of the Higgs P_T using different MRST99 gluon luminosity PDFs gives an idea of the uncertainty in jet production since the Higgs will be recoiling against these jets. This is particularly

Jet Multiplicity	η_H : μ_R, μ_F	P_T^H : μ_R, μ_F	P_T^H : g luminosity
0	0.025	+0.046	+0.009
1	0.028	−0.051	−0.019
≥ 2	0.031	−0.087	−0.028

Table 10.5: Systematic uncertainty on the $gg \rightarrow H$ acceptance due to PDF uncertainties. Distributions of η and P_T for the Higgs are re-weighted based on changing the gluon luminosity or the renormalization and factorization scales (μ_R, μ_F). The +/- refer to anti-correlated systematics across the jet multiplicities. Only the relative sign matters.

of interest because it can be anti-correlated across the different jet multiplicities.

Similarly, the renormalization and factorization scales (μ_R, μ_F) are varied and the acceptance change measured by re-weighting the nominal MC in η and P_T. The uncertainties derived from these studies for $gg \rightarrow H$ are given in table 10.5. Each of these systematics are uncorrelated with each other, but themselves correlated (or anti-correlated) across the jet multiplicities.

10.1.6 Trigger Efficiency

The uncertainty on the acceptance due to the uncertainties in the trigger efficiencies are calculated by varying the trigger efficiencies up and down by their estimated errors given in table 5.1. The systematics associated with these variations are given as fractional uncertainties on the acceptance in table 10.6.

10.1.7 Fake Probabilities

The uncertainty on the jet fake probabilities are large in comparison to other uncertainties in this analysis. The uncertainty on the fake probabilities themselves is discussed in section 4.4. The uncertainty on the yield is calculated by varying

Trigger Systematic	
Process	Fractional uncertainty
WW	0.021
WZ	0.021
ZZ	0.021
$t\bar{t}$	0.020
Z/γ^*	0.034
$W\gamma$	0.070
W+jets	-
$gg \rightarrow H$	0.033
WH	0.021
ZH	0.021
VBF	0.033

Table 10.6: Fractional uncertainty on the acceptance in each channel due to trigger efficiency variations.

Fake Probability Systematic				
High S/B 0J	Low S/B 0J	High S/B 1J	Low S/B 1J	≥ 2 Jets
0.277	0.215	0.315	0.222	0.271

Table 10.7: Systematic due to the jet fake probability uncertainties for each channel.

the probability up and down by its estimated statistical and systematic error and measuring the change in the yield. This uncertainty only applies to the W+jets sample which is itself taken from the data. The fractional uncertainties on the yield are given in table 10.7.

10.1.8 Monte Carlo Run Dependence

The data periods used in this analysis are 0 through and including 17. The simulation is run dependent, however not all of the Monte Carlo samples are simulated for the full run range. As a result of this a systematic is taken to account for any

Monte Carlo Run Dependence Systematic

Process	0 Jet	1 Jet	≥ 2 Jets
WW	0.039	0.018	0.010
$t\bar{t}$	0.045	0.022	0.010
$W\gamma$	0.045	0.022	0.010
$gg \rightarrow H$	0.037	0.026	0.017
WH	-	0.026	0.020
ZH	-	0.019	0.019
VBF	-	0.028	0.026

Table 10.8: Fractional systematic uncertainty due to run dependent Monte Carlo.

run dependent deficiencies. The WW sample used in this analysis is a NLO Monte Carlo sample which only covers periods 0 through and including 7. A PYTHIA [61] sample spanning the entire run range is processed twice to give samples for the run periods p0-7 and p0-17, which allows one to measure directly the run dependent change in acceptance. Since the WW sample is scaled to match this change only half of the difference is taken as a systematic. The deficiency in run range for the other samples is estimated using the Drell-Yan Monte Carlo sample. This run dependence systematic is also estimated for the different jet multiplicities considered. This uncertainty is correlated across all samples and jet multiplicities. The fractional uncertainties are given in table 10.8.

10.1.9 Luminosity and Anti-B-Tag

For all Monte Carlo based samples a systematic is applied for the uncertainty in the CDF luminosity measurement of 5.9% which is correlated across all samples and channels. This does not apply to the W+jets sample since it is directly from the data.

Higher Order Acceptance Systematic						
WW	WZ	ZZ	$t\bar{t}$	Z/γ^*	$W\gamma$	W+jets
0.100	0.100	0.100	0.150	0.050	0.100	-

$gg \to H$	WH	ZH	VBF
0.120	0.050	0.050	0.100

Table 10.9: Fractional systematic uncertainty from theory cross section uncertainties.

The uncertainty on the efficiency of the b-tagging algorithm is 5% [28]. Inverting this by requiring that there be no b-tag on events from the $t\bar{t}$ sample yields an uncertainty of 7%. This uncertainty is applied only to the $t\bar{t}$ sample and only in the ≥ 2 jets channel where events with b-tagged jets are rejected.

10.1.10 Cross Section

Theoretical uncertainties on the cross sections are also taken as systematic uncertainties. These uncertainties are listed in table 10.9. The WW, WZ, and ZZ cross section uncertainties are taken to be correlated while the others are uncorrelated in the likelihood. No systematic is taken on the W+jets since it is derived from the data.

10.2 Shape Systematics

Several shape systematics were investigated which were thought to have the largest effect. None of the shape systematics investigated showed any deviation in the final result which was outside of the statistical uncertainty in the limits. As a result no shape systematics are used in the final result. The are summarized here for

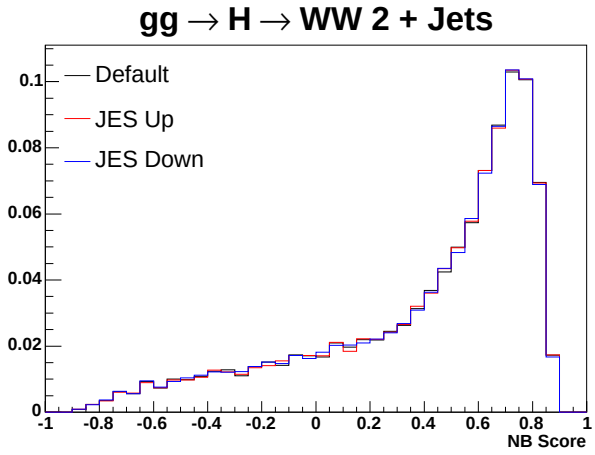

Figure 10.1: Neural network output for the $gg \rightarrow H$ signal in the ≥ 2 jets channel with different jet energy scale variations for $M_H = 160$ GeV.

completeness

10.2.1 Jet Energy Scale

The effect of the jet energy scale is investigated as a shape uncertainty in the neural network output for the ≥ 2 jets channel. The jet energy corrections which are standard at CDF [26] are varied up and down corresponding to their $\pm 1\sigma$ uncertainties. These variations are typically on the order of 2-3%. Variations of the jet energy scale for $gg \rightarrow H$ signal events is shown in figure 10.1. There is only a very slight shape variation and when computing limits with these variations given as $\pm 1\sigma$ shape errors there is no noticeable difference in the final result.

10.2.2 Initial State Radiation - WW / $H \rightarrow WW$

Variations of the initial state radiation (ISR) tuning in PYTHIA were investigated to get an idea of the magnitude of the shape variations in the neural network output

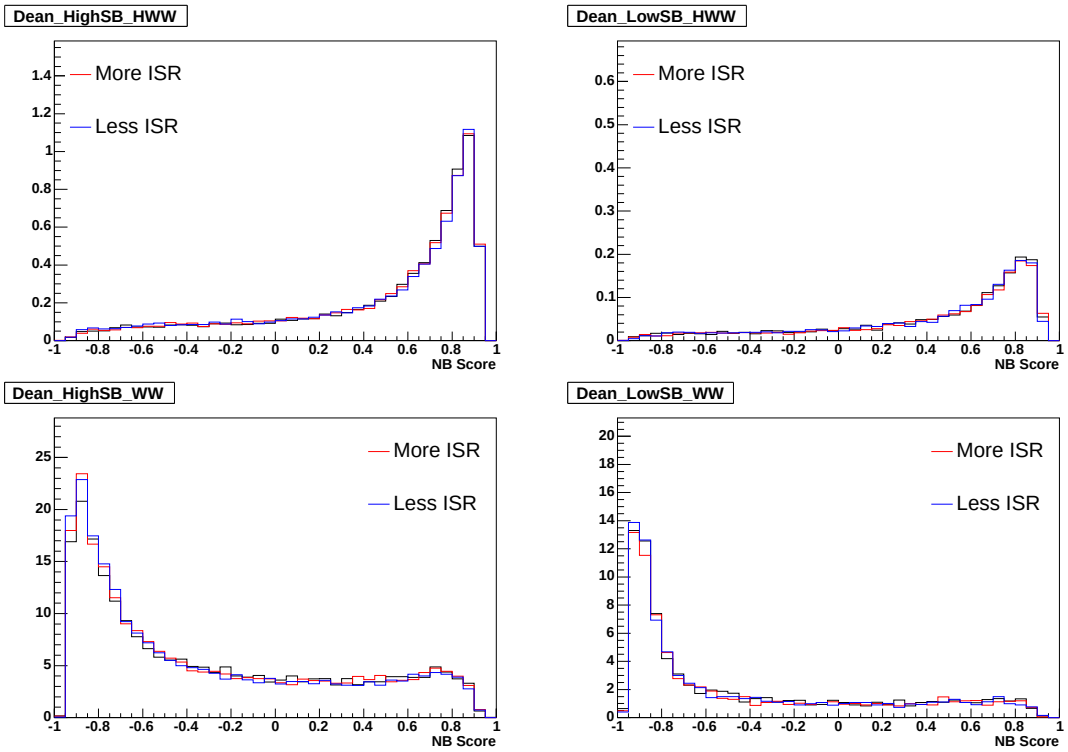

Figure 10.2: Neural network output for the $gg \rightarrow H$ signal (*top*) and WW background (*bottom*) for 0 and 1 jet events with different PYTHIA ISR tunings at $M_H = 160$ GeV. High S/B is shown on the left and low S/B on the right. The default is given in black.

for 0 and 1 jet events. The variations for the $gg \rightarrow H$ and WW PYTHIA sample are shown for high and low S/B in figure 10.2. There is again no appreciable difference in the final results due to this shape difference and they are in the end not included in the final result.

10.2.3 Scale Variations - μ_R and μ_F

HNNLO was used to study scale variations for the $gg \rightarrow H$ signal in the ≥ 2 jets channel. μ_R and μ_F are varied between $M_H/4$ and M_H, where the default

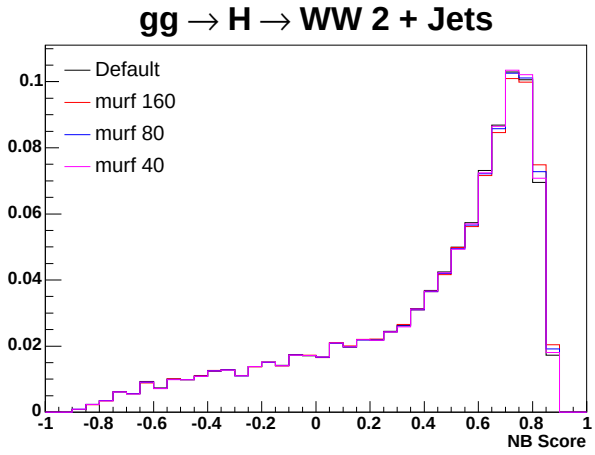

Figure 10.3: Neural network output for the $gg \rightarrow H$ signal in the ≥ 2 jets channel for different variations of the renormalization and factorization scale for $M_H = 160$ GeV.

value is $M_H/2$. The PYTHIA sample is then re-weighted to match the HNNLO distributions, which gives the shape variations shown in figure 10.3 for $M_H = 160$ GeV. This shape difference has no effect on the limits and is not included in the final result.

Chapter 11

Setting Limits on Standard Model Higgs Production

As can be seen from the estimates and observed events shown in chapter 9 there is no obvious nor appreciable excess of data events. It is thus desirable to quote an allowed upper limit on the possible contribution from the signal to the data at some confidence level. The method and results from data are discussed in the remainder of this chapter.

11.1 A Bayesian Method

In this analysis a Bayesian method is used to set an upper limit on SM Higgs production for 14 values of M_H, which in this case includes contributions from $gg \to H$, WH, ZH, and VFB.

Bayes' theorem, given by

$$P(A|B) = \frac{P(A)}{P(B)} P(B|A) \tag{11.1}$$

says that the probability of observing an outcome A given that an outcome B

has already occurred is equal to the probability of observing B given that A has occurred times the ratio of the probabilities of A and B. The essential idea is that one wishes to make inferences about the unknown true value (A_T) from $P(A_T|B_0)$ given the results of an experiment which observes B_0, whose probability distribution is correlated with A. A likelihood ($\mathcal{L}$) is used to make inferences about the observation B_0 given a true value (A_T) and is applied to Bayes' theorem as

$$P(A_T|B_0) = \mathcal{L}(B_0|A_T)\frac{P(A_T)}{P(B_0)}. \tag{11.2}$$

The intention is to investigate confidence intervals by integrating the *p.d.f.* $P(A_T|B_0)$ over a range of possible true values (A_T) as in

$$\int_{A_1}^{A_2} P(A_T|B_0)\, dA_T = \int_{A_1}^{A_2} \mathcal{L}(B_0|A_T)\frac{P(A_T)}{P(B_0)}\, dA_T = \alpha. \tag{11.3}$$

Here α is called the confidence level. The denominator in equation 11.2, $P(B_0)$, essentially becomes a normalization factor. $P(A_T)$ is the *prior* and it may contain constraints, or prior beliefs, about the true value of the parameter A_T.

In this analysis a binned likelihood is used where the likelihood is given by a product of Poisson probabilities

$$\mathcal{L} = \prod_i \frac{\mu_i^{n_i} e^{-\mu_i}}{n_i!} \tag{11.4}$$

where μ_i is the total prediction in the i-th bin and n_i the number observed events

in that bin. The expected total in the i-th bin is given by

$$\mu_i = \sum_k \left[\prod_c (1 + f_k^c S_c) \right] \mu_i^k \tag{11.5}$$

where k refers to the processes considered and c the systematic uncertainties. f_k^c is the fractional uncertainty for the k-th process due to the systematic c. S_c are nuisance parameters for each systematic considered. Typically when setting limits variations of these nuisance parameters are integrated, or averaged, over to obtain a reasonably smooth likelihood distribution as a function of A_T.

The prior used in this analysis is flat in the ratio of the Higgs cross section being tested to the standard model prediction and acceptance combined with efficiencies. This is to say that the acceptance, efficiencies, and cross section are given equal weight for any value of the Higgs cross section in question. Non-physical values of the Higgs cross section are not considered, thus the value A_1 in equation 11.3 is not allowed to be negative.

11.2 Computing Upper Limits

Upper limits for Higgs cross sections are calculated as a ratio to the SM and include contributions from the four production processes mentioned previously. The SM cross sections for the individual processes are given in table 2.7. The limit is calculated for the ratio of total event yields and interpreted as a limit on the production compared to the SM prediction.

The confidence level chosen is 95%, or $\approx 2\sigma$ as given by the normal distribution.

The choice of 95% is somewhat flexible, but is both seemingly reasonable and has become standard practice in high energy physics for setting limits.

To normalize the integral in equation 11.3 the denominator is chosen to be

$$P(B_0) = \int_0^\infty \mathcal{L}(B_0|A_T)dA_T. \tag{11.6}$$

It is then easy to interpret α as the confidence level that the true value lies between A_1 and A_2. Computationally, the integral in equation 11.6 can be difficult and if not done correctly may not converge. A Gauss-Laguerre integration technique is used in this analysis which is further described in [46].

In this case, since an upper limit is desired, $A_1 = 0$ and A_2 is determined by choosing the desired value of α. Where $\alpha = 0.95$ the integral becomes

$$\frac{\int_0^{A_2} \mathcal{L}(B_0|A_T)dA_T}{\int_0^\infty \mathcal{L}(B_0|A_T)dA_T} = 0.95. \tag{11.7}$$

A_2 is then the upper limit at the 95% confidence level.

This upper limit, A_2, is determined numerically using a software package developed at CDF called mclimit [53]. This software has the ability to combine many channels, integrate the nuisance parameters, use asymmetric errors, and interpolate between shape error variations. Systematics, including shape systematics, are discussed further in chapter 10. The shape systematics considered had an insignificant effect on the result and are not included in the final result. Symmetric rate errors are applied for each systematic considered.

11.3 Upper Limits on Higgs Production by Channel

Upper limits are calculated on SM Higgs production as a ratio to the SM prediction for 14 masses in the range $110 \leq M_H \leq 200$ GeV. The limits are calculated for the 0 and 1 jet channels combined and the ≥ 2 jet channel separately which are discussed in the following sections. The combination of all channels is given in section 11.4. In combining multiple channels which involve different production mechanisms the cross section uncertainties on the different production mechanisms are taken into account.

For each combination of channels 10,000 pseudo-experiments are generated and limits computed for each. Pseudo-experiments are generated by varying the mean prediction for each process in a correlated way across all channels based on their systematic uncertainties. This prediction is then Poisson fluctuated to obtain the contribution from each process. This number of events is then selected from its template according to the probability distribution of the template. Statistical errors on the templates, though small due to the large statistics, are assumed to be Gaussian. For the pseudo-experiments, 1,000 iterations over the nuisance parameters are performed. For the data limit the number of iterations is increased to 10,000 for more robust data limits. These pseudo-experiments give an idea of the range of limits one should expect to find in experiment. All optimizations of the analysis are based on the median expected limit and the distribution of limits from pseudo-experiments.

The templates used to calculate these limits are the neural network templates

discussed in sections 9.1, 9.2 and 9.3. All of the templates used for each mass can be found in appendix A.

11.3.1 Limits for Zero and One Jet Channels

Limits are calculated for the combination of the 0 and 1 jet channels. This includes a total of 4 sub-channels (High and Low S/B for each, discussed at the beginning of chapter 9) which are individually incorporated into the limit. To incorporate them, the product over i in the likelihood of equation 11.4 is extended to cover all of the bins in each channel.

The limits for the combined 0 and 1 jet channels are shown in figure 11.1. At a Higgs mass of 165 GeV the expected limit is $1.88 \times \sigma_{SM}$ and the observed limit is $1.63 \times \sigma_{SM}$.

11.3.2 Limits for the ≥ 2 Jet Channel

Limits for the ≥ 2 jet channel are calculated similarly to the zero and one jet channel. The main difference is that here there is only one channel and no distinction is made between high and low S/B events. It is interesting to separate this channel from the others in the sense that the background composition is somewhat different and the signal is comparable between $gg \rightarrow H$, VH, and VBF as can be seen in table 9.8.

This channel alone gives an upper limit on SM Higgs production of $4.39 \times \sigma_{SM}$ expected and $6.55 \times \sigma_{SM}$ observed at $M_H = 165$ GeV. The limits at all of the masses investigated are shown in figure 11.2. An overall excess of events in this channel pushes the observed limit just above 1σ high, however this excess is still well within

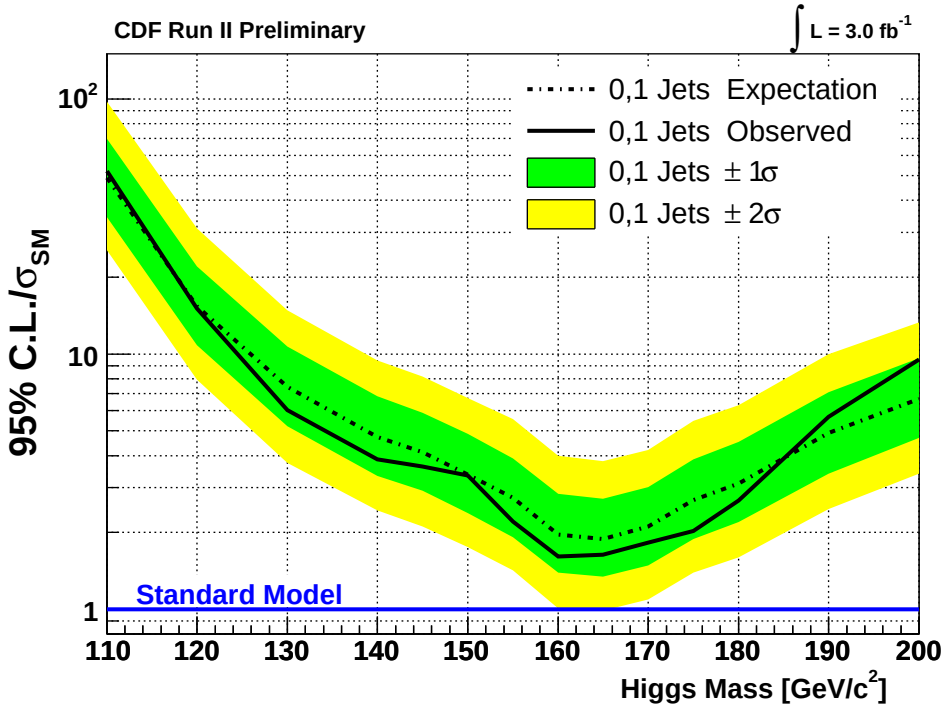

	110	120	130	140	145	150	155
$-2\sigma/\sigma_{SM}$	25.49	7.93	3.75	2.44	2.11	1.75	1.42
$-1\sigma/\sigma_{SM}$	34.36	10.84	5.21	3.33	2.91	2.38	1.91
Median/σ_{SM}	**49.02**	**15.39**	**7.44**	**4.72**	**4.12**	**3.37**	**2.73**
$+1\sigma/\sigma_{SM}$	69.77	22.02	10.69	6.83	5.89	4.86	3.90
$+2\sigma/\sigma_{SM}$	97.30	31.11	14.82	9.44	8.16	6.72	5.56
Observed/σ_{SM}	**52.10**	**15.11**	**6.03**	**3.86**	**3.62**	**3.35**	**2.20**

	160	165	170	175	180	190	200
$-2\sigma/\sigma_{SM}$	1.01	0.99	1.09	1.39	1.60	2.47	3.40
$-1\sigma/\sigma_{SM}$	1.39	1.34	1.48	1.88	2.19	3.40	4.68
Median/σ_{SM}	**1.96**	**1.88**	**2.11**	**2.67**	**3.11**	**4.91**	**6.67**
$+1\sigma/\sigma_{SM}$	2.83	2.71	3.02	3.87	4.52	7.10	9.65
$+2\sigma/\sigma_{SM}$	4.00	3.81	4.20	5.47	6.30	9.98	13.31
Observed/σ_{SM}	**1.61**	**1.63**	**1.82**	**2.03**	**2.66**	**5.68**	**9.51**

Figure 11.1: Expected and observed limits on Higgs production as a ratio to the standard model expectation for 0 and 1 jet channels combined.

the estimated uncertainties as can be seen in table 9.7.

11.4 Limits Combined

Templates from all sub-channels are combined into what is the final result. The limits on Higgs production shown in this section consist of a total of five sub-channels. This combined result is currently the world's most sensitive single-experiment limit on SM Higgs production. Systematics for this combination are estimated separately for each channel, however the correlations between channels are taken into account where appropriate.

The combination gives an upper limit on SM Higgs production at $1.70 \times \sigma_{SM}$ with an expected limit of $1.70 \times \sigma_{SM}$ at $M_H = 165$ GeV. The 95% C.L. upper limit for each of the 14 masses investigated is given in figure 11.3.

This limit, combined with an analysis from the D0 collaboration [23], became the first result from a hadron collider to exclude a standard model Higgs at the 95% confidence level. These experiments together exclude at 95% C.L. a standard model Higgs in a narrow range around $M_H = 170$ GeV [21].

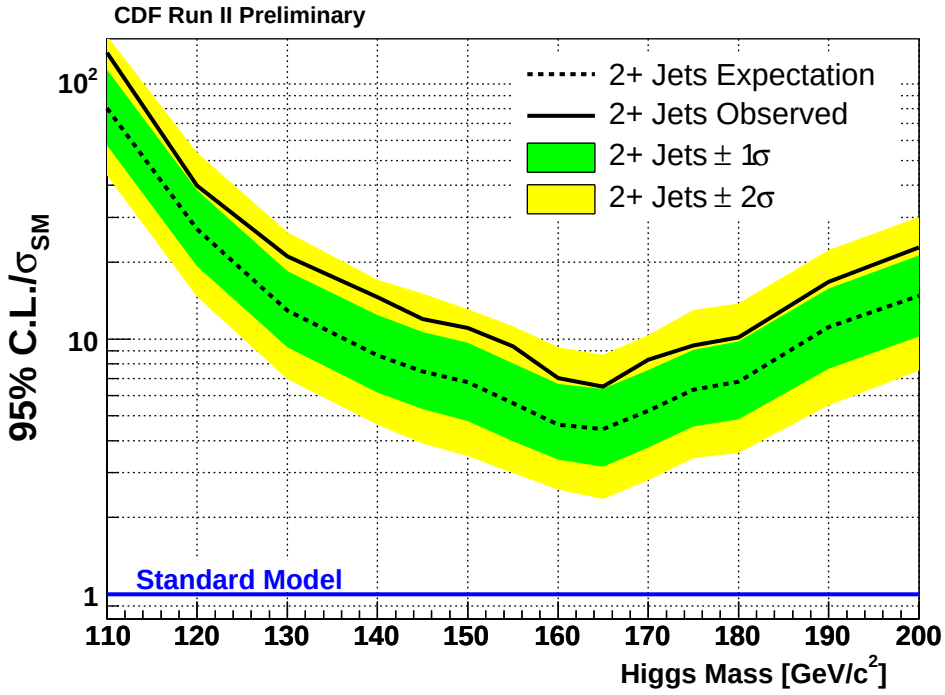

	110	120	130	140	145	150	155
$-2\sigma/\sigma_{SM}$	42.02	14.26	6.81	4.40	3.77	3.43	2.85
$-1\sigma/\sigma_{SM}$	56.39	18.92	9.19	6.02	5.18	4.64	3.89
Median/σ_{SM}	**79.35**	**26.55**	**12.98**	**8.53**	**7.38**	**6.66**	**5.51**
$+1\sigma/\sigma_{SM}$	112.98	38.17	18.67	12.36	10.76	9.53	7.96
$+2\sigma/\sigma_{SM}$	157.79	53.54	26.40	17.30	15.16	13.47	11.26
Observed/σ_{SM}	**131.94**	**39.79**	**21.01**	**14.57**	**11.76**	**10.77**	**9.14**

	160	165	170	175	180	190	200
$-2\sigma/\sigma_{SM}$	2.37	2.28	2.65	3.22	3.50	5.73	7.43
$-1\sigma/\sigma_{SM}$	3.19	3.10	3.63	4.41	4.85	7.84	10.34
Median/σ_{SM}	**4.51**	**4.39**	**5.15**	**6.29**	**6.89**	**11.37**	**14.90**
$+1\sigma/\sigma_{SM}$	6.48	6.35	7.49	9.20	10.03	16.45	21.61
$+2\sigma/\sigma_{SM}$	9.12	8.89	10.57	13.01	14.17	23.46	30.82
Observed/σ_{SM}	**6.89**	**6.55**	**8.12**	**9.40**	**10.17**	**17.39**	**23.07**

Figure 11.2: Expected and observed limits on Higgs production as a ratio to the standard model expectation for the ≥ 2 jet channels.

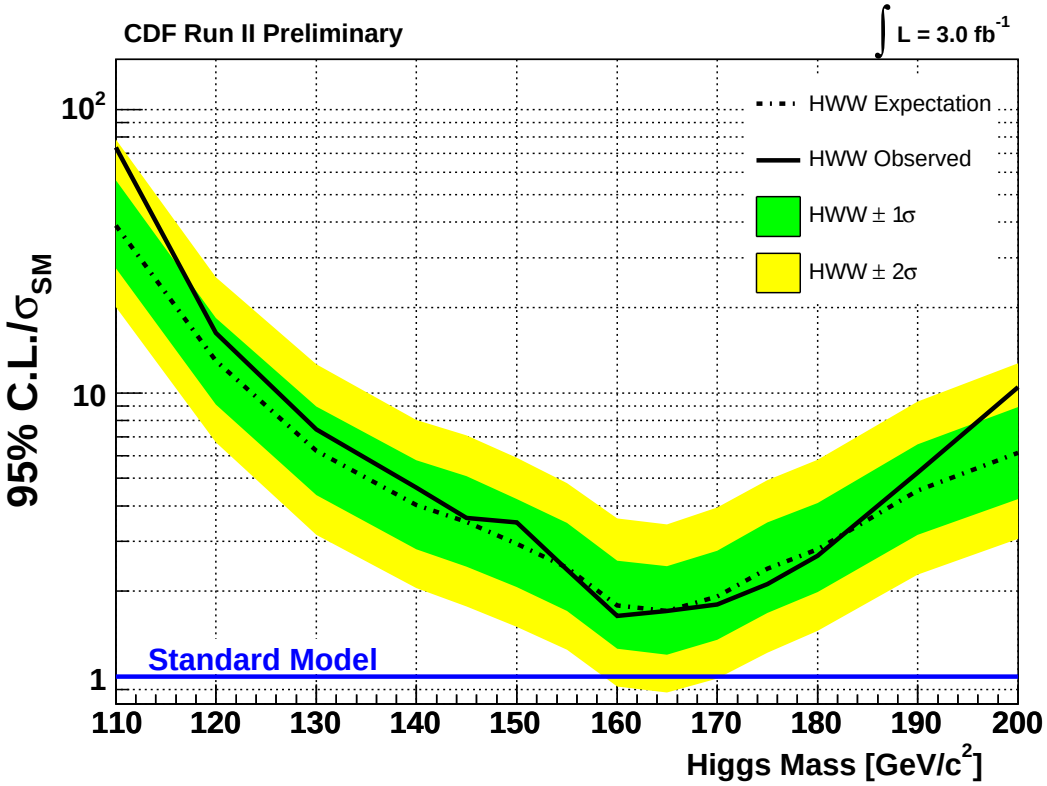

	110	120	130	140	145	150	155
$-2\sigma/\sigma_{SM}$	20.11	6.69	3.16	2.05	1.76	1.50	1.24
$-1\sigma/\sigma_{SM}$	27.48	9.10	4.37	2.81	2.44	2.07	1.70
Median/σ_{SM}	**38.90**	**12.96**	**6.26**	**4.02**	**3.51**	**2.94**	**2.42**
$+1\sigma/\sigma_{SM}$	56.22	18.41	8.96	5.79	5.09	4.23	3.48
$+2\sigma/\sigma_{SM}$	78.34	25.57	12.63	8.04	7.08	5.91	4.82
Observed/σ_{SM}	**73.37**	**16.30**	**7.43**	**4.63**	**3.62**	**3.49**	**2.38**

	160	165	170	175	180	190	200
$-2\sigma/\sigma_{SM}$	0.92	0.88	0.98	1.21	1.45	2.29	3.06
$-1\sigma/\sigma_{SM}$	1.25	1.20	1.35	1.67	1.99	3.16	4.23
Median/σ_{SM}	**1.78**	**1.70**	**1.92**	**2.40**	**2.81**	**4.52**	**6.14**
$+1\sigma/\sigma_{SM}$	2.56	2.45	2.77	3.49	4.10	6.58	8.92
$+2\sigma/\sigma_{SM}$	3.61	3.44	3.95	4.93	5.81	9.32	12.73
Observed/σ_{SM}	**1.63**	**1.70**	**1.79**	**2.12**	**2.67**	**5.23**	**10.49**

Figure 11.3: Expected and observed limits on Higgs production as a ratio to the standard model expectation for all channels combined.

Chapter 12

Conclusions

An upper limit is set on standard model Higgs production for 14 Higgs masses in the range $110 \leq M_H \leq 200$ using the $H \rightarrow WW$ decay mode. The final state considered consists of two identified leptons (e or μ) and missing transverse energy. Four Higgs production mechanisms are considered which gives a total expected signal yield of 17.5 ± 2.2 events for a Higgs mass of 160 GeV on top of an expected background of 894.8 ± 97.6 events in 3 fb^{-1} of data. The number of events observed in data is 918. Advanced statistical techniques (matrix element based event probabilities and neural networks) are used to further separate signal from background. The use of these advanced techniques as well as the addition of three production mechanisms which were not previously considered have considerably increased the sensitivity from previous measurements.

The most important background in this analysis is WW production, specifically for events containing zero and one jets. Top quark pair production is the dominant background for events containing two or more jets. Both of these cross sections are measured in this analysis and agree well with the SM prediction giving confidence in the background estimations which is crucial in searching for yet unobserved phenomena.

The upper limit from this analysis on the SM Higgs cross section is $1.63 \times \sigma_{SM}$ for $M_H = 160$ GeV at 95% confidence. This analysis combined with an analysis from DØ excludes a SM Higgs in a narrow range around $M_H = 170$ GeV at 95% confidence which is the first such exclusion from a hadron collider.

Whether the Higgs exists as prescribed by the standard model, or by some other model, or by no model, or does not exist at all, is still a looming question in particle physics, the answer to which is of great current interest. It can now be said that it does not exists at $M_H = 170$ GeV with reasonable confidence, but whether or not the mechanism of electroweak symmetry breaking is that given by the Higgs mechanism is still uncertain. Whatever the mechanism, there must be some underlying principle which explains the mass hierarchy of the particles observed in nature.

Chapter 13

Brief Notes on Future Work

There are several improvements to this analysis at CDF which can and may be implemented in the near future. One of these is the obvious inclusion of the third generation lepton, the τ. The analysis is already sensitive to the leptonic decay of the τ, however this is a relatively small fraction of all τ decays. 64.8% of the time a τ will decay hadronically (denoted by τ_{had}) [27]. While the combinatorics of adding the third lepton type are a clear benefit one must realize the difficulty in both identifying these τ_{had} decays and the even more difficult task estimating the amount of fake τ_{had} coming from QCD jets, which is large and difficult to reduce.

In the case of a Higgs produced in association with a vector boson VH the final state may contain leptons of like charge. For instance the decays

$$W^{\pm}H \rightarrow W^{\pm}W^{+}W^{-} \rightarrow \begin{cases} \ell^{\pm}\nu\ell^{+}\nu jj \\ \ell^{\pm}\nu jj\ell^{-}\bar{\nu} \\ \ell^{\pm}\nu\ell^{+}\nu\ell^{-}\bar{\nu} \end{cases}$$

as well as $ZH \rightarrow ZW^{+}W^{-}$ where the Z and either W decay leptonically. The main standard model background for this is WZ production along with W+jets and $W\gamma$

where the jet or photon fakes a lepton. In general, the backgrounds for this search are quite small. To reduce the fake contributions from W+jets and $W\gamma$ forward tracks and forward electrons can be removed. Initial studies of same sign events (two or three leptons only) show a sensitivity of about $9.6 \times \sigma_{SM}$ at $M_H = 160$ GeV which is roughly 2 times the ≥ 2 jet channel limit. This avenue is one clearly worth pursuing. Care must be taken in estimating the fake contributions and in measuring how often the wrong charge is assigned to tracks which may enter the signal sample. This rate is in general very small for central tracks.

Some benefit may come from using the forward muon detectors (which are not described in this thesis) to purify the CMIO categories. One should take care that the acceptance loss from their inclusion does not negatively effect the sensitivity beyond what is reasonable.

Although the branching ratio is smaller, the $H \rightarrow ZZ$ mode should add some sensitivity even at the Tevatron. To first order one can include the $H \rightarrow ZZ \rightarrow \nu\bar{\nu}\ell^+\ell^-$ mode where one might expect to see some signal in the already defined "base region". The $\not\!\!E_T$ from the neutrinos will tend to be less than for that of the $H \rightarrow WW$ decay. For this reason it may be difficult to recover some of these events which may get lost under a mountain of Drell-Yan. Matrix element calculations or a neural network may aide in separating these events from Drell-Yan if one were to lower the $\not\!\!E_T$ requirement. The 4 lepton mode, or the "golden mode" at the LHC, has a very small cross section times branching ratio at the Tevatron, though the backgrounds are quite small. The other modes involving leptons and jets in the final state with no real $\not\!\!E_T$ are difficult to distinguish from large backgrounds.

By the end of Run II, Tevatron experiments should have the sensitivity to ex-

clude a moderate range of Higgs masses around 165 GeV using the $H \rightarrow WW$ mode. It should be noted as well that this mode has about the same sensitivity as the low mass searches (using WH and ZH where $H \rightarrow b\bar{b}$ is the dominant decay) at $M_H = 130$ GeV so it is not only very powerful at high masses, but contributes significantly at lower masses than one might expect. This channel is also of great interest at the LHC where the discovery potential in this mass range is clear.

Appendix A

Neural Network Templates

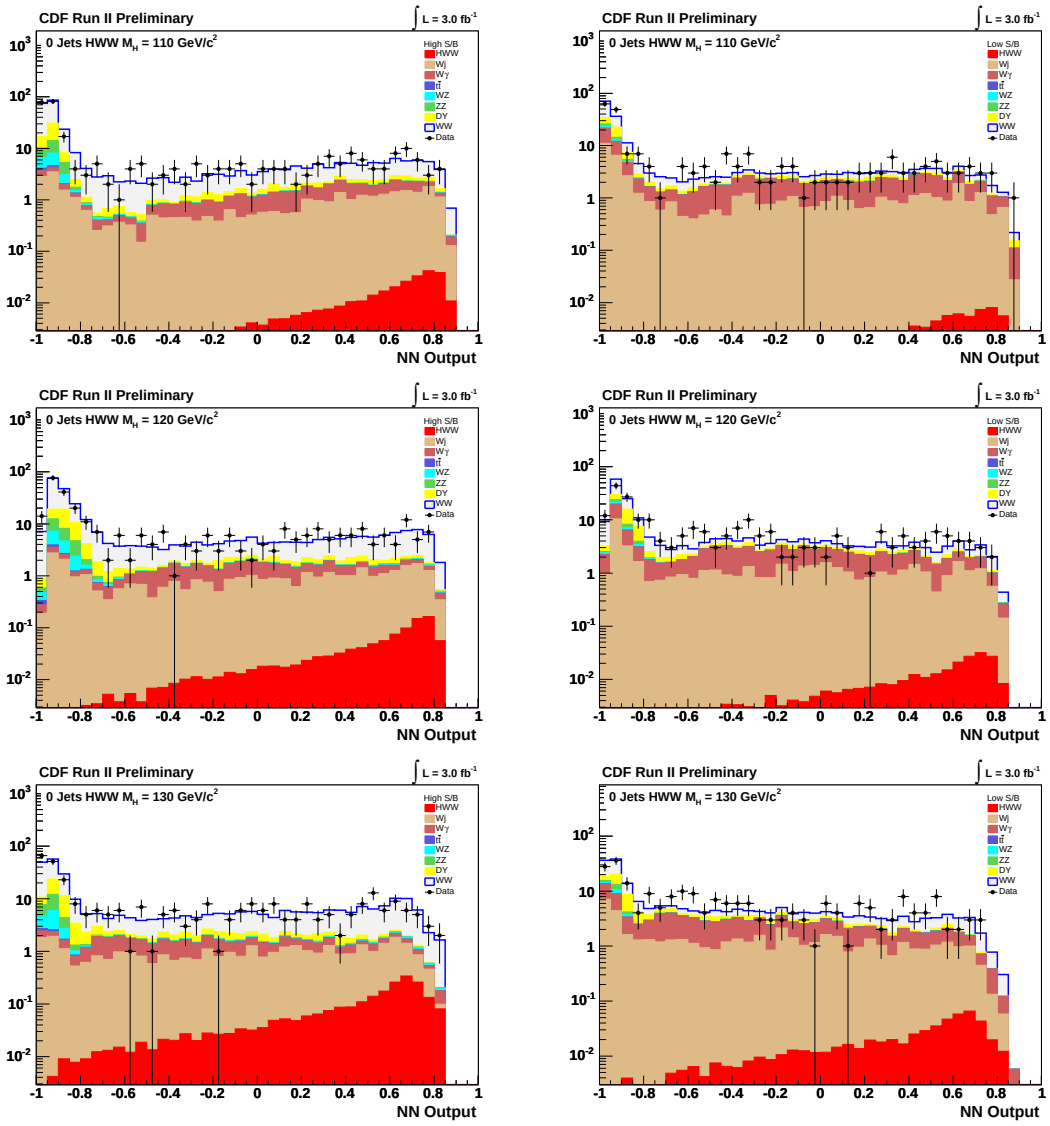

Figure A.1: Neural network output for high S/B (*left*) and low S/B (*right*) 0-jet events for $110 \leq M_H \leq 143$ GeV.

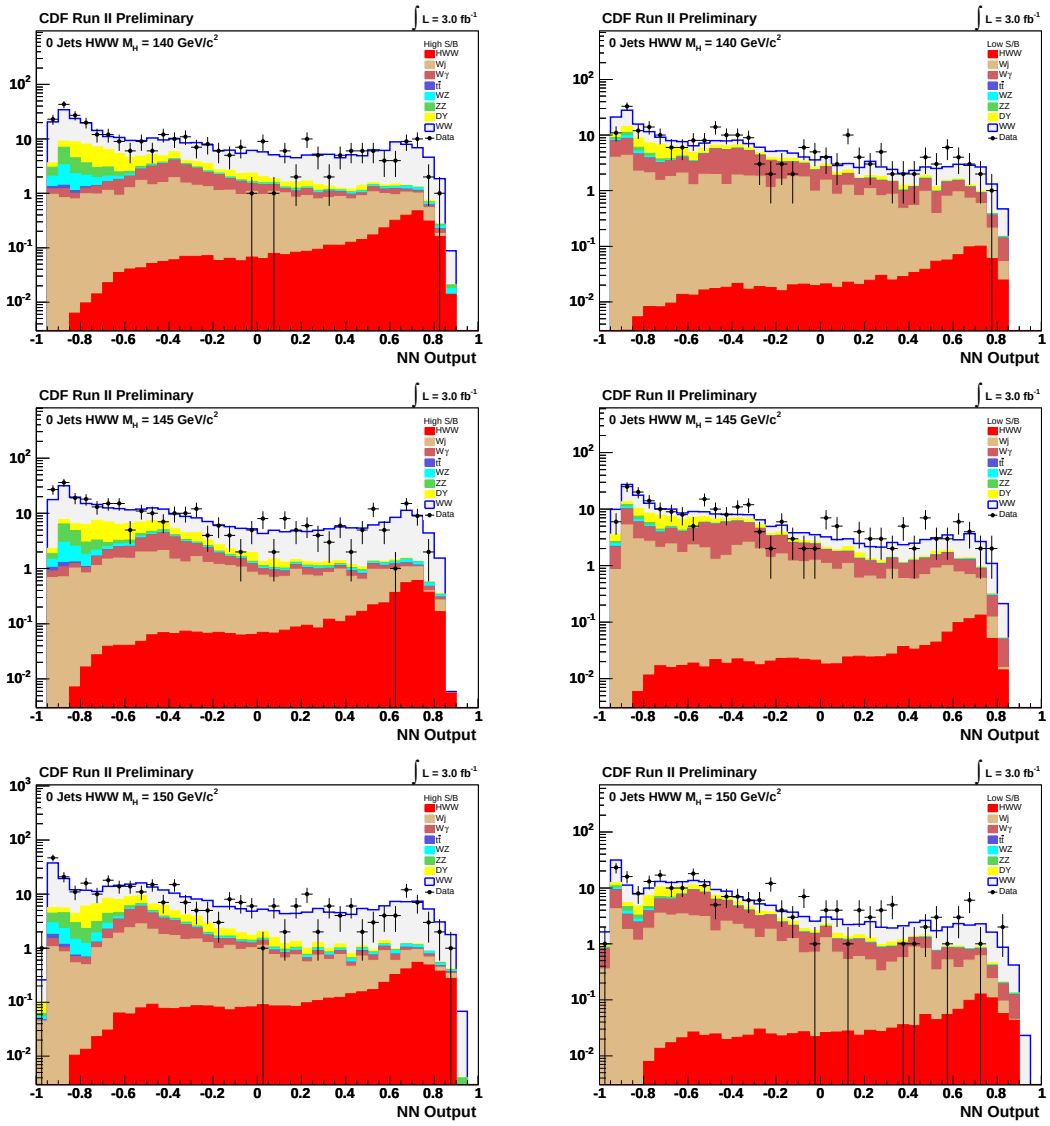

Figure A.2: Neural network output for high S/B (*left*) and low S/B (*right*) 0-jet events for $135 \leq M_H \leq 150$ GeV.

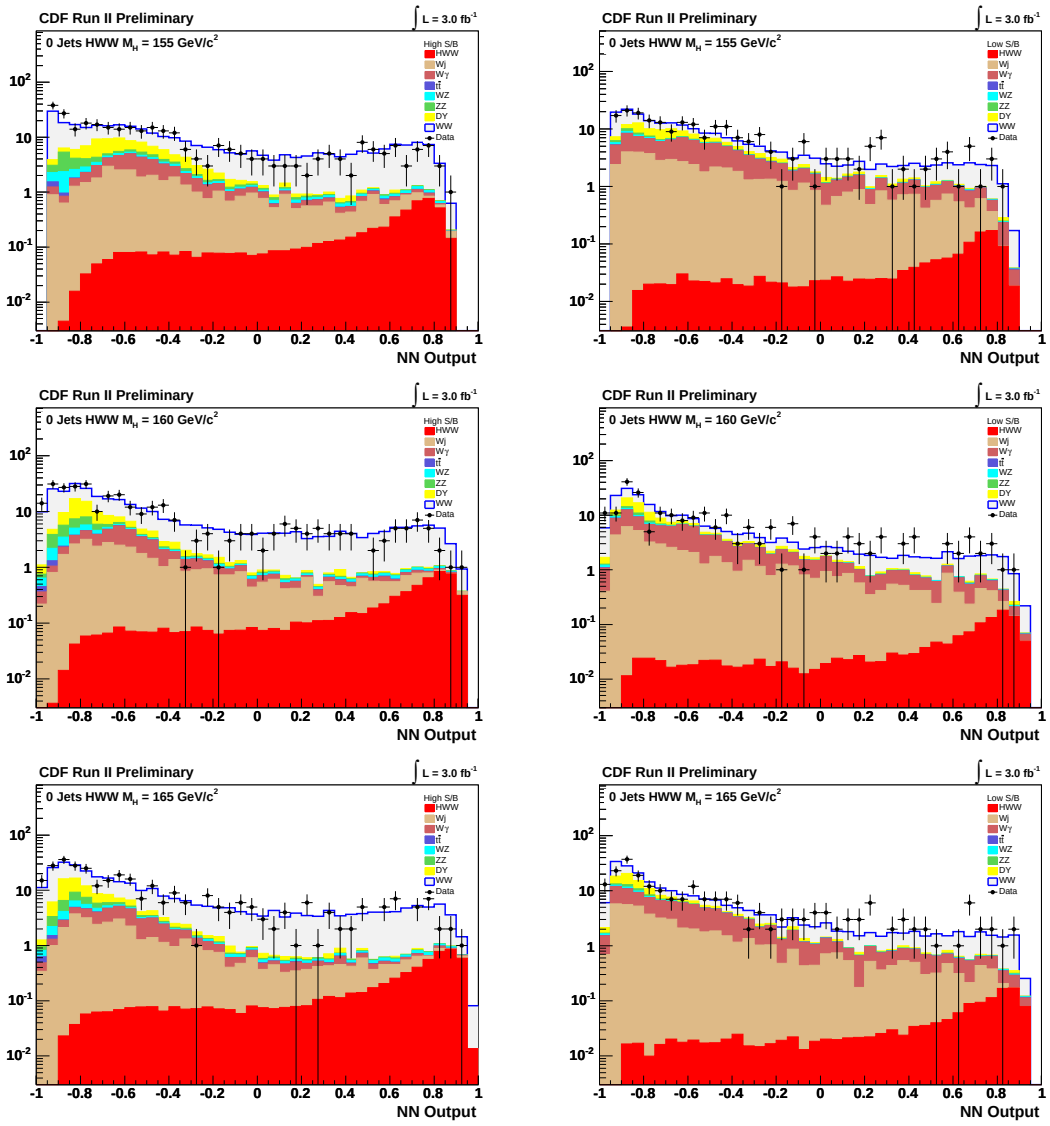

Figure A.3: Neural network output for high S/B (*left*) and low S/B (*right*) 0-jet events for $155 \leq M_H \leq 165$ GeV.

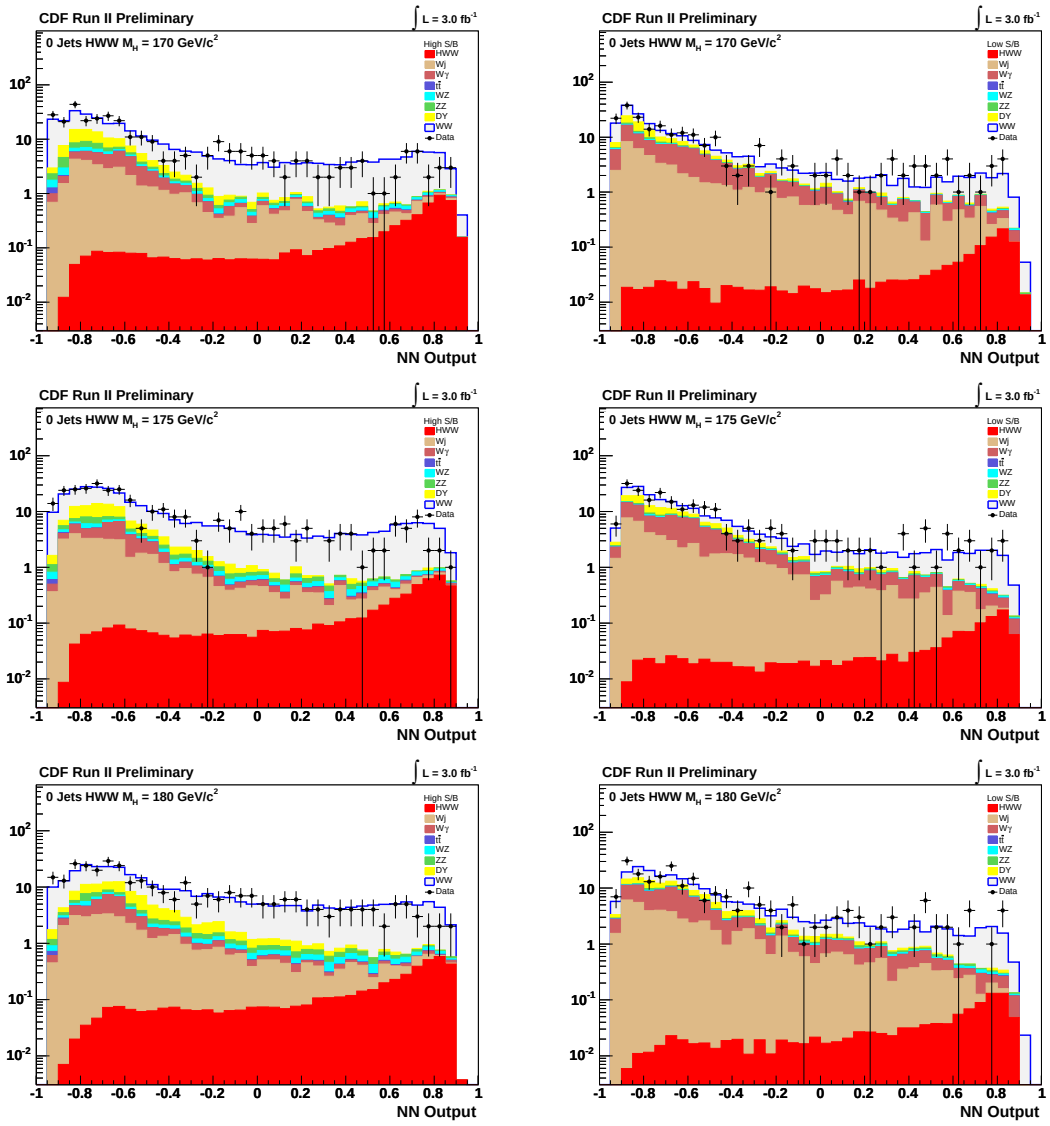

Figure A.4: Neural network output for high S/B (*left*) and low S/B (*right*) 0-jet events for $170 \leq M_H \leq 180$ GeV.

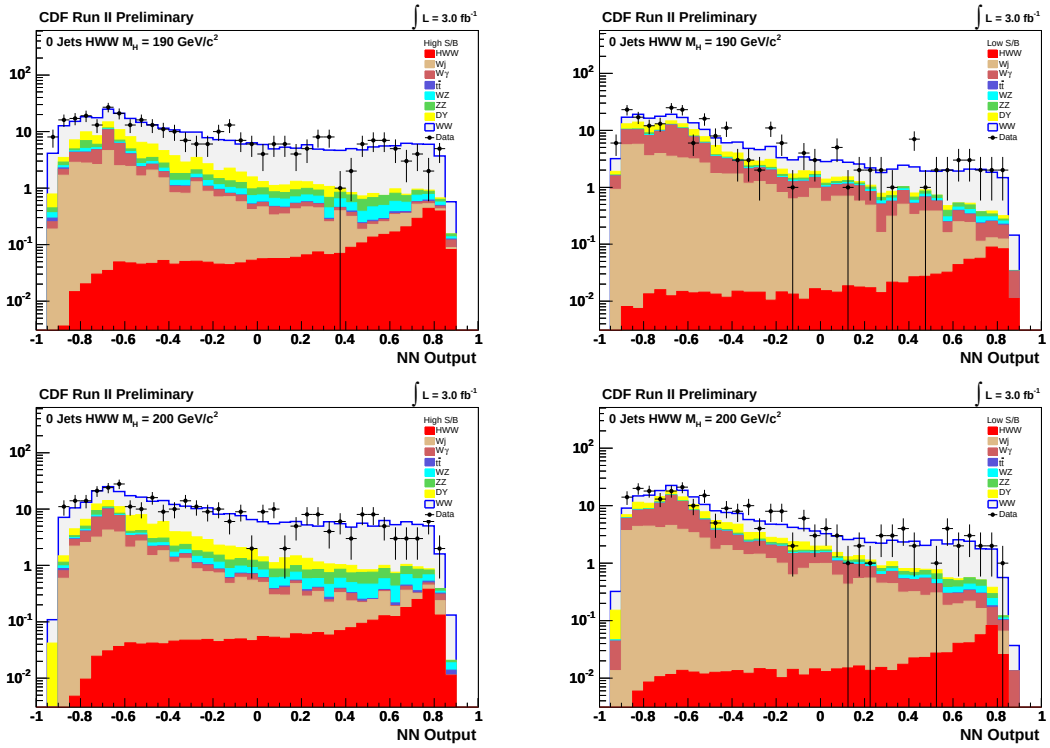

Figure A.5: Neural network output for high S/B (*left*) and low S/B (*right*) 0-jet events for $190 \leq M_H \leq 200$ GeV.

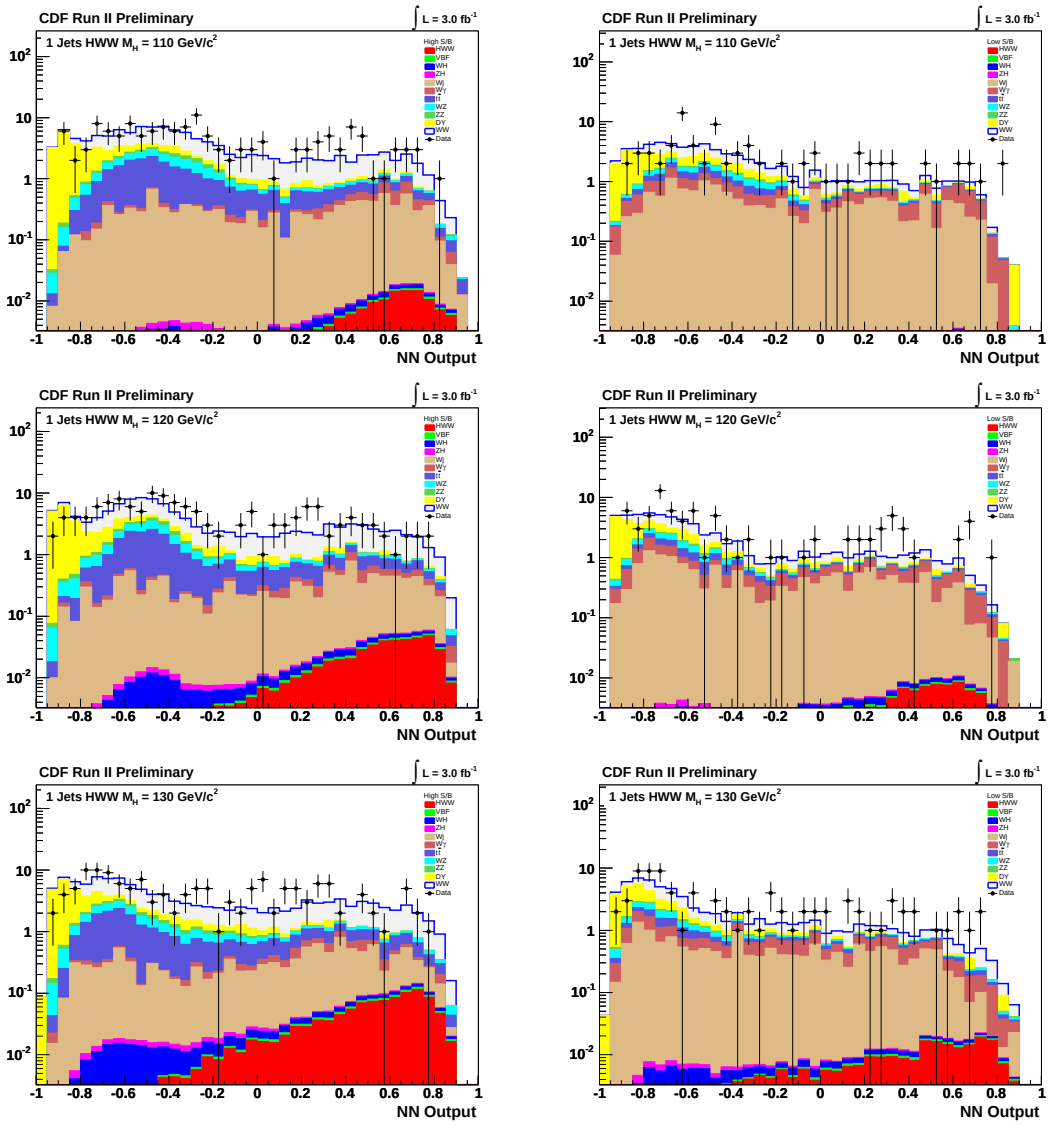

Figure A.6: Neural network output for high S/B (*left*) and low S/B (*right*) 1-jet events for $110 \leq M_H \leq 130$ GeV.

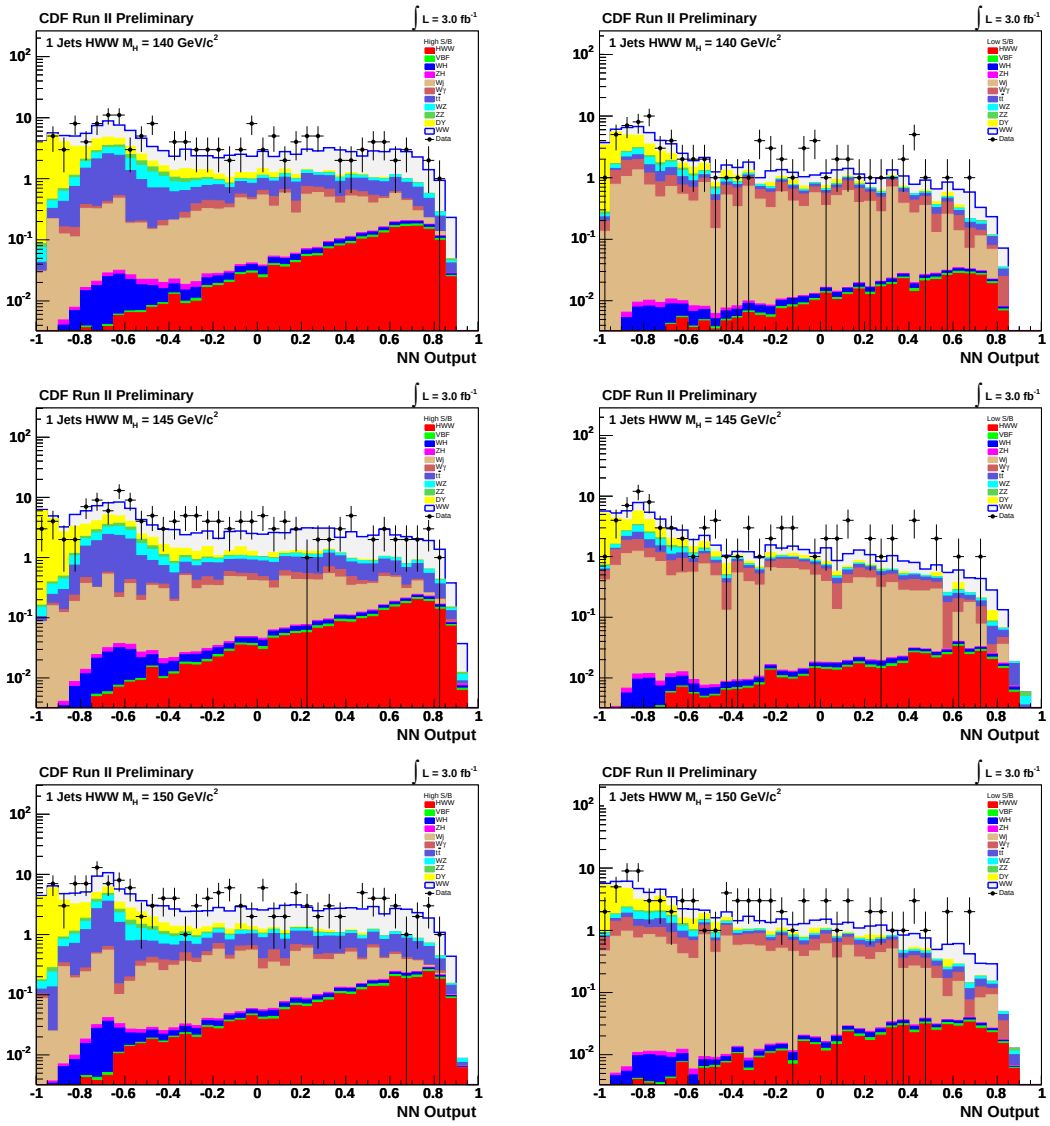

Figure A.7: Neural network output for high S/B (*left*) and low S/B (*right*) 1-jet events for $140 \leq M_H \leq 150$ GeV.

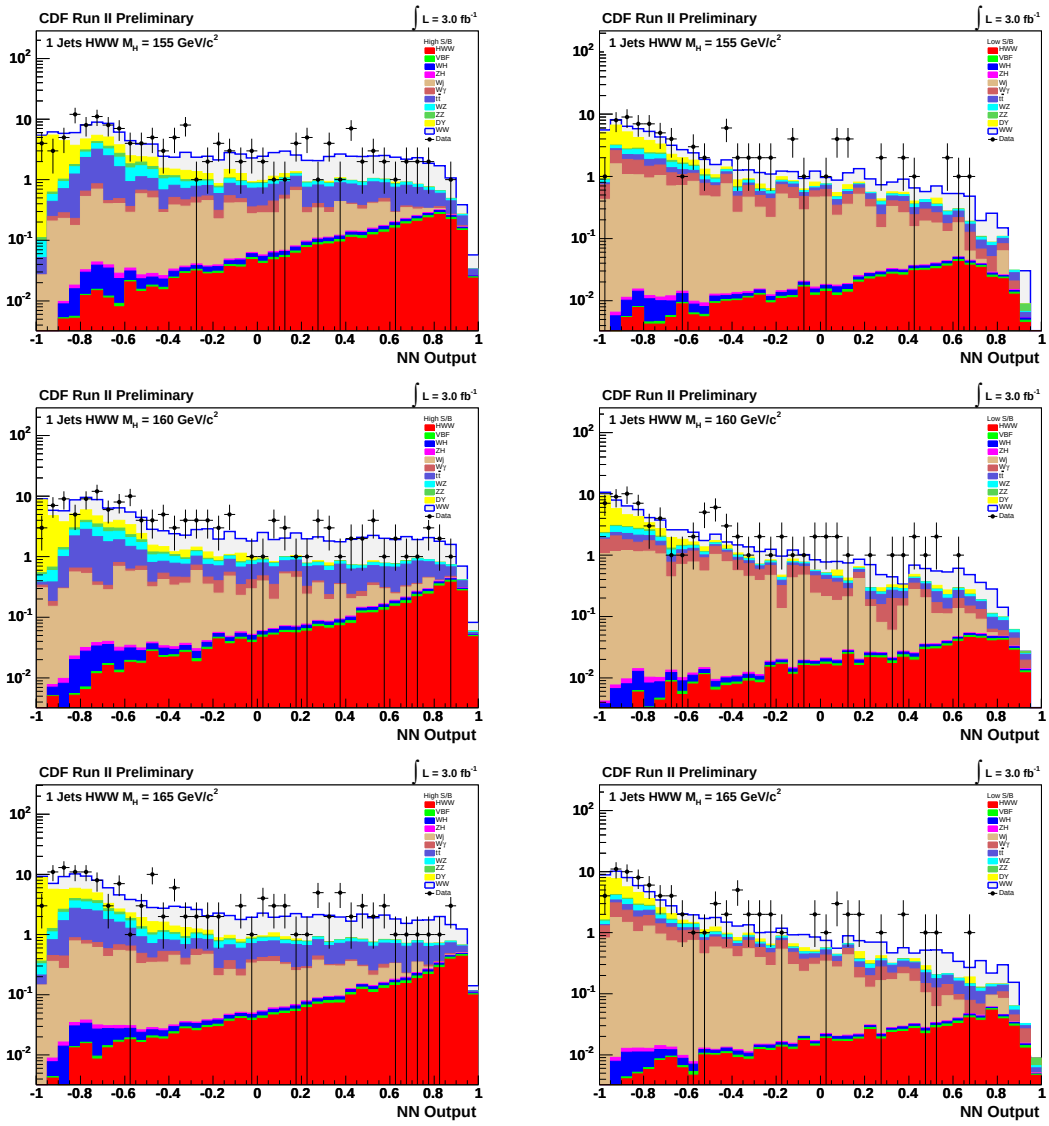

Figure A.8: Neural network output for high S/B (*left*) and low S/B (*right*) 1-jet events for $155 \leq M_H \leq 165$ GeV.

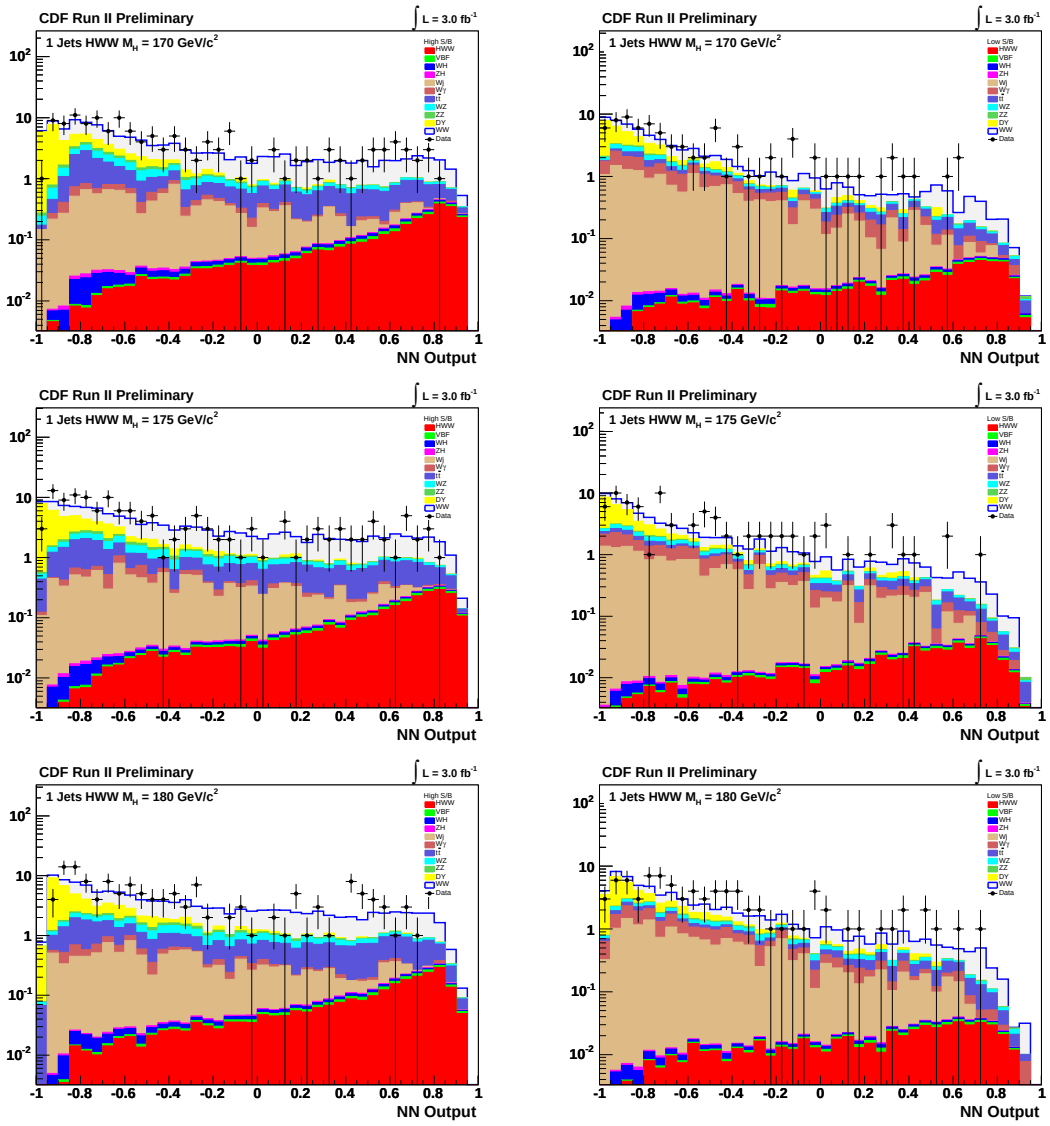

Figure A.9: Neural network output for high S/B (*left*) and low S/B (*right*) 1-jet events for $170 \leq M_H \leq 180$ GeV.

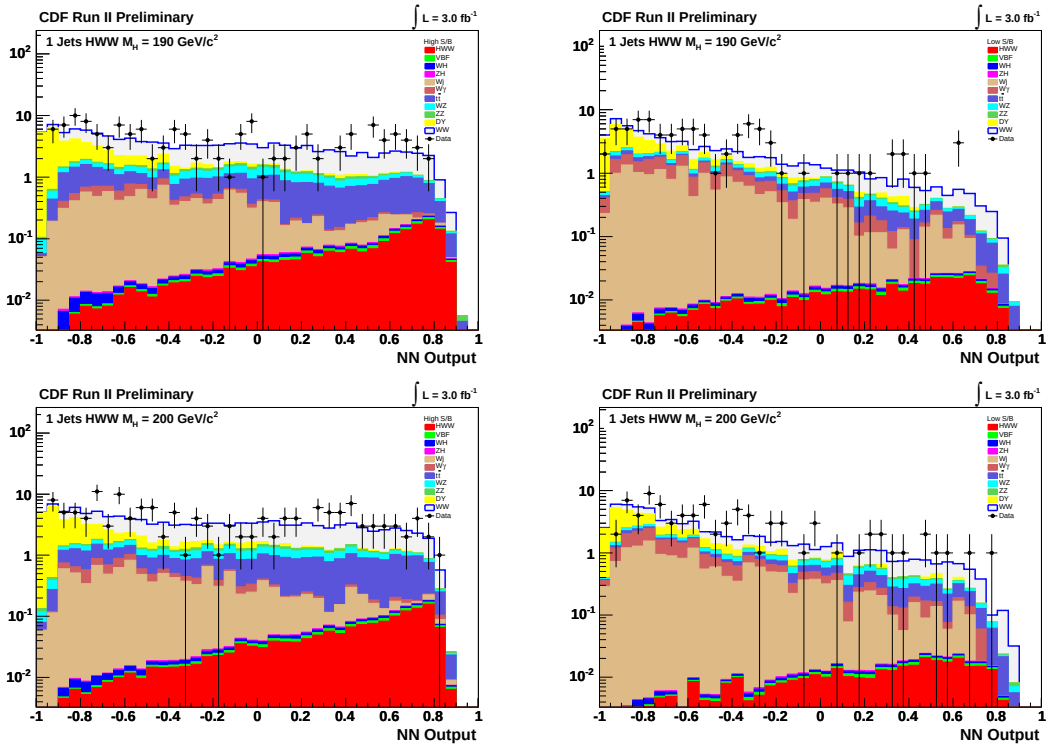

Figure A.10: Neural network output for high S/B (*left*) and low S/B (*right*) 1-jet events for $190 \leq M_H \leq 200$ GeV.

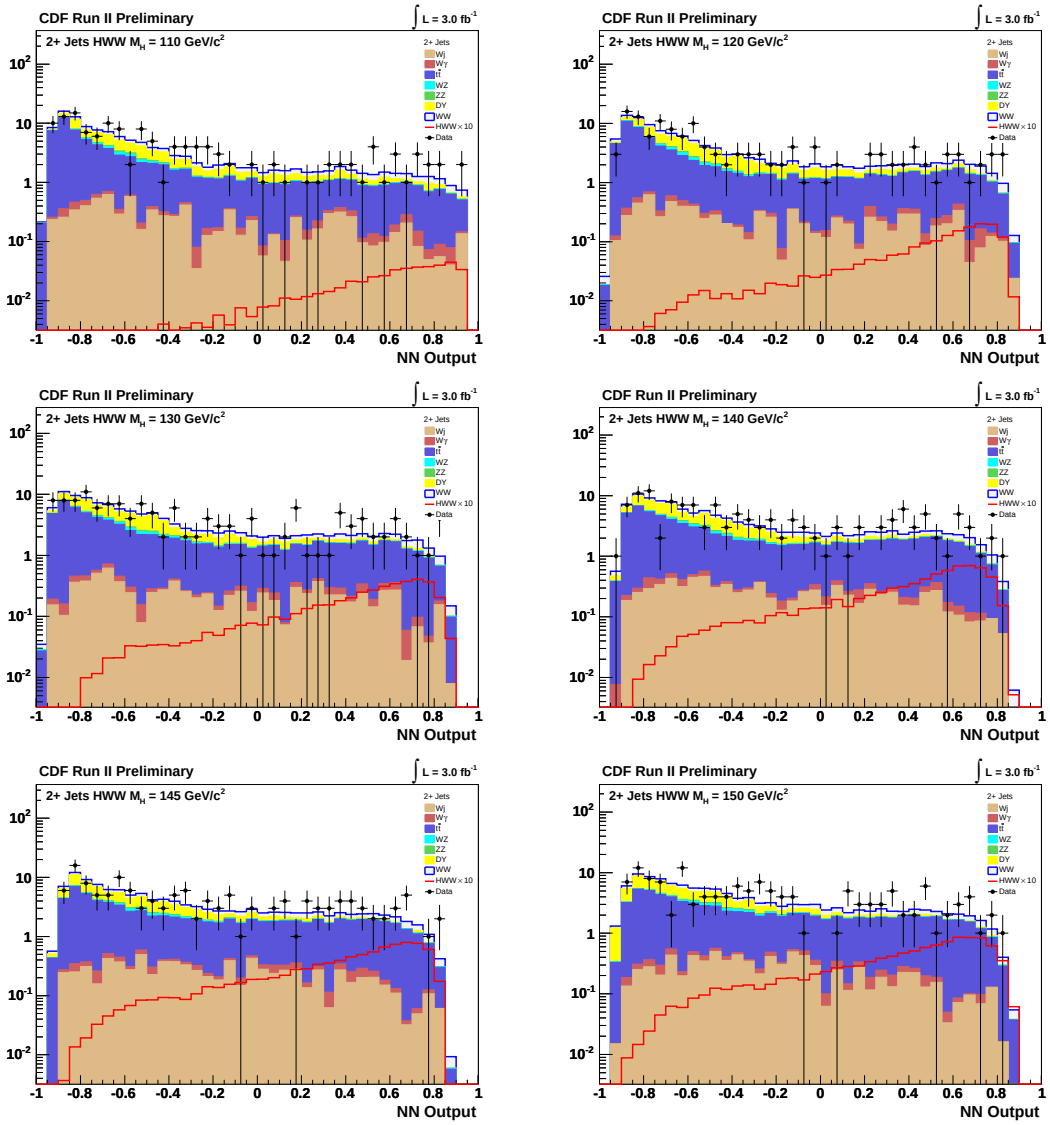

Figure A.11: Neural network output for ≥ 2 jet events for $110 \leq M_H \leq 150$ GeV.

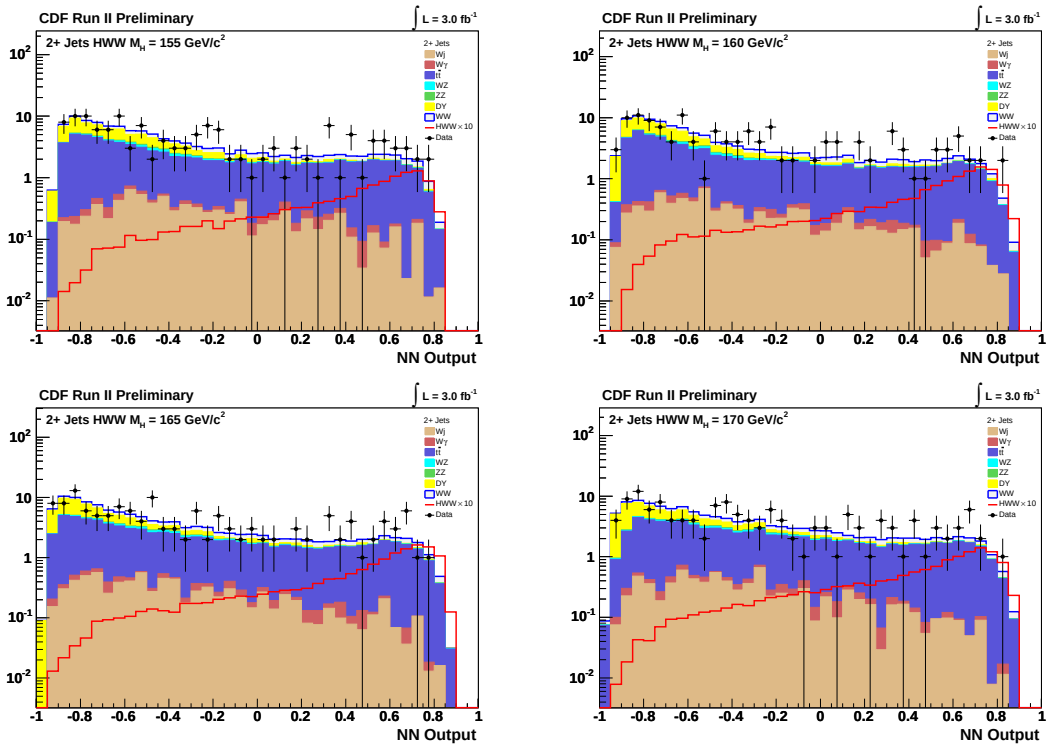

Figure A.12: Neural network output for ≥ 2 jet events for $155 \leq M_H \leq 170$ GeV.

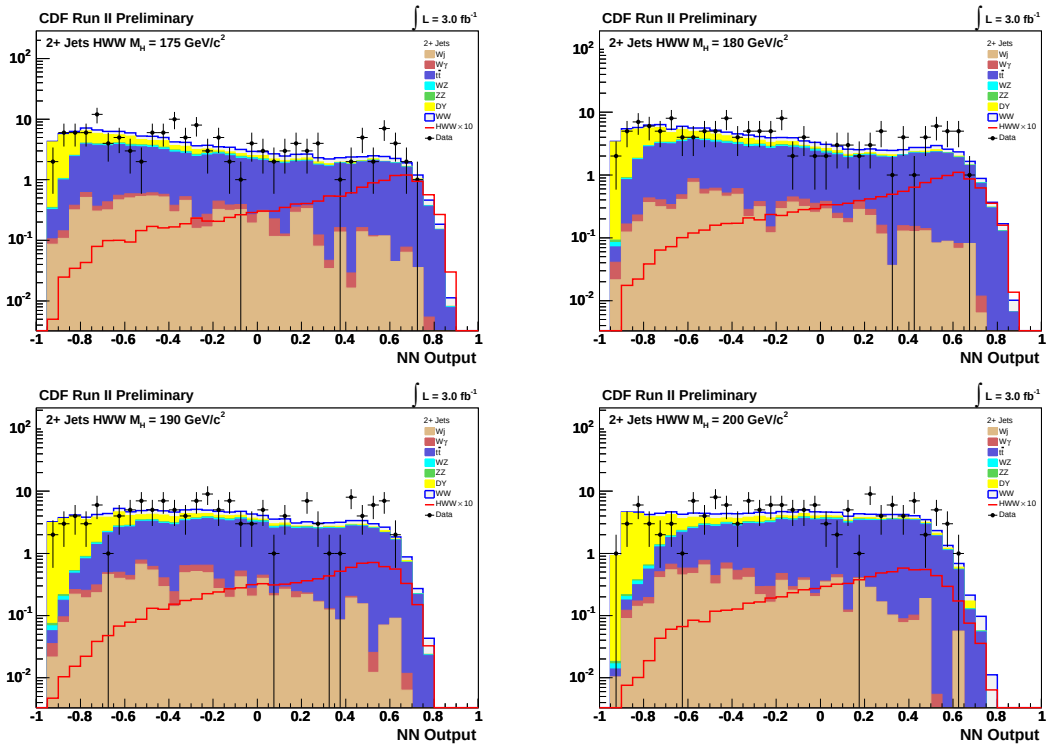

Figure A.13: Neural network output for ≥ 2 jet events for $175 \leq M_H \leq 200$ GeV.

Bibliography

[1] Information on Higgs cross section can be found on the TeV4LHC web page http://maltoni.home.cern.ch/maltoni/TeV4LHC/SM.html.

[2] Information on MINUIT can be found at http://cern.ch/minuit.

[3] These optimizations are a result of detailed studies performed by Simon Pagan Griso and presented at various HWW CDF meetings.

[4] U. Aglietta, B. Bonciani, G. Degrassi, and A. Vivini. Two-loop electroweak corrections to higgs production in proton-proton collisions. 2006. hep-ph/0610033.

[5] U. Aglietti, R. Bonciani, G. Degrassi, and A. Vicini. Two-loop electroweak corrections to higgs production in proton-proton collisions. 2006. hep-ph/0610033.

[6] A. Attal and A. Canepa. Photon Conversion Removal Efficiency, CDF/ANAL/ELECTRON/CDFR/8073. Technical report, CDF Collaboration, 2006.

[7] Vernon D. Barger and Roger J. N. Phillips. *Collider Physics*. Addison-Wesley, Redwood City, California, USA, 1987.

[8] U. Baur and E. L. Berger. Probing the weak-boson sector in $z\gamma$ production at hadron colliders. *Phys. Rev. D*, 47(11):4889–4904, Jun 1993.

[9] Edmond L. Berger and John Campbell. Higgs boson production in weak boson fusion at next-to-leading order. 2004. hep-ph/0403194.

[10] R. Blair et al. The CDF-II detector: Technical design report. FERMILAB-PUB-96-390-E.

[11] Veronique Boisvert. Trigger Efficiencies for the High ET Central Electrons in Gen6, CDF/DOC/ELECTRON/CDFR/7939. Technical report, CDF Collaboration, 2005.

[12] Oliver Brein, Abdelhak Djouadi, and Robert Harlander. Nnlo qcd corrections to the higgs-strahlung processes at hadron colliders. 2003. hep-ph/0307206.

[13] J. M. Campbell and R. K. Ellis. Update on vector boson pair production at hadron colliders. *Phys. Rev. D*, 60(11):113006, Nov 1999.

[14] J. M. Campbell and R. K. Ellis. Radiative corrections to $zb\bar{b}$ production. 2000. hep-ph/0006304v1.

[15] S. Catani, D. de Florian, M. Grazzini, and P. Nason. Soft-gluon resummation for higgs boson production at hadron colliders. *J. High Energy Phys.*, 2003(07), 2003. hep-ph/0306211.

[16] C. Chen, I. Cho, C. Hays, M. Herndon, J. Kraus, J. Kroll, T. Miao, P. Murat, R. OldeMan, and J.C Yun. Measurement of the Track Reconstruction Efficiency in the COT Using a MC Track Embedding Technique, CDF/PHYS/BOTTOM/CDFR/6394. Technical report, CDF Collaboration, 2003.

[17] M. L. Ciccolini, S. Dittmaier, and M. Krmer. Electroweak radiative corrections to associated wh and zh production at hadron colliders. 2003. hep-ph/0306234.

[18] ALEPH Collaboration, DELPHI Collaboration, L3 Collaboration, OPAL Collaboration, and The LEP Working Group for Higgs Boson Searches. Search for the standard model higgs boson at lep. *Physics Letters B*, 565(17):61–75, July 2003.

[19] ALEPH Collaboration, DELPHI Collaboration, L3 Collaboration, OPAL Collaboration, and LEP Electroweak Working Group. Precision electroweak measurements and constraints on the standard model. 2007. arXiv:0712.0929v2 [hep-ex].

[20] CDF Collaboration. Measurement of the w[sup +]w[sup -] production cross section in p[overline p] collisions at sqrt(s) = 1.96 tev using dilepton events. *Physical Review Letters*, 94(21):211801, 2005.

[21] CDF Collaboration and D0 Collaboration. Combined cdf and dzero upper limits on standard model higgs boson production at high mass (155-200 gev/c2) with 3 fb-1 of data. 2008. hep-ex/0808.0534.

[22] D0 Collaboration. Measurement of the ww production cross section in p[overline p] collisions at sqrt(s) = 1.96 tev. *Physical Review Letters*, 94(15):151801, 2005.

[23] The D0 Collaboration. Search for the higgs boson in $h \to ww^* \to \ell\ell'\nu\nu(\ell, \ell' = e, \mu)$ decays with 3.0 fb^{-1} at d0 in run ii, D0 Note 5757-CONF. Technical report, The D0 Collaboration, 2008.

[24] D.Benjamin, P. Bussey, T. Davies, D. Hidas, S. C. Hsu, M. Kruse, E. Lipeles, M. Neubauer, M. Norman, A Robson, R. St. Denis, A. S. Thompson, R. Vanguri, and F. Wurthwein. Search for HWW Production at Tevatron Using $1.9fb^{-1}$ Data - Public Note, CDF/PUB/EXOTIC/PUBLIC/8958. Technical report, CDF Collaboration, 2007.

[25] A. Djouadi, J. Kalinowski, and M. Spira. Hdecay: a program for higgs boson decays in the standard model and its supersymmetric extension. 1997. arXiv:hep-ph/9704448v1.

[26] A. Bhatti *et. al.* Determination of the Jet Energy Scale at the Collider Detector at Fermilab. 2006.

[27] C. Amsler *et. al. Physics Letters*, B667(1), 2008.

[28] D. Acosta *et al.* Measurement of the $t\bar{t}$ production cross section in $p\bar{p}$ collisions at $\sqrt{s}$ = 1.96 tev using lepton + jets events with secondary vertex b-tagging. *Physical Review D (Particles and Fields)*, 71(5):052003, 2005.

[29] D0 Collaboration: V. Abazov *et. al.* Observation of zz production in $p\bar{p}$ collisions at $\sqrt{s} = 1.96$ tev. 2008. hep-ex/0808.0703.

[30] Matteo Cacciari *et. al.* 068, 2004.

[31] S. Agostinelli *et al.* Geant4a simulation toolkit. *Nuclear Instruments and Methods in Physics Research Section A*, 506(4), 2003.

[32] T. Aaltonen *et. al.* Strong evidence for zz production in $p\bar{p}$ collisions at $\sqrt{s}$ = 1.96 tev. *Phys. Rev. Lett.*, 100(20):201801, May 2008.

[33] Michael Feindt. A neural bayesian estimator for conditional probability densities. 2004. arXiv:physics/0402093v1.

[34] M. Feindta and U. Kerzel. The neurobayes neural network package. *Nuclear Instruments and Methods in Physics Research Section A*, 559(190-194), 2006.

[35] S. Frixione and B.R. Webber. Matching nlo qcd computations and parton shower simulations. 0206(029), 2002. hep-ph/0204244.

[36] Y. Fukuda et al. Evidence for oscillation of atmospheric neutrinos. *Phys. Rev. Lett.*, 81:1562–1567, 1998.

[37] Ford Garberson, Sebastian Grinstein, Joao Guimaraes da Costa, J. Incandela, Chris Neu, and Daniel Sherman. Combination of the secvtx 1.2/fb b-tagging scale factors, CDF/DOC/SEC_VTX/CDFR/8666. Technical report, The CDF Collaboration, 2007.

[38] M. Grazzini. HNNLO: a MC program for Higgs boson production at hadron colliders. 2008. 0806.3336.

[39] LEP Electroweak Working Group. The lep electroweak working group, October 2008. `http://lepewwg.web.cern.ch/LEPEWWG/`.

[40] U. Grundler, A. Taffard, and X. Zhang. High-Pt muons recommended cuts & efficiencies for Winter 2006, CDF//MUON//7956. Technical report, CDF Collaboration, 2005.

[41] Ulysses Grundler, Anyes Taffard, and Xiaojian Zhang. High-Pt muons recommended cuts and efficiencies for Summer 2006, CDF/ANAL/TOP/CDFR/8262. Technical report, CDF Collaboration, 2005.

[42] E. Halkiadakis, C. Hays, M. Tecchio, and W. Yao. A Conversion Removal Algorithm for the 2003 Winter Coferences, CDF/DOC/TOP/CDFR/6250. Technical report, CDF Collaboration, 2003.

[43] Bo-Young Han and Veronique Boisvert. Trigger Efficiencies for the High Et Central Electron in the Gen6 data(run:217990 - 222426), CDF/DOC/ELECTRON/CDFR/8629. Technical report, CDF Collaboration, 2006.

[44] Bo-Young Han and Eva Halkiadakis. MET PEM trigger efficiency for Pheonix electrons, CDF/ANAL/ELECTROWEAK/CDFR/7940. Technical report, CDF Collaboration, 2005.

[45] Robert V. Harlander and William B. Kilgore. Next-to-next-to-leading order higgs production at hadron colliders. *Phys. Rev. Lett.*, 88(20):201801, May 2002.

[46] Joel Heinrich. Bayesian limit software: multi-channel with correlated backgrounds and efficiencies, CDF/MEMO/STATISTICS/PUBLIC/7587. Technical report, The CDF Collaboration, 2005.

[47] Peter W. Higgs. Broken symmetries and the masses of gauge bosons. *Phys. Rev. Lett.*, 13(16):508–509, Oct 1964.

[48] Shih-Chieh Hsu, Elliot Lipeles, Kevin McCarthy, Mark Neubauer, and Frank Wurthwein. Lepton ID and Fake Rates for the WW and WZ Analyses, CDF/ANAL/ELECTROWEAK/CDFR/8093. Technical report, CDF Collaboration, 2006.

[49] Shih-Chieh Hsu, Elliot Lipeles, Mark Neubauer, Kevin McCarthy, and Frank Wurthwein. Measurement of the ww cross section in dileptons + missing transverse energy, CDF/ANAL/ELECTROWEAK/CDFR/8094. Technical report, The CDF Collaboration, 2006.

[50] Shih-Chieh Hsu, Elliot Lipeles, Mark Neubauer, Matthew Norman, and Frank Wurthwein. Search for hww production with matrix element methods using $1.1 fb^{-1}$, CDF/PHYS/EXOTIC/CDFR/8719. Technical report, The CDF Collaboration, 2007.

[51] Yoshio Ishizawa and Jason Nielsen. Trigger Efficiencies for High Et Electrons, CDF/DOC/ELECTRON/CDFR/7401. Technical report, CDF Collaboration, 2004.

[52] S. Jadach. Foam: A general-purpose cellular monte carlo event generator. 2003. arXiv:physics/0203033v2.

[53] Tom Junk. Sensitivity, exclusion and discovery with small signals, large backgrounds, and large systematics, CDF/DOC/STATISTICS/PUBLIC/8128. Technical report, The CDF Collaboration, 2007.

[54] J. Konigsberg, S. Klimenko, S.M. Wang, D. Tsybychev, A. Sukhanov, S. Pronko, V. Necula, D. Acosta, G. Mitselmakher, A. Korytov, and G. Lungu. A first look at the CLC Luminosity Measurements, CDF/ANAL/CDF/CDFR/6052. Technical report, CDF Collaboration, 2002.

[55] H. L. Lai, J. Huston, S. Kuhlmann, J. Morfin, F. Olness, J. F. Owens, J. Pumplin, and W. K. Tung. Global qcd analysis of parton structure of the nucleon: Cteq5 parton distributions. 2000. hep-ph/9903282v3.

[56] Benjamin W. Lee, C. Quigg, and H. B. Thacker. Strength of weak interactions at very high energies and the higgs boson mass. *Phys. Rev. Lett.*, 38(16):883–885, Apr 1977.

[57] A. D. Martin, R. G. Roberts, W. J. Stirling, and R. S. Thorne. Parton distributions and the lhc: W and z production. 2000. hep-ph/9907231v1.

[58] Donald H. Perkins. *Introduction to High Energy Physics*. The Press Syndicate of the University of Cambridge, Cambridge, United Kingdom, 2000.

[59] J. Pumplin et al. New generation of parton distributions with uncertainties from global QCD analysis. *JHEP*, 07:012, 2002. hep-ph/0201195.

[60] W.K. Sakumoto. Event $|Z_{vtx}| < 60$ Cut Acceptance for Run II (to Sep05), CDF/ANAL/ELECTROWEAK/CDFR/7935. Technical report, CDF Collaboration, 2005.

[61] Torbjrn Sjstrand, Stephen Mrenna, and Peter Skands. 026(0605), 2006.

[62] Anyes Taffard. Run II Cosmic Ray Tagger, CDF/ANAL/MUON/CDFR/6100. Technical report, CDF Collaboration, 2002.

[63] Anyes Taffard. RunII Cosmic Ray Tagger Performances, CDF/ANAL/MUON/PUBLIC/6255. Technical report, CDF Collaboration, 2003.

[64] Alexei Varganov, Dan Amidei, and Dave Gerdes. Measurement of ttbar production cross section using dilepton events with in 2.7/fb, CDF/DOC/TOP/PUBLIC/9399. Technical report, The CDF Collaboration, 2008.

[65] Alexei Varganov, Dan Amidei, and Dave Gerdes. Measurement of ttbar production cross section using dilepton events with tight secvtx tag in 2/fb, CDF/DOC/TOP/PUBLIC/9271. Technical report, The CDF Collaboration, 2008.

[66] R. G. Wagner. Electron Identification for Run II: Understanding and Using Lshr, CDF/DOC/ELECTRON/CDFR/6249. Technical report, CDF Collaboration, 2003.

Biography

Dean Andrew Hidas [redacted] He then attended the University of California San Diego where he received a bachelor of science degree in Physics in 2002. In summer of 2002 he traveled across the country to begin postgraduate study at Duke University in Durham, North Carolina. In May 2004 he relocated to Chicago, Illinois while conducting research at Fermi National Accelerator Laboratory in Batavia, IL. In December of 2008 he received his doctorate of philosophy in physics.